

JPL Publication 92-14, Vol. 3

Summaries of the Third Annual JPL
Airborne Geoscience Workshop
June 1-5, 1992

Volume 3. AIRSAR Workshop

Jakob van Zyl
Editor

(NASA-CR-194542) SUMMARIES OF THE
THIRD ANNUAL JPL AIRBORNE
GEOSCIENCE WORKSHOP. VOLUME 3:
AIRSAR WORKSHOP (JPL) 120 p

N94-16731
--THRU--
N94-16762
Unclas

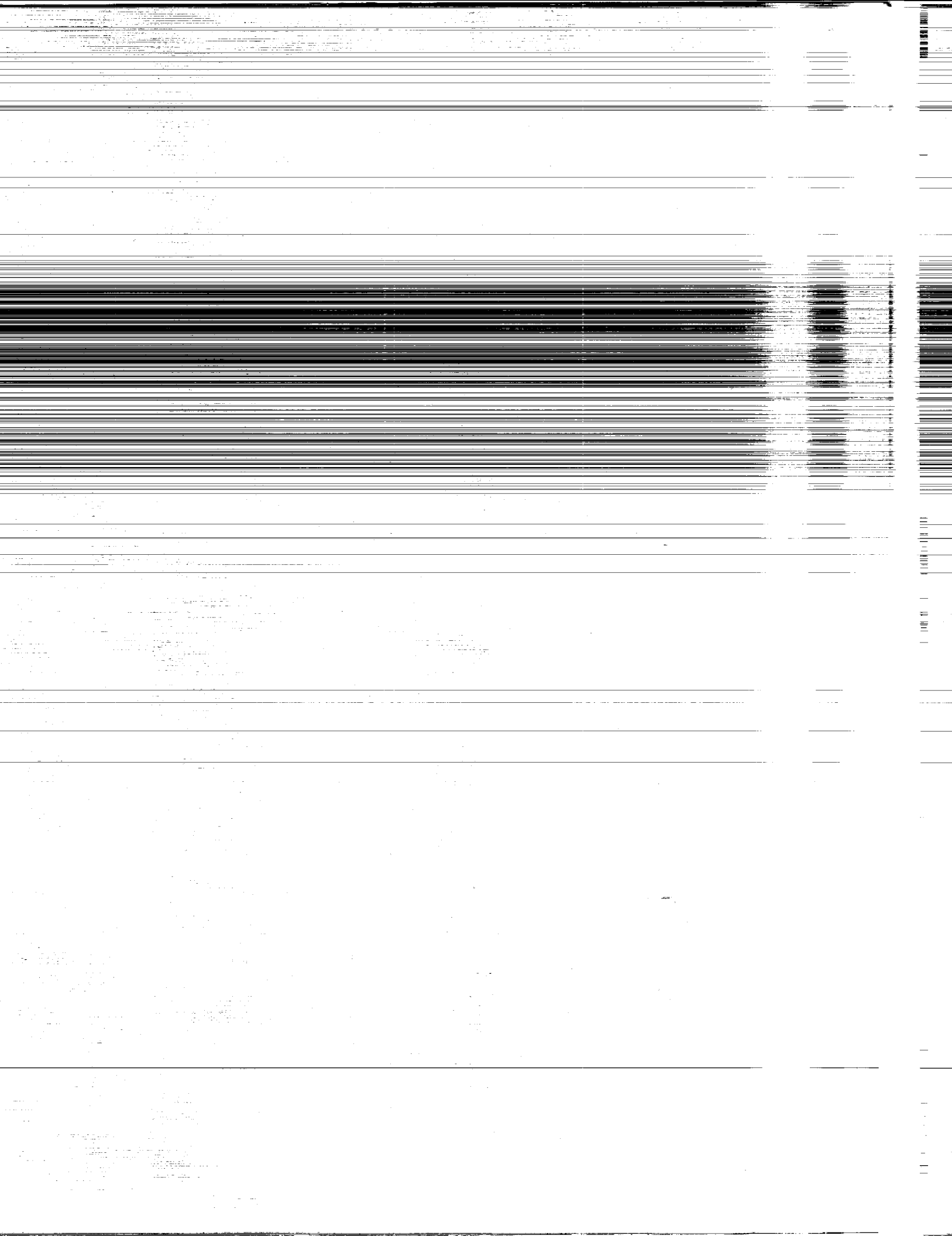
G3/42 0189109

June 1, 1992



National Aeronautics and
Space Administration

Jet Propulsion Laboratory
California Institute of Technology
Pasadena, California



Summaries of the Third Annual JPL Airborne Geoscience Workshop June 1–5, 1992

Volume 3. AIRSAR Workshop

Jakob van Zyl
Editor

June 1, 1992



National Aeronautics and
Space Administration

Jet Propulsion Laboratory
California Institute of Technology
Pasadena, California

This publication was prepared by the Jet Propulsion Laboratory, California Institute of Technology, under a contract with the National Aeronautics and Space Administration.

ABSTRACT

This publication contains the preliminary agenda and summaries for the Third Annual JPL Airborne Geoscience Workshop, held at the Jet Propulsion Laboratory, Pasadena, California, on June 1–5, 1992. This main workshop is divided into three smaller workshops as follows:

- The Airborne Visible/Infrared Imaging Spectrometer (AVIRIS) workshop, on June 1 and 2. The summaries for this workshop appear in Volume 1.
- The Thermal Infrared Multispectral Scanner (TIMS) workshop, on June 3. The summaries for this workshop appear in Volume 2.
- The Airborne Synthetic Aperture Radar (AIRSAR) workshop, on June 4 and 5. The summaries for this workshop appear in Volume 3.

CONTENTS

Volume 1: AVIRIS Workshop

Preliminary Agenda.....	xiii
In-Flight Calibration of the Spectral and Radiometric Characteristics of AVIRIS in 1991.....	1
<i>Robert O. Green, James E. Conel, Carol J. Bruegge, Jack S. Margolis, Veronique Carrere, Gregg Vane, and Gordon Hoover</i>	
Using AVIRIS Images To Measure Temporal Trends in Abundance of Photosynthetic and Nonphotosynthetic Canopy Components.....	5
<i>Susan L. Ustin, Milton O. Smith, Dar Roberts, John A. Gamon, and Christopher B. Field</i>	
Unmixing AVIRIS Data To Provide a Method for Vegetation Fraction Subtraction.....	8
<i>J.A. Zamudio</i>	
Mapping the Mineralogy and Lithology of Canyonlands, Utah With Imaging Spectrometer Data and the Multiple Spectral Feature Mapping Algorithm.....	11
<i>Roger N. Clark, Gregg A. Swayze, and Andrea Gallagher</i>	
Spatial Resolution and Cloud Optical Thickness Retrievals.....	14
<i>Rand E. Feind, Sundar A. Christopher, and Ronald M. Welch</i>	
Evaluation of Spatial Productivity Patterns in an Annual Grassland During an AVIRIS Overflight.....	17
<i>John A. Gamon, Christopher B. Field, and Susan L. Ustin</i>	
Hyperspectral Modeling for Extracting Aerosols From Aircraft/Satellite Data.....	20
<i>G. Daniel Hickman and Michael J. Duggin</i>	
The Spectral Image Processing System (SIPS)—Software for Integrated Analysis of AVIRIS Data.....	23
<i>F.A. Kruse, A.B. Lefkoff, J.W. Boardman, K.B. Heidebrecht, A.T. Shapiro, P.J. Barloon, and A.F.H. Goetz</i>	
First Results From Analysis of Coordinated AVIRIS, TIMS, and ISM (French) Data for the Ronda (Spain) and Beni Bousera (Morocco) Peridotites.....	26
<i>J.F. Mustard, S. Hurtrez, P. Pinet, and C. Sotin</i>	
AVIRIS Study of Death Valley Evaporite Deposits Using Least-Squares Band- Fitting Methods.....	29
<i>J.K. Crowley and R.N. Clark</i>	
A Field Measure of the "Shade" Fraction.....	32
<i>Alan R. Gillespie, Milton O. Smith, and Donald E. Sabol</i>	
A Linear Spectral Matching Technique for Retrieving Equivalent Water Thickness and Biochemical Constituents of Green Vegetation.....	35
<i>Bo-Cai Gao and Alexander F.H. Goetz</i>	

Mapping the Spectral Variability in Photosynthetic and Non-Photosynthetic Vegetation, Soils and Shade Using AVIRIS	38
<i>Dar A. Roberts, Milton O. Smith, Donald E. Sabol, John B. Adams, and Susan Ustin</i>	
Volcanic Thermal Features Observed by AVIRIS.....	41
<i>Clive Oppenheimer, David Pieri, Veronique Carrere, Michael Abrams, David Rothery, and Peter Francis</i>	
Retrieval of Biophysical Parameters With AVIRIS and ISM—The Landes Forest, South West France	44
<i>F. Zagolski, J.P. Gastellu-Etchegorry, E. Mougín, G. Giordano, G. Marty, T. Le Toan, and A. Beaudoin</i>	
Ground-Truthing AVIRIS Mineral Mapping at Cuprite, Nevada.....	47
<i>Gregg Swayze, Roger N. Clark, Fred Kruse, Steve Sutley, and Andrea Gallagher</i>	
Exploring the Remote Sensing of Foliar Biochemical Concentrations With AVIRIS Data	50
<i>Geoffrey M. Smith and Paul J. Curran</i>	
Seasonal and Spatial Variations in Phytoplanktonic Chlorophyll in Eutrophic Mono Lake, California, Measured With the Airborne Visible and Infrared Imaging Spectrometer (AVIRIS)	53
<i>John M. Melack and Mary Gastil</i>	
AVIRIS Calibration and Application in Coastal Oceanic Environments	56
<i>Kendall L. Carder</i>	
Mapping Vegetation Types With the Multiple Spectral Feature Mapping Algorithm in Both Emission and Absorption.....	60
<i>Roger N. Clark, Gregg A. Swayze, Christopher Koch, and Cathy Ager</i>	
Multiple Dataset Water-Quality Analyses in the Vicinity of an Ocean Wastewater Plume.....	63
<i>Michael Hamilton, Curtiss O. Davis, W. Joseph Rhea, and Jeannette van den Bosch</i>	
MAC Europe 91: Evaluation of AVIRIS, GER Imaging Spectrometry Data for the Land Application Testsite Oberpfaffenhofen.....	66
<i>F. Lehmann, R. Richter, H. Rothfuss, K. Werner, P. Hausknecht, A. Müller, and P. Strobl</i>	
Using Endmembers in AVIRIS Images To Estimate Changes in Vegetative Biomass	69
<i>Milton O. Smith, John B. Adams, Susan L. Ustin, and Dar A. Roberts</i>	
Atmospheric Correction of AVIRIS Data in Ocean Waters	72
<i>Gregory Terrie and Robert Arnone</i>	

The 1991 AVIRIS/POLDER Experiment in Camargue, France.....	75
<i>F. Baret, C. Leprieur, S. Jacquemoud, V. Carrère, X.F. Gu, M. Steven, V. Vanderbilt, J.F. Hanocq, S. Ustin, G. Rondeaux, C. Daughtry, L. Biehl, R. Pettigrew, D. Modro, H. Horoyan, T. Sarto, C. Despontin, and H. Razafindraibe</i>	
AVIRIS: Recent Instrument Maintenance, Modifications and 1992 Performance.....	78
<i>Thomas G. Chrien</i>	
AVIRIS Ground Data Processing System.....	80
<i>Earl G. Hansen, Steve Larson, H. Ian Novack, and Robert Bennett</i>	
Simulation of ASTER Data Using AVIRIS Images	83
<i>Michael Abrams</i>	
Use of AVIRIS Data to the Definition of Optimised Specifications for Land Applications With Future Spaceborne Imaging Spectrometers	85
<i>J. Bodechtel</i>	
Primary Studies of Trace Quantities of Green Vegetation in Mono Lake Area Using 1990 AVIRIS Data	86
<i>Zhikang Chen, Chris D. Elvidge, and David P. Groeneveld</i>	
JPL Activities on Development of Acousto-Optic Tunable Filter Imaging Spectrometer.....	88
<i>Li-Jen Cheng, Tien-Hsin Chao, and George Reyes</i>	
Measuring Dry Plant Residues in Grasslands: A Case Study Using AVIRIS	91
<i>Michael Fitzgerald and Susan L. Ustin</i>	
Analysis of AVIRIS San Pedro Channel Data: Methods and Applications.....	94
<i>Richard B. Frost</i>	
Tracking Photosynthetic Efficiency With Narrow-Band Spectroradiometry	95
<i>John A. Gamon and Christopher B. Field</i>	
Separation of Cirrus Cloud From Clear Surface From AVIRIS Data Using the 1.38- μ m Water Vapor Band.....	98
<i>Bo-Cai Gao and Alexander F.H. Goetz</i>	
Software for the Derivation of Scaled Surface Reflectances From AVIRIS Data.....	101
<i>Bo-Cai Gao, Kathleen Heidebrecht, and Alexander F.H. Goetz</i>	
Integrating Remote Sensing Techniques at Cuprite, Nevada: AVIRIS, Thematic Mapper, and Field Spectroscopy	104
<i>Bradley Hill, Greg Nash, Merrill Ridd, Phoebe Hauff, and Phil Ebel</i>	
Evaluation of AVIRISwiss-91 Campaign Data	108
<i>K.I. Itten, P. Meyer, K. Staenz, T. Kellenberger, and M. Schaepman</i>	
AVIRIS Investigator's Guide.....	111
<i>Howell Johnson</i>	

Oregon Transect: Comparison of Leaf-Level Reflectance With Canopy-Level and Modelled Reflectance.....	113
<i>Lee F. Johnson, Frederic Baret, and David L. Peterson</i>	
AVIRIS as a Tool for Carbonatite Exploration: Comparison of SPAM and Mbandmap Data Analysis Methods	116
<i>Marguerite J. Kingston and James K. Crowley</i>	
Expert System-Based Mineral Mapping Using AVIRIS	119
<i>F.A. Kruse, A.B. Lefkoff, and J.B. Dietz</i>	
The EARSEC Programme in Relation to the 1991 MAC-Europe Campaign.....	122
<i>Wim J. Looyen, Jean Verdebout, Benny M. Sorensen, Giancarlo Maracci, Guido Schmuck, and Alois J. Sieber</i>	
Preliminary Statistical Analysis of AVIRIS/TMS Data Acquired Over the Matera Test Site.....	125
<i>Stefania Mattei and Sergio Vetrella</i>	
AVIRIS Data and Neural Networks Applied to an Urban Ecosystem.....	129
<i>Merrill K. Ridd, Niles D. Ritter, Nevin A. Bryant, and Robert O. Green</i>	
Temporal Variation in Spectral Detection Thresholds of Substrate and Vegetation in AVIRIS Images.....	132
<i>Donald E. Sabol, Jr., Dar Roberts, Milton Smith, and John Adams</i>	
Discussion of Band Selection and Methodologies for the Estimation of Precipitable Water Vapour From AVIRIS Data	135
<i>Dena Schanzer and Karl Staenz</i>	
Abundance Recovery Error Analysis Using Simulated AVIRIS Data	138
<i>William W. Stoner, Joseph C. Harsanyi, William H. Farrand, and Jennifer A. Wong</i>	
Multitemporal Diurnal AVIRIS Images of a Forested Ecosystem	141
<i>Susan L. Ustin, Milton O. Smith, and John B. Adams</i>	
A Comparison of LOWTRAN-7 Corrected Airborne Visible/Infrared Imaging Spectrometer (AVIRIS) Data With Ground Spectral Measurements	144
<i>Pengyang Xu and Ronald Greeley</i>	
Discrimination Among Semi-Arid Landscape Endmembers Using the Spectral Angle Mapper (SAM) Algorithm.....	147
<i>Roberta H. Yuhas, Alexander F.H. Goetz, and Joe W. Boardman</i>	
Empirical Relationships Among Atmospheric Variables From Rawinsonde and Field Data as Surrogates for AVIRIS Measurements: Estimation of Regional Land Surface Evapotranspiration	150
<i>James E. Conel, Gordon Hoover, Anne Nolin, Ron Alley, and Jack Margolis</i>	
The JPL Spectral Library 0.4 to 2.5 Micrometers.....	152
<i>Simon J. Hook, Cindy I. Grove, and Earnest D. Paylor II</i>	

Lossless Compression of AVIRIS Data: Comparison of Methods and Instrument Constraints.....	154
<i>R.E. Roger, J.F. Arnold, M.C. Cavenor, and J.A. Richards</i>	
Simulation of AVHRR-K Band Ratios With AVIRIS.....	157
<i>Melanie A. Wetzel and Ronald M. Welch</i>	
Volume 2: TIMS Workshop	
Preliminary Agenda.....	xiii
TIMS Performance Evaluation Summary	1
<i>Bruce Spiering, G. Meeks, J. Anderson, S. Jaggi, and S. Kuo</i>	
A Quantitative Analysis of TIMS Data Obtained on the Learjet 23 at Various Altitudes	4
<i>S. Jaggi</i>	
Analysis of TIMS Performance Subjected to Simulated Wind Blast	7
<i>S. Jaggi and S. Kuo</i>	
Sensitivity of Blackbody Reference Panels to Wind Blast	10
<i>Gordon Hoover</i>	
Comparison of Preliminary Results From Airborne ASTER Simulator (AAS) With TIMS Data.....	13
<i>Yoshiaki Kannari, Franklin Mills, Hiroshi Watanabe, Teruya Ezaka, Tatsuhiko Narita, and Sheng-Huei Chang</i>	
Application of Split Window Technique to TIMS Data	16
<i>Tsuneo Matsunaga, Shuichi Rokugawa, and Yoshinori Ishii</i>	
Atmospheric Corrections for TIMS Estimated Emittance	19
<i>T.A. Warner and D.W. Levandowski</i>	
An Algorithm for the Estimation of Bounds on the Emissivity and Temperatures From Thermal Multispectral Airborne Remotely Sensed Data	22
<i>S. Jaggi, D. Quattrochi, and R. Baskin</i>	
Multi-Resolution Processing for Fractal Analysis of Airborne Remotely Sensed Data	25
<i>S. Jaggi, D. Quattrochi, and N. Lam</i>	
Preliminary Analysis of Thermal-Infrared Multispectral Scanner Data of the Iron Hill, Colorado Carbonatite-Alkalic Rock Complex	28
<i>Lawrence C. Rowan, Kenneth Watson, and Susanne H. Miller</i>	
The Use of TIMS for Mapping Different Pahoehoe Surfaces: Mauna Iki, Kilauea	31
<i>Scott K. Rowland</i>	
Ejecta Patterns of Meteor Crater, Arizona Derived From the Linear Un-Mixing of TIMS Data and Laboratory Thermal Emission Spectra.....	34
<i>Michael S. Ramsey and Philip R. Christensen</i>	

The Use of TIMS Data To Estimate the SO ₂ Concentrations of Volcanic Plumes: A Case Study at Mount Etna, Sicily..... <i>Vincent J. Realmuto</i>	37
ATTIRE (Analytical Tools for Thermal Infrared Engineering)—A Thermal Sensor Simulation Package <i>S. Jaggi</i>	40
Kilauea Data Set Compiled for Distribution on Compact Disc <i>Lori Glaze, George Karas, Sonia Chernobieff, Elsa Abbott, and Earnie Paylor</i>	43
Volume 3: AIRSAR Workshop	
Preliminary Agenda.....	xiii
A Snow Wetness Retrieval Algorithm for SAR..... <i>Jiancheng Shi and Jeff Dozier</i>	1
Comparison of JPL-AIRSAR and DLR E-SAR Images from the MAC Europe '91 Campaign Over Testsite Oberpfaffenhofen: Frequency and Polarization Dependent Backscatter Variations From Agricultural Fields <i>C. Schmullius and J. Nithack</i>	4
Monitoring Environmental State of Alaskan Forests With AIRSAR <i>Kyle C. McDonald, JoBea Way, Eric Rignot, Cindy Williams, Les Viereck, and Phylis Adams</i>	7
Comparison of Modeled Backscatter With SAR Data at P-Band..... <i>Yong Wang, Frank W. Davis, and John M. Melack</i>	9
SAR Backscatter From Coniferous Forest Gaps..... <i>John L. Day and Frank W. Davis</i>	12
Retrieval of Pine Forest Biomass Using JPL AIRSAR Data..... <i>A. Beaudoin, T. Le Toan, F. Zagolski, C.C. Hsu, H.C. Han, and J.A. Kong</i>	15
Characterization of Wetland, Forest, and Agricultural Ecosystems in Belize With Airborne Radar (AIRSAR)..... <i>Kevin O. Pope, Jose Maria Rey-Benayas, and Jack F. Paris</i>	18
Strategies for Detection of Floodplain Inundation With Multi-Frequency Polarimetric SAR <i>Laura L. Hess and John M. Melack</i>	21
Supervised Fully Polarimetric Classification of the Black Forest Test Site: From MAESTRO1 to MAC Europe..... <i>G. De Grandi, C. Lavalley, H. De Groof, and A. Sieber</i>	24
Relating Multifrequency Radar Backscattering to Forest Biomass: Modeling and AIRSAR Measurement <i>Guoqing Sun and K. Jon Ranson</i>	27

SAR Observations in the Gulf of Mexico	30
<i>David Sheres</i>	
Investigation of AIRSAR Signatures of the Gulf Stream	32
<i>G.R. Valenzuela, J.S. Lee, D.L. Schuler, G.O. Marmorino, F. Askari, K. Hoppel, J.A.C. Kaiser, and W.C. Keller</i>	
Mapping of Sea Bottom Topography	35
<i>C.J. Calcoen, G.J. Wensink, and G.H.F.M. Hesselms</i>	
Sea Bottom Topography Imaging With SAR	38
<i>M.W.A. van der Kooij, G.J. Wensink, and J. Vogelzang</i>	
Preliminary Results of Polarization Signatures for Glacial Moraines in the Mono Basin, Eastern Sierra Nevada	40
<i>Richard R. Forster, Andrew N. Fox, and Bryan Isacks</i>	
Detecting Surface Roughness Effects on the Atmospheric Boundary Layer Via AIRSAR Data: A Field Experiment in Death Valley, California	43
<i>Dan G. Blumberg and Ronald Greeley</i>	
Extraction of Quantitative Surface Characteristics From AIRSAR Data for Death Valley, California	46
<i>K.S. Kierein-Young and F.A. Kruse</i>	
The TOPSAR Interferometric Radar Topographic Mapping Instrument	49
<i>Howard A. Zebker, Søren N. Madsen, Jan Martin, Giovanni Alberti, Sergio Vetrella, and Alessandro Cucci</i>	
Evaluation of the TOPSAR Performance by Using Passive and Active Calibrators	53
<i>G. Alberti, A. Moccia, S. Ponte, and S. Vetrella</i>	
Fitting a Three-Component Scattering Model to Polarimetric SAR Data	56
<i>A. Freeman and S. Durden</i>	
Application of Symmetry Properties to Polarimetric Remote Sensing With JPL AIRSAR Data	59
<i>S.V. Nghiem, S.H. Yueh, R. Kwok, and F.K. Li</i>	
External Calibration of Polarimetric Radar Images Using Distributed Targets	62
<i>Simon H. Yueh, S.V. Nghiem, and R. Kwok</i>	
Processing of Polarimetric SAR Data for Soil Moisture Estimation Over Mahantango Watershed Area	65
<i>K.S. Rao, W.L. Teng, and J.R. Wang</i>	
Evaluation of Polarimetric SAR Parameters for Soil Moisture Retrieval	69
<i>Jiancheng Shi, Jakob J. van Zyl, and Edwin T. Engman</i>	
Interaction Types and Their Like-Polarization Phase-Angle Difference Signatures	72
<i>Jack F. Paris</i>	

Application of Modified VICAR/IBIS GIS to Analysis of July 1991 Flevoland AIRSAR Data.....	75
<i>L. Norikane, B. Broek, and A. Freeman</i>	
Radar Analysis and Visualization Environment (RAVEN): Software for Polarimetric Radar Analysis.....	78
<i>K.S. Kierein-Young, A.B. Lefkoff, and F.A. Kruse</i>	
Measuring Ocean Coherence Time With Dual-Baseline Interferometry	81
<i>Richard E. Carande</i>	
A Bibliography of Global Change, Airborne Science, 1985-1991	84
<i>Edwin J. Sheffner and James G. Lawless</i>	
Soil Conservation Applications With C-Band SAR	86
<i>B. Brisco, R.J. Brown, J. Naunheimer, and D. Bedard</i>	
Comparison of Edges Detected at Different Polarisation in MAESTRO Data	89
<i>Ronald G. Caves, Peter J. Harley, and Shaun Quegan</i>	
Lithological and Textural Controls on Radar and Diurnal Thermal Signatures of Weathered Volcanic Deposits, Lunar Crater Region, Nevada.....	92
<i>Jeffrey J. Plaut and Benoit Rivard</i>	

AGENDA

THIRD ANNUAL JPL AIRBORNE GEOSCIENCE WORKSHOP: AIRBORNE VISIBLE/INFRARED IMAGING SPECTROMETER (AVIRIS)

June 1 and 2, 1992
Von Karman Auditorium
Jet Propulsion Laboratory
Pasadena, California 91109

MONDAY, JUNE 1, 1992

- 7:15 a.m. Shuttle bus departs Pasadena Ritz-Carlton Hotel for JPL.
- 7:30 a.m. Registration and continental breakfast at JPL.
- 8:00 a.m. Welcome
- 8:30 a.m. In-Flight Calibration of the Spectral and Radiometric Characteristics of AVIRIS in 1991
Robert O. Green, James E. Conel, Carol J. Bruegge, Jack S. Margolis, Veronique Carrere, Gregg Vane, and Gordon Hoover
- 9:00 a.m. Using AVIRIS Images To Measure Temporal Trends in Abundance of Photosynthetic and Nonphotosynthetic Canopy Components
Susan L. Ustin, Milton O. Smith, Dar Roberts, John A. Gamon, and Christopher B. Field
- 9:30 a.m. Unmixing AVIRIS Data To Provide a Method for Vegetation Fraction Subtraction
J.A. Zamudio
- 10:00 a.m. Break
- 10:30 a.m. Mapping the Mineralogy and Lithology of Canyonlands, Utah With Imaging Spectrometer Data and the Multiple Spectral Feature Mapping Algorithm
Roger N. Clark, Gregg A. Swayze, and Andrea Gallagher
- 11:00 a.m. Spatial Resolution and Cloud Optical Thickness Retrievals
Rand E. Feind, Sundar A. Christopher, and Ronald M. Welch
- 11:30 a.m. Evaluation of Spatial Productivity Patterns in an Annual Grassland During an AVIRIS Overflight
John A. Gamon, Christopher B. Field, and Susan L. Ustin
- 12:00 noon Lunch
- 1:00 p.m. Hyperspectral Modeling for Extracting Aerosols From Aircraft/Satellite Data
G. Daniel Hickman and Michael J. Duggin
- 1:30 p.m. The Spectral Image Processing System (SIPS)—Software for Integrated Analysis of AVIRIS Data
F.A. Kruse, A.B. Lefkoff, J.W. Boardman, K.B. Heidebrecht, A.T. Shapiro, P.J. Barloon, and A.F.H. Goetz

AGENDA (CONTINUED)

THIRD ANNUAL JPL AIRBORNE GEOSCIENCE WORKSHOP: AIRBORNE VISIBLE/INFRARED IMAGING SPECTROMETER (AVIRIS)

- 2:00 p.m. First Results From Analysis of Coordinated AVIRIS, TIMS, and ISM (French) Data for the Ronda (Spain) and Beni Bousera (Morocco) Peridotites
J.F. Mustard, S. Hurtrez, P. Pinet, and C. Sotin
- 2:30 p.m. AVIRIS Study of Death Valley Evaporite Deposits Using Least-Squares Band-Fitting Methods
J.K. Crowley and R.N. Clark
- 3:00 p.m. Break
- 3:30 p.m. A Field Measure of the "Shade" Fraction
Alan R. Gillespie, Milton O. Smith, and Donald E. Sabol
- 4:00 p.m. A Linear Spectral Matching Technique for Retrieving Equivalent Water Thickness and Biochemical Constituents of Green Vegetation
Bo-Cai Gao and Alexander F.H. Goetz
- 4:30 p.m. Poster Previews
- 5:00 p.m. Poster Previews
- 5:30 p.m. End of session.
- 5:45 p.m. Shuttle bus departs JPL for the Pasadena Ritz-Carlton Hotel.
- 6:30 p.m. Reception and poster sessions at the Pasadena Ritz-Carlton Hotel.
- 9:00 p.m. Close of reception and poster sessions.

AGENDA

THIRD ANNUAL JPL AIRBORNE GEOSCIENCE WORKSHOP: POSTER SESSION

Monday, June 1, 1992
6:30 to 9:00 p.m.
Pasadena Ritz-Carlton Hotel

1. Use of AVIRIS Data to the Definition of Optimised Specifications for Land Applications With Future Spaceborne Imaging Spectrometers
J. Bodechtel
2. Primary Studies of Trace Quantities of Green Vegetation in Mono Lake Area Using 1990 AVIRIS Data
Zhikang Chen, Chris D. Elvidge, and David P. Groeneveld
3. JPL Activities on Development of Acousto-Optic Tunable Filter Imaging Spectrometer
Li-Jen Cheng, Tien-Hsin Chao, and George Reyes
4. Measuring Dry Plant Residues in Grasslands: A Case Study Using AVIRIS
Michael Fitzgerald and Susan L. Ustin
5. Analysis of AVIRIS San Pedro Channel Data: Methods and Applications
Richard B. Frost
6. Tracking Photosynthetic Efficiency With Narrow-Band Spectroradiometry
John A. Gamon and Christopher B. Field
7. Separation of Cirrus Cloud From Clear Surface From AVIRIS Data Using the 1.38- μ m Water Vapor Band
Bo-Cai Gao and Alexander F.H. Goetz
8. Software for the Derivation of Scaled Surface Reflectances From AVIRIS Data
Bo-Cai Gao, Kathleen Heidebrecht, and Alexander F.H. Goetz
9. Integrating Remote Sensing Techniques at Cuprite, Nevada: AVIRIS, Thematic Mapper, and Field Spectroscopy
Bradley Hill, Greg Nash, Merrill Ridd, Phoebe Hauff, and Phil Ebel
10. Evaluation of AVIRISwiss-91 Campaign Data
K.I. Itten, P. Meyer, K. Staenz, T. Kellenberger, and M. Schaepman
11. AVIRIS Investigator's Guide
Howell Johnson
12. Oregon Transect: Comparison of Leaf-Level Reflectance With Canopy-Level and Modelled Reflectance
Lee F. Johnson, Frederic Baret, and David L. Peterson
13. AVIRIS as a Tool for Carbonatite Exploration: Comparison of SPAM and Mbandmap Data Analysis Methods
Marguerite J. Kingston and James K. Crowley
14. Expert System-Based Mineral Mapping Using AVIRIS
F.A. Kruse, A.B. Lefkoff, and J.B. Dietz

AGENDA

THIRD ANNUAL JPL AIRBORNE GEOSCIENCE WORKSHOP: MONDAY POSTER SESSION (CONTINUED)

15. The EARSEC Programme in Relation to the 1991 MAC-Europe Campaign
Wim J. Looyen, Jean Verdebout, Benny M. Sorensen, Giancarlo Maracci, Guido Schmuck, and Alois J. Sieber
16. Preliminary Statistical Analysis of AVIRIS/TMS Data Acquired Over the Matera Test Site
Stefania Mattei and Sergio Vetrella
17. AVIRIS Data and Neural Networks Applied to an Urban Ecosystem
Merrill K. Ridd, Niles D. Ritter, Nevin A. Bryant, and Robert O. Green
18. Temporal Variation in Spectral Detection Thresholds of Substrate and Vegetation in AVIRIS Images
Donald E. Sabol, Jr., Dar Roberts, Milton Smith, and John Adams
19. Discussion of Band Selection and Methodologies for the Estimation of Precipitable Water Vapour From AVIRIS Data
Dena Schanzer and Karl Staenz
20. Abundance Recovery Error Analysis Using Simulated AVIRIS Data
William W. Stoner, Joseph C. Harsanyi, William H. Farrand, and Jennifer A. Wong
21. Multitemporal Diurnal AVIRIS Images of a Forested Ecosystem
Susan L. Ustin, Milton O. Smith, and John B. Adams
22. A Comparison of LOWTRAN-7 Corrected Airborne Visible/Infrared Imaging Spectrometer (AVIRIS) Data With Ground Spectral Measurements
Pengyang Xu and Ronald Greeley
23. Discrimination Among Semi-Arid Landscape Endmembers Using the Spectral Angle Mapper (SAM) Algorithm
Roberta H. Yuhas, Alexander F.H. Goetz, and Joe W. Boardman
24. Empirical Relationships Among Atmospheric Variables From Rawinsonde and Field Data as Surrogates for AVIRIS Measurements: Estimation of Regional Land Surface Evapotranspiration
James E. Conel, Gordon Hoover, Anne Nolin, Ron Alley, and Jack Margolis

AGENDA

THIRD ANNUAL JPL AIRBORNE GEOSCIENCE WORKSHOP: AIRBORNE VISIBLE/INFRARED IMAGING SPECTROMETER (AVIRIS)

June 1 and 2, 1992
Von Karman Auditorium
Jet Propulsion Laboratory
Pasadena, California 91109

TUESDAY, JUNE 2, 1992

- 7:15 a.m. Shuttle bus departs Pasadena Ritz-Carlton Hotel for JPL.
- 7:30 a.m. Registration and continental breakfast at JPL.
- 8:00 a.m. Mapping the Spectral Variability in Photosynthetic and Non-Photosynthetic Vegetation, Soils and Shade Using AVIRIS
Dar A. Roberts, Milton O. Smith, Donald E. Sabol, John B. Adams, and Susan Ustin
- 8:30 a.m. Volcanic Thermal Features Observed by AVIRIS
Clive Oppenheimer, David Pieri, Veronique Carrere, Michael Abrams, David Rothery, and Peter Francis
- 9:00 a.m. Retrieval of Biophysical Parameters With AVIRIS and ISM—The Landes Forest, South West France
F. Zagolski, J.P. Gastellu-Etchegorry, E. Mougín, G. Giordano, G. Marty, T. Le Toan, and A. Beaudoin
- 9:30 a.m. Ground-Truthing AVIRIS Mineral Mapping at Cuprite, Nevada
Gregg Swayze, Roger N. Clark, Fred Kruse, Steve Sutley, and Andrea Gallagher
- 10:00 a.m. Break
- 10:30 a.m. Exploring the Remote Sensing of Foliar Biochemical Concentrations With AVIRIS Data
Geoffrey M. Smith and Paul J. Curran
- 11:00 a.m. Seasonal and Spatial Variations in Phytoplanktonic Chlorophyll in Eutrophic Mono Lake, California, Measured With the Airborne Visible and Infrared Imaging Spectrometer (AVIRIS)
John M. Melack and Mary Gastil
- 11:30 a.m. AVIRIS Calibration and Application in Coastal Oceanic Environments
Kendall L. Carder
- 12:00 noon Lunch
- 1:00 p.m. Mapping Vegetation Types With the Multiple Spectral Feature Mapping Algorithm in Both Emission and Absorption
Roger N. Clark, Gregg A. Swayze, Christopher Koch, and Cathy Ager

AGENDA (CONTINUED)

THIRD ANNUAL JPL AIRBORNE GEOSCIENCE WORKSHOP:
AIRBORNE VISIBLE/INFRARED IMAGING SPECTROMETER
(AVIRIS)

- 1:30 p.m. Multiple Dataset Water-Quality Analyses in the Vicinity of an Ocean Wastewater Plume
Michael Hamilton, Curtiss O. Davis, W. Joseph Rhea, and Jeannette van den Bosch
- 2:00 p.m. MAC Europe 91: Evaluation of AVIRIS, GER Imaging Spectrometry Data for the Land Application Testsite Oberpfaffenhofen
F. Lehmann, R. Richter, H. Rothfuss, K. Werner, P. Hausknecht, A. Müller, and P. Strobl
- 2:30 p.m. Using Endmembers in AVIRIS Images To Estimate Changes in Vegetative Biomass
Milton O. Smith, John B. Adams, Susan L. Ustin, and Dar A. Roberts
- 3:00 p.m. Break
- 3:30 p.m. Atmospheric Correction of AVIRIS Data in Ocean Waters
Gregory Terrie and Robert Arnone
- 4:00 p.m. The 1991 AVIRIS/POLDER Experiment in Camargue, France
F. Baret, C. Leprieur, S. Jacquemoud, V. Carrère, X.F. Gu, M. Steven, V. Vanderbilt, J.F. Hanocq, S. Ustin, G. Rondeaux, C. Daughtry, L. Biehl, R. Pettigrew, D. Modro, H. Horoyan, T. Sarto, C. Despontin, and H. Razafindraibe
- 4:30 p.m. AVIRIS Sensor and Ground Data System: Status and Plans
Thomas Chrien and Earl Hansen
- 5:00 p.m. Wrap up.
- 5:30 p.m. End of AVIRIS Workshop.
- 5:45 p.m. Shuttle bus departs JPL for the Pasadena Ritz-Carlton Hotel.

AGENDA

THIRD ANNUAL JPL AIRBORNE GEOSCIENCE WORKSHOP: THERMAL INFRARED MULTISPECTRAL SCANNER (TIMS)

June 3, 1992
Von Karman Auditorium
Jet Propulsion Laboratory
Pasadena, California 91109

WEDNESDAY, JUNE 3, 1992

- 7:15 a.m. Shuttle bus departs Pasadena Ritz-Carlton Hotel for JPL.
- 7:30 a.m. Registration and continental breakfast at JPL.
- 8:00 a.m. Welcome
- 8:30 a.m. TIMS Performance Evaluation Summary
Bruce Spiering, G. Meeks, J. Anderson, S. Jaggi, and S. Kuo
- A Quantitative Analysis of TIMS Data Obtained on the Learjet 23 at Various Altitudes
S. Jaggi
- Analysis of TIMS Performance Subjected to Simulated Wind Blast
S. Jaggi and S. Kuo
- 9:30 a.m. Sensitivity of Blackbody Reference Panels to Wind Blast
Gordon Hoover
- 10:00 a.m. Break
- 10:30 a.m. Preliminary Analysis of TIMS Performance on the ER-2
S.J. Hook, V.J. Realmuto, and R.E. Alley
- 11:00 a.m. Comparison of Preliminary Results From Airborne ASTER Simulator (AAS) With TIMS Data
Yoshiaki Kannari, Franklin Mills, Hiroshi Watanabe, Teruya Ezaka, Tatsuhiko Narita, and Sheng-Huei Chang
- 11:30 a.m. Simulation of ASTER Data Using AVIRIS Images
Michael Abrams
- 12:00 noon Lunch
- 1:00 p.m. Application of Split Window Technique to TIMS Data
Tsuneo Matsunaga, Shuichi Rokugawa, and Yoshinori Ishii
- 1:30 p.m. Atmospheric Corrections for TIMS Estimated Emittance
T.A. Warner and D.W. Levandowski
- 2:00 p.m. An Algorithm for the Estimation of Bounds on the Emissivity and Temperatures From Thermal Multispectral Airborne Remotely Sensed Data
S. Jaggi, D. Quattrochi, and R. Baskin

AGENDA (CONTINUED)

THIRD ANNUAL JPL AIRBORNE GEOSCIENCE WORKSHOP:
THERMAL INFRARED MULTISPECTRAL SCANNER
(TIMS)

- 2:30 p.m. Multi-Resolution Processing for Fractal Analysis of Airborne Remotely Sensed Data
S. Jaggi, D. Quattrochi, and N. Lam
- 3:00 p.m. Break
- 3:30 p.m. Preliminary Analysis of Thermal-Infrared Multispectral Scanner Data of the Iron Hill, Colorado Carbonatite-Alkalic Rock Complex
Lawrence C. Rowan, Kenneth Watson, and Susanne H. Miller
- 4:00 p.m. The Use of TIMS for Mapping Different Pahoehoe Surfaces: Mauna Iki, Kilauea
Scott K. Rowland
- 4:30 p.m. Ejecta Patterns of Meteor Crater, Arizona Derived From the Linear Un-Mixing of TIMS Data and Laboratory Thermal Emission Spectra
Michael S. Ramsey and Philip R. Christensen
- 5:00 p.m. The Use of TIMS Data To Estimate the SO₂ Concentrations of Volcanic Plumes: A Case Study at Mount Etna, Sicily
Vincent J. Realmuto
- 5:30 p.m. End of TIMS Workshop.
- 5:45 p.m. Shuttle bus departs JPL for the Pasadena Ritz-Carlton Hotel.

AGENDA

THIRD ANNUAL JPL AIRBORNE GEOSCIENCE WORKSHOP: AIRBORNE SYNTHETIC APERTURE RADAR (AIRSAR)

June 4 and 5, 1992
Von Karman Auditorium
Jet Propulsion Laboratory
Pasadena, California 91109

THURSDAY, JUNE 4, 1992

- 7:15 a.m. Shuttle bus departs Pasadena Ritz-Carlton Hotel for JPL.
- 7:30 a.m. Registration and continental breakfast at JPL.
- 8:00 a.m. Welcome
- 8:30 a.m. The NASA/JPL Three-Frequency AIRSAR System
J. van Zyl, R. Carande, Y. Low, T. Miller, and K. Wheeler
- 9:00 a.m. A Snow Wetness Retrieval Algorithm for SAR
Jiancheng Shi and Jeff Dozier
- 9:30 a.m. Comparison of JPL-AIRSAR and DLR E-SAR Images from the MAC Europe '91 Campaign Over Testsite Oberpfaffenhofen: Frequency and Polarization Dependent Backscatter Variations From Agricultural Fields
C. Schmullius and J. Nithack
- 10:00 a.m. Break
- 10:30 a.m. Monitoring Environmental State of Alaskan Forests With AIRSAR
Kyle C. McDonald, JoBea Way, Eric Rignot, Cindy Williams, Les Viereck, and Phylis Adams
- 11:00 a.m. Comparison of Modeled Backscatter With SAR Data at P-Band
Yong Wang, Frank W. Davis, and John M. Melack
- 11:30 a.m. SAR Backscatter From Coniferous Forest Gaps
John L. Day and Frank W. Davis
- 12:00 noon Lunch
- 1:00 p.m. Panel Discussion on Future Emphasis of the AIRSAR System
J. van Zyl, Moderator
- 1:30 p.m. Retrieval of Pine Forest Biomass Using JPL AIRSAR Data
A. Beaudoin, T. Le Toan, F. Zagolski, C.C. Hsu, H.C. Han, and J.A. Kong
- 2:00 p.m. Characterization of Wetland, Forest, and Agricultural Ecosystems in Belize With Airborne Radar (AIRSAR)
Kevin O. Pope, Jose Maria Rey-Benayas, and Jack F. Paris
- 2:30 p.m. Strategies for Detection of Floodplain Inundation With Multi-Frequency Polarimetric SAR
Laura L. Hess and John M. Melack

AGENDA (CONTINUED)

THIRD ANNUAL JPL AIRBORNE GEOSCIENCE WORKSHOP:
AIRBORNE SYNTHETIC APERTURE RADAR
(AIRSAR)

- 3:00 p.m. Break
- 3:30 p.m. Supervised Fully Polarimetric Classification of the Black Forest Test Site: From MAESTRO1 to MAC Europe
G. De Grandi, C. Lavalle, H. De Groof, and A. Sieber
- 4:00 p.m. Relating Multifrequency Radar Backscattering to Forest Biomass: Modeling and AIRSAR Measurement
Guoqing Sun and K. Jon Ranson
- 4:30 p.m. Poster Previews
- 5:00 p.m. Poster Previews
- 5:30 p.m. End of session.
- 5:45 p.m. Shuttle bus departs JPL for the Pasadena Ritz-Carlton Hotel.
- 6:30 p.m. Reception and poster sessions at the Pasadena Ritz-Carlton Hotel.
- 9:00 p.m. Close of reception and poster sessions.

AGENDA

THIRD ANNUAL JPL AIRBORNE GEOSCIENCE WORKSHOP: POSTER SESSION

Thursday, June 4, 1992
6:30 to 9:00 p.m.
Pasadena Ritz-Carlton Hotel

1. Processing of AIRSAR Polarimetric Data for Soil Moisture Estimation Over Mahantango Watershed Area
K.S. Rao
2. Evaluation of Polarimetric SAR Parameters for Soil Moisture Retrieval
Jiancheng Shi, Jakob J. van Zyl, and Edwin T. Engman
3. Interaction Types and Their Like-Polarization Phase-Angle Difference Signatures
Jack F. Paris
4. Application of Modified VICAR/IBIS GIS to Analysis of July 1991 Flevoland AIRSAR Data
L. Norikane, B. Broek, and A. Freeman
5. Radar Analysis and Visualization Environment (RAVEN): Software for Polarimetric Radar Analysis
K.S. Kierein-Young, A.B. Lefkoff, and F.A. Kruse
6. Measuring Ocean Coherence Time With Dual-Baseline Interferometry
Richard E. Carande
7. A Bibliography of Global Change, Airborne Science, 1985-1991
Edwin J. Sheffner and James G. Lawless
8. ATTIRE (Analytical Tools for Thermal Infrared Engineering)—A Thermal Sensor Simulation Package
S. Jaggi
9. Kilauea Data Set Compiled for Distribution on Compact Disc
Lori Glaze, George Karas, Sonia Chernobieff, Elsa Abbott, and Earnie Paylor
10. The JPL Spectral Library 0.4 to 2.5 Micrometers
Simon J. Hook, Cindy I. Grove, and Earnest D. Paylor II
11. Lossless Compression of AVIRIS Data: Comparison of Methods and Instrument Constraints
R.E. Roger, J.F. Arnold, M.C. Cavenor, and J.A. Richards
12. Simulation of AVHRR-K Band Ratios With AVIRIS
Melanie A. Wetzel and Ronald M. Welch
13. Soil Conservation Applications With C-Band SAR
B. Brisco, R.J. Brown, J. Naunheimer, and D. Bedard

AGENDA

THIRD ANNUAL JPL AIRBORNE GEOSCIENCE WORKSHOP: THURSDAY POSTER SESSION (CONTINUED)

14. Comparison of Edges Detected at Different Polarisation in MAESTRO Data
Ronald G. Caves, Peter J. Harley, and Shaun Quegan
15. Identification of Erosion Hazards in a Mediterranean Environment
M. Altherr, J. Hill, and W. Mehl

AGENDA

THIRD ANNUAL JPL AIRBORNE GEOSCIENCE WORKSHOP: AIRBORNE SYNTHETIC APERTURE RADAR (AIRSAR)

June 4 and 5, 1992
Von Karman Auditorium
Jet Propulsion Laboratory
Pasadena, California 91109

FRIDAY, JUNE 5, 1992

- 7:15 a.m. Shuttle bus departs Pasadena Ritz-Carlton Hotel for JPL.
- 7:30 a.m. Registration and continental breakfast at JPL.
- 8:00 a.m. Oceanic Features Detected by SAR in the Mediterranean Sea During the MAC Europe '91 Campaign
Werner Alpers
- 8:30 a.m. SAR Observations in the Gulf of Mexico
David Sheres
- 9:00 a.m. Investigation of AIRSAR Signatures of the Gulf Stream
G.R. Valenzuela, J.S. Lee, D.L. Schuler, G.O. Marmorino, F. Askari, K. Hoppel, J.A.C. Kaiser, and W.C. Keller
- 9:30 a.m. Mapping of Sea Bottom Topography
C.J. Calkoen, G.J. Wensink, and G.H.F.M. Hesselmans
- 10:00 a.m. Break
- 10:30 a.m. Sea Bottom Topography Imaging With SAR
M.W.A. van der Kooij, G.J. Wensink, and J. Vogelzang
- 11:00 a.m. AIRSAR Surveys of Upper-Ocean Fronts Off California and Hawaii
P. Flament
- 11:30 a.m. Preliminary Results of Polarization Signatures for Glacial Moraines in the Mono Basin, Eastern Sierra Nevada
Richard R. Forster, Andrew N. Fox, and Bryan Isacks
- 12:00 noon Lunch
- 1:00 p.m. Detecting Surface Roughness Effects on the Atmospheric Boundary Layer Via AIRSAR Data: A Field Experiment in Death Valley, California
Dan G. Blumberg and Ronald Greeley
- 1:30 p.m. Extraction of Quantitative Surface Characteristics From AIRSAR Data for Death Valley, California
K.S. Kierein-Young and F.A. Kruse
- 2:00 p.m. The TOPSAR Interferometric Radar Topographic Mapping Instrument
Howard A. Zebker, Søren N. Madsen, Jan Martin, Giovanni Alberti, Sergio Vetrella, and Alessandro Cucci

AGENDA (CONTINUED)

THIRD ANNUAL JPL AIRBORNE GEOSCIENCE WORKSHOP: AIRBORNE SYNTHETIC APERTURE RADAR (AIRSAR)

- 2:30 p.m. Evaluation of the TOPSAR Performance by Using Passive and Active Calibrators
G. Alberti, A. Moccia, S. Ponte, and S. Vetrella
- 3:00 p.m. Break
- 3:30 p.m. Fitting a Three-Component Scattering Model to Polarimetric SAR Data
A. Freeman and S. Durden
- 4:00 p.m. Application of Symmetry Properties to Polarimetric Remote Sensing With JPL
AIRSAR Data
S.V. Nghiem, S.H. Yueh, R. Kwok, and F.K. Li
- 4:30 p.m. External Calibration of Polarimetric Radar Images Using Distributed Targets
Simon H. Yueh, S.V. Nghiem, and R. Kwok
- 5:00 p.m. Wrap up.
- 5:30 p.m. End of AIRSAR Workshop.
- 5:45 p.m. Shuttle bus departs JPL for the Pasadena Ritz-Carlton Hotel.

A SNOW WETNESS RETRIEVAL ALGORITHM FOR SAR

Jiancheng Shi

Center for Remote Sensing and Environmental Optics
University of California, Santa Barbara, CA 93106

Jeff Dozier

NASA Goddard Space Flight Center, Code 900,
Greenbelt, MD 20771

The objectives of this study are (1) to evaluate the backscattering signals response to snow wetness and (2) to develop an algorithm for snow wetness measurement using C-band polarimetric SAR. In hydrological investigations, modeling and forecasting of snowmelt runoff requires information about snowpack properties and their spatial variability. In particular, timely measurement of snow parameters is needed for operational hydrology. The liquid water content of snowpack is one of the important parameters. Active microwave sensors are highly sensitive to liquid water in the snowpack because of the large dielectric contrast between ice and water in the microwave spectrum. They are not affected by weather and have a spatial resolution compatible with the topographic variation in alpine regions. However, a quantitative algorithm for retrieval snow wetness has not been developed.

The data, from a polarimetric SAR overflight by the NASA/JPL DC-8 over the glaciers in the Ötztal Alps, Austria, were analyzed. In order to utilize the polarimetric SAR data for quantitatively measuring snow wetness purpose, we must consider the accuracy of the radar measurements. For radiometric calibration, and as geometric reference points, trihedral corner reflectors with leg lengths of 0.65, 1.25 and 1.8 meters were deployed on the glaciers. Using topographic information, SAR data can be calibrated (van Zyl and Shi, 1992) so that it contains the more accurate information of the polarization signatures response to snow physical parameters. With the generated incidence angle and radar antenna angle map, the topographic effect on SAR image data is minimized so that a direct comparison in the model simulations and inversion snow wetness become possible.

Backscattering measurements by SAR from wet snow covered terrain are affected by two sets of parameters (Shi and Dozier, 1992a): (1) sensor parameters which include the frequency, polarization, and viewing geometry, and (2) snowpack parameters which include snow density, liquid water content, particle sizes and shapes of ice and water, type of the correlation function and its parameters of surface roughness.

In addition to snowpack physical parameters, the surface roughness and incidence angle have a great impact on the relationship between the backscattering coefficients and snow wetness. A negative correlation between the backscattering coefficients and snow wetness was found by the truck-mounted Microwave Active Spectrometer at frequency 8.6 GHz for incidence angles greater than 5° (Stiles and Ulaby, 1980). However, positive correlation was found in this study when comparing AIRSAR measurements for VV and HH polarizations at identical incidence angles were about 5 dB higher from high liquid water content snow samples than from low liquid water content snow samples. A 3 dB difference was found in HV polarization.

Both measurements and model predictions show that the scattering mechanisms of wet snow are characterized as (1) for low liquid water content snow, surface

scattering is dominant at small incidence angles and volume scattering dominates at large incidence angles. (2) for high liquid water content snow with a relatively rough surface, surface scattering dominates at all incidence angles.

The actual relationship between the co-polarization signals and snow wetness is controlled by the scattering mechanisms. When the surface is smooth, volume scattering is the dominant scattering source. As snow wetness increases, both the volume scattering albedo and the transmission coefficients greatly decrease. This results in a negative correlation between the backscattering signals and snow wetness. When the surface is not smooth, increasing snow wetness results in greatly increased surface scattering interaction and surface scattering becomes the dominant scattering process. Therefore, a positive correlation between the backscattering signals and snow wetness will be observed.

To develop an algorithm of measuring snow wetness, we need to minimize or combine these factors since the polarimetric SAR only provides a limited number of independent observations. The task is to select appropriate measurements for relating snow wetness to the backscattering measurements.

Based on the identified scattering mechanics of wet snow-covered terrain from the model predictions and measurements of the polarimetric properties (Shi and Dozier, 1992a), we construct the inversion model with two components:

$$\sigma_t^{pp} = \sigma_s^{pp} + \sigma_v^{pp} \quad (1)$$

where pp indicates polarization. σ_t is the total backscattering coefficient. σ_s is the surface backscattering from the air-snow interface and σ_v is the volume backscattering from the snowpack.

Since the relations of the ratios derived by the first-order surface and volume scattering model in co-polarization signals, two ratios of the combined VV and HH polarization signals can be represented as

$$\frac{\sigma_t^{hh}}{\sigma_t^{vv} + \sigma_t^{hh}} = \frac{1}{D_T(\theta_i, \epsilon_r)(1 - C_{hh}) + C_{hh}D_R(\theta_i, \epsilon_r) + 1} \quad (2)$$

and

$$\frac{\sigma_t^{vv}}{\sigma_t^{vv} + \sigma_t^{hh}} = \frac{D_T(\theta_i, \epsilon_r)(1 - C_{hh}) + C_{hh}D_R(\theta_i, \epsilon_r)}{D_T(\theta_i, \epsilon_r)(1 - C_{hh}) + C_{hh}D_R(\theta_i, \epsilon_r) + 1} \quad (3)$$

where D_R and D_T are the surface and volume backscattering ratios of VV and HH polarizations (Shi and Dozier, 1992b), which are only a function of incidence angle and the permittivity of wet snow. The C_{hh} is the surface backscattering contribution in the HH polarization of the total backscattering signal. From the above two measurements, the two unknowns, ϵ_r and C_{hh} , can be solved. The algorithm derived above does not require any information about the surface roughness and the volume scattering albedo. It only involves the calculation of snowpack permittivity.

To test the algorithm for measuring snow wetness over a large area, a snow map was first obtained by performing the supervised Bayes classification (Shi et al., 1991) and non-snow-covered area was masked. Secondly, the backscattering coefficients of VV and HH polarizations for a given pixel were determined by the median value within a 5×5 window to reduce the effect of image speckle. The algorithm was applied after the measurements of $\sigma^{hh}/(\sigma^{vv} + \sigma^{hh})$ and $\sigma^{vv}/(\sigma^{vv} + \sigma^{hh})$ were tested by the physical conditions (Shi and Dozier, 1992b).

Figure shows an image of the inversion-derived snow wetness. The image brightness is proportional to the snow wetness and ranges from 1 to 8 percent by volume. The black region is non-snow-covered area. At the time of the radar survey the snow cover was wet at all elevation zones. The liquid water content of the top snow layer was in the order of 5 to 6 percent by volume at the elevation

of 3,000 meters, decreasing to 2 or 3 percent at the highest elevations. The snow densities and depths ranged from 492 to 580 kg m⁻³ and from 45 to 114 cm respectively. Using co-registered DEM data, we compared the inversion-derived snow wetness within the elevation zones. The result shows that the algorithm performs well and that the absolute error, generally, is less than 2 percent.

This study shows recent results of our efforts to develop and verify an algorithm for snow wetness retrieval from a polarimetric SAR. Our algorithm is based on the first-order scattering model with consideration of both surface and volume scattering. It operates at C-band and requires only rough information about the ice volume fraction in snowpack. By evaluating the relationship between the backscattering coefficients of both surface and volume scattering for the co-polarization signals, the estimate of snow wetness can be derived from the ratios of the combined co-polarization signals. The inversion algorithm performs well using AIRSAR data and should prove useful for routine and large-area snow wetness measurements.

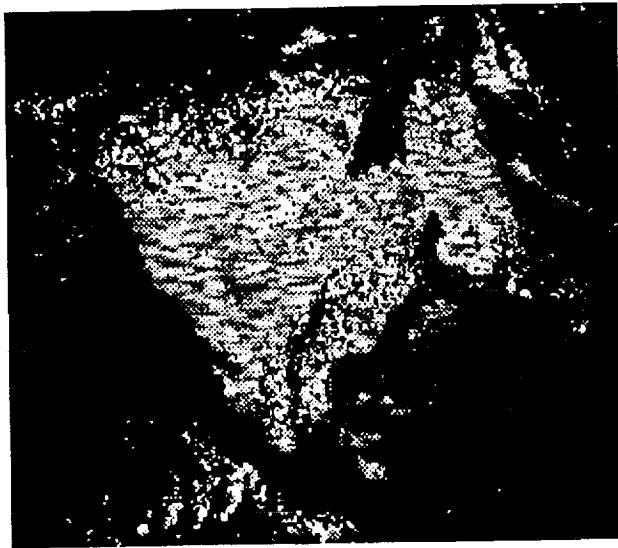


Figure Inversion-derived snow wetness. The image brightness is proportional to the snow wetness and ranges from 1 to 8 percent by volume. The black region is nonsnow-covered area.

References

- [1] J. J. van Zyl and J. Shi, "The effect of topography on SAR calibration," submitted to *IEEE Transactions on Geoscience and Remote Sensing*, 1992.
- [2] J. Shi and J. Dozier. "Radar response to snow wetness." submitted to *Proceedings IGARSS '92*.
- [3] F.T. Ulaby and W.H. Stiles, "The active and passive microwave response to snow parameters, 2, water equivalent of dry snow," *J. Geophys. Res.*, vol. 85, no. C2, pp. 1045-1049, 1980.
- [4] J. Shi and J. Dozier. "Retrieval snow wetness from SAR." submitted to *Annals of glaciology*, 1992.
- [5] J. Shi, J. Dozier, H. Rott, and R. E. Davis. Snow and glacier mapping in alpine regions with polarimetric SAR. *Proceedings IGARSS '91, IV*, pp. 2311-3214.

COMPARISON OF JPL-AIRSAR AND DLR E-SAR IMAGES
FROM THE MAC EUROPE '91 CAMPAIGN OVER TESTSITE OBER-
PFAFFENHOFEN: FREQUENCY AND POLARIZATION DEPENDENT
BACKSCATTER VARIATIONS FROM AGRICULTURAL FIELDS

C. Schmullius, J. Nithack

N 94-16733-1

Institute of Radio-Frequency Technology
German Aerospace Establishment (DLR)
D-8031 Oberpfaffenhofen, Germany

1. INTRODUCTION

On July 12, the MAC Europe '91 (Multi-Sensor Airborne Campaign) took place over test site Oberpfaffenhofen. The DLR Institute of Radio-Frequency Technology participated with its C-VV, X-VV, and X-HH Experimental SAR (E-SAR). The high resolution E-SAR images with a pixel size between 1 and 2 m and the polarimetric AIRSAR images were analyzed. Using both sensors in combination is a unique opportunity to evaluate SAR images in a frequency range from P- to X-band and to investigate polarimetric information.

2. EXPERIMENT AND DATA DESCRIPTION

The JPL AIRSAR was flown over testsite Oberpfaffenhofen on July 12, 1991 at noon. The DLR E-SAR was flown on different daytimes between July 8 and 12. The E-SAR data were processed at the DLR facility with the Motion Compensation SAR Processor [Moreira 1990]. The pixel resolution for the 8-look images (slant range presentation) is 1.8 x 1.2 m. The antenna pattern was corrected using a multiplicative polynomial correction function. The image digital numbers correspond to 16 bit amplitude values.

Ground truth consisted in mapping of landuse and the phenological situation, and intensive soil sampling on large, flat agricultural fields belonging to three different soil types: a loessy soil, drained turfy material, and a gravel-rich glacial terrace. Biomass and leaf area index were measured on several corn fields.

3. IMAGE INTERPRETATION

Digital image processing was performed on an EASI/PACE system (PCI Inc.) using a DECstation 5000/200. Since the E-SAR samples one frequency-polarization combination at a time, the image channels of the test site had to be geometrically rectified to each other. Figure 1 shows a color composite of three E-SAR images illustrating different backscattering mechanisms for C- and X-band but, furthermore, also for X-HH and -VV polarization. These differences are due to varying states of crop maturity. The wetness, mainly in the crop's ears, causes absorption losses of the VV-polarized signals.

This finding is in agreement with measurements of the absorption loss factor of wheat stalks [Allen and Ulaby 1984] and negative correlations between biomass and C-VV backscatter for corn fields and potato fields, see figure 2. For vertical polarization the loss factor increases with plant volumetric moisture (ie. the backscattered power decreases), and for horizontal polarization the loss factor decreases with wetness. Hence, the HH-polarized returns penetrate the crop's ear layer somewhat and backscattering occurs on lower parts of the plants where the different state of maturity does not cause, at this time of the year (July 8), differences in water content.

Figure 3 shows an unsupervised Migrating-Means (or K-Cluster) approach to classify an agricultural area close to the DLR. Only the E-SAR C-VV and X-VV channels were used. Image processing techniques such as post-classification filtering or a combination with image segmentation algorithms [Rignot et al. 1991] can improve the classification results.

4. CONCLUSION AND OUTLOOK

The VV-polarized C- and X-band scattering is dependent on the different degrees of maturity in the barley fields. HH-polarized X-band signals have a larger penetration depth and the backscattering intensity is not dependent on the water content of the uppermost vegetation layer. SAR images of one week later do not show these backscattering variations since the crops had been ripening in that time period.

JPL polarimetric AIRSAR data from this test site is being analysed with special regard to the polarization-dependent backscatter phenomena, since it could be shown that a combination of a different frequency plus a different polarization gives best statistical separability. Future campaigns such as CLEOPATRA 1992 will include additional ground truth measurements that are regarded to be of importance and have been missing in the MAC Europe '91 Campaign, such as plant geometry.

5. REFERENCES

- C. Allen and F. Ulaby, "Modeling the Polarization Dependence of the Attenuation in Vegetation Canopies," in Proceedings of the International Geoscience and Remote Sensing Symposium, Strasbourg, France, 27.-30.8. 1984.
- J. Moreira, "Motion Compensation SAR-Processing Facility at DLR," in Proceedings of the 10th EARSeL Symposium, Toulouse, 5.-8. June 1990, pp. 279-288.
- E. Rignot, R. Chellappa, R. Dubois, R. Kwok, and J. van Zyl, "Unsupervised Segmentation of Polarimetric SAR Data using the Covariance Matrix," in Proceedings of the International Geoscience and Remote Sensing Symposium, Espoo, 3.-6. June 1991, pp. 1813-1816.



Fig. 1



Fig. 3

Fig. 1
Color composite of a three channel image
(red: C-VV, green: X-VV, blue: X-HH, MAC
Europe '91).

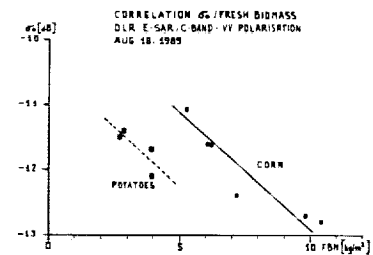


Fig. 2 Correlations of σ_0
(derived from the mean grey value per field)
with the fresh biomass of corn and potatoes
(C-band image, Aug. 1989).

Fig. 3:
Non-supervised classification of a two fre-
quency image (X-band, C-band both
VV-polarisation, MAC Europe '91).

Legend:

Blue:	water
yellow + green:	Summer cereals
Green:	Gras
(+ little orange)	
Orange:	Oats
(+ little green)	
light blue:	not cultivated
Margenta:	Winter barley
Red/Violett:	Corn + potatoes
Red/Brown:	Rape

MONITORING ENVIRONMENTAL STATE OF ALASKAN FORESTS WITH AIRSAR

Kyle C. McDonald, JoBea Way and Eric Rignot

Jet Propulsion Laboratory
California Institute of Technology
4800 Oak Grove Drive
Pasadena, California
91109-8001

Cindy Williams, Les Viereck and Phyllis Adams

University of Alaska
Institute of Northern Forestry
308 Tanana Drive
Fairbanks, Alaska
99701-5500

During March 1988 and May 1991, the JPL airborne synthetic aperture radar, AIRSAR, collected sets of multi-temporal imagery of the Bonanza Creek Experimental Forest near Fairbanks, Alaska. These data sets consist of series of multi-polarized images collected at P-, L- and C-bands each over a period of a few days. The AIRSAR campaigns were complemented with extensive ground measurements that included observations of both static canopy characteristics such as forest architecture as well as properties that vary on short term time scales such as canopy dielectric conditions. Observations exist for several stands of deciduous and coniferous species including white spruce (*Picea glauca*), black spruce (*Picea mariana*) and balsam poplar (*Populus balsamifera*).

Although the duration of each campaign was fairly short, significant changes in environmental conditions caused notable variations in the physiological state of the canopies. During the 1988 campaign, environmental conditions ranged from unseasonably warm to more normal subfreezing temperatures. This permitted AIRSAR observations of frozen and thawed canopy states. During May 1991, ice jams that occurred along the river caused many stands to flood while the subsequent clearing of the river then allowed the waters to recede, leaving a snow covered ground surface. This allowed observations of several stands during both flooded and non-flooded conditions. Furthermore, the local weather varied from clear sunny days to heavy overcast days with some occurrence of rain. Measurements of leaf water potential indicated that this caused significant variations in canopy water status, allowing SAR observations of water stressed and unstressed trees.

Mean backscatter from several stands is examined for the various canopy physiological states. The changes in canopy backscatter that occur as a function of environmental and physiological state are analyzed. Preliminary results of a backscatter

signature modeling analysis are presented. The implications of using SAR to monitor canopy phenological state are addressed.

This work was carried out at the Jet Propulsion Laboratory, California Institute of Technology, under contract to the National Aeronautics and Space Administration, and at the Institute of Northern Forestry, University of Alaska.

COMPARISON OF MODELED BACKSCATTER WITH SAR DATA AT P-BAND

Yong Wang, Frank W. Davis, and John M. Melack*

Department of Geography, University of California at Santa Barbara, CA 93106.

*Department of Biological Science, University of California at Santa Barbara, CA 93106

1. Introduction

In recent years several analytical models have been developed to predict microwave scattering by trees and forest canopies [1-6]. These models contribute to the understanding of radar backscatter over forested regions to the extent that they capture the basic interactions between microwave radiation and tree canopies, understories, and ground layers as functions of incidence angle, wavelength, and polarization. The Santa Barbara microwave model backscatter model for woodland (i.e. with discontinuous tree canopies) combines a single-tree backscatter model and a gap probability model [5-6]. Comparison of model predictions with synthetic aperture radar (SAR) data at L-band ($\lambda = 0.235$ m) is promising [7], but much work is still needed to test the validity of model predictions at other wavelengths. Here we test the validity of the model predictions at P-band ($\lambda = 0.68$ m) for woodland stands at our Mt. Shasta test site.

2. Study area

Extensive ground data have been collected to support our SIR-B (Shuttle Imaging Radar) and SIR-C/X-SAR studies. The site is located to the southeast of Mt. Shasta, California (41°18' N, 122°05' W), and spans elevations from 1160 to 1220 m. The forest stands under investigation are natural, are on level ground, and are dominated by ponderosa pine (*Pinus ponderosa*) or pine mixed with white fir (*Abies concolor*). Under story vegetation is sparse and consists primarily of perennial grasses and forbes. The litter layer can reach a depth of about 0.1 m. Three ponderosa pine stands ("Sp2", "St2", and "St11") in the site were chosen for this study because adequate ground data for these stands are available to provide inputs to the model. The three stands have different stand densities and trunk diameters at breast height (dbh). "Sp2" has trees of 25.0 m h and 0.77 m dbh, with stand density of 23 trees per hectare. "St11" has trees of 27.0 m h and 0.46 m dbh, with stand density of 228 trees per hectare. "St2" has trees of 25 m h and 0.42 m dbh, with stand density of 303 trees per hectare. The soil of the stands is derived from recent alluvial deposits of volcanic ash, and the ground surface is smooth at P-band. Other ground data used as model inputs can be found in [8].

3. SAR data

SAR data were acquired by the Jet Propulsion Laboratory (JPL) airborne SAR overflights on 6 September 1989 after a dry summer. The SAR data were processed and calibrated by JPL. The estimated calibration uncertainty of the backscatter is ± 1.0 dB [3]. The estimated calibration uncertainty of VV-HH phase difference is $\pm 10^\circ$, and the estimated calibration uncertainty of HH and VV correlation coefficient is ± 0.1 (personal communication, Freeman 1992). We received the standard 4-look compressed data with pixel spacing of 12.1 m (azimuth) and 6.7 m (slant range). For the three stands, the means of the backscatter (HH, HV, and VV polarizations), the VV-HH phase difference, and the HH and VV correlation coefficient were extracted from the SAR data.

4. Comparison of model results with SAR data at P-band

Model simulations for stands "St2", "St11", and "Sp2" were carried out at the same incidence angle (θ_o) as the SAR data. We have 8 SAR data takes covering stand "St2" (θ_o ranges from 22° to 54°), 5 data takes covering stand "St11" (θ_o from 25° to 45°), and 5 data takes covering stand "Sp2" (θ_o from 27° to 47°). The HH, HV, and VV backscatter, and the HH and VV correlation coefficient are shown in Figure 1. The model makes good predictions of the HH backscatter for stands "St2" and "St11" (Figure 1a), the VV backscatter for all three stands (Figure 1b), and the HV backscatter for stand "St11" (Figure 1c). The model overestimates the HH backscatter for stand "Sp2" (Figure 1a). The model underestimates the HV backscatter for stand "Sp2" and stand "St2" (Figure 1c). We attribute the underestimate to the surface model, in which we model only the co-polarized surface backscatter. Since the soil is dry and the radar wavelength is long, deep penetration into the soil is expected. Because "Sp2" has the low stand density and "St2" has small trees, more soil surface is exposed in these stands. Thus, the backscatter from the sub-surface may be a major contributor.

The model predicts well for the HH and VV correlation coefficients of stands "St2" and "St11", but overestimates the coefficient of stand "Sp2" (Figure 1d). The overestimate can be attributed to inadequate modeling of surface backscatter. The surface model used gives completely correlated backscatter for HH and VV because identical surface parameters are used for all the simulated pixels in a stand, and because the surface model predicts zero cross-polarized backscatter. For the sparse stand "Sp2", the surface backscatter is the major scattering source. Thus, strong and completely correlated surface backscatter is predicted by the model.

The model predicts a phase difference of $\approx 210.0^\circ$ for the dense stands "St2" and "St11". Since the model phase difference and the SAR observed phase differences are close to 180° for stands "St2" and "St11", there is some indication that the VV-HH phase difference from double-bounce trunk-ground interactions (180°) contributes to the total phase difference.

To investigate the model prediction quantitatively, we test the null hypothesis of $H_o: \mu_{model} = \mu_{sar}$, where μ_{model} is the modeled mean and μ_{sar} is the mean of the SAR data. At the 5% significance level, the H_o tests of the HH, HV, and VV backscatter, the correlation coefficient of HH and VV polarizations, and the VV-HH phase difference are accepted.

5. Conclusions

For P-band, the model predicts well compared with SAR data for HH, HV, and VV backscatter, VV-HH phase difference, and HH and VV correlation coefficient for stands with medium-to-high density (228 -- 303 trees per hectare). When stand density is low (23 trees per hectare), model performance becomes unacceptable: the model overestimates HH and VV backscatter, underestimates HV backscatter, and overestimates HH and VV correlation coefficient.

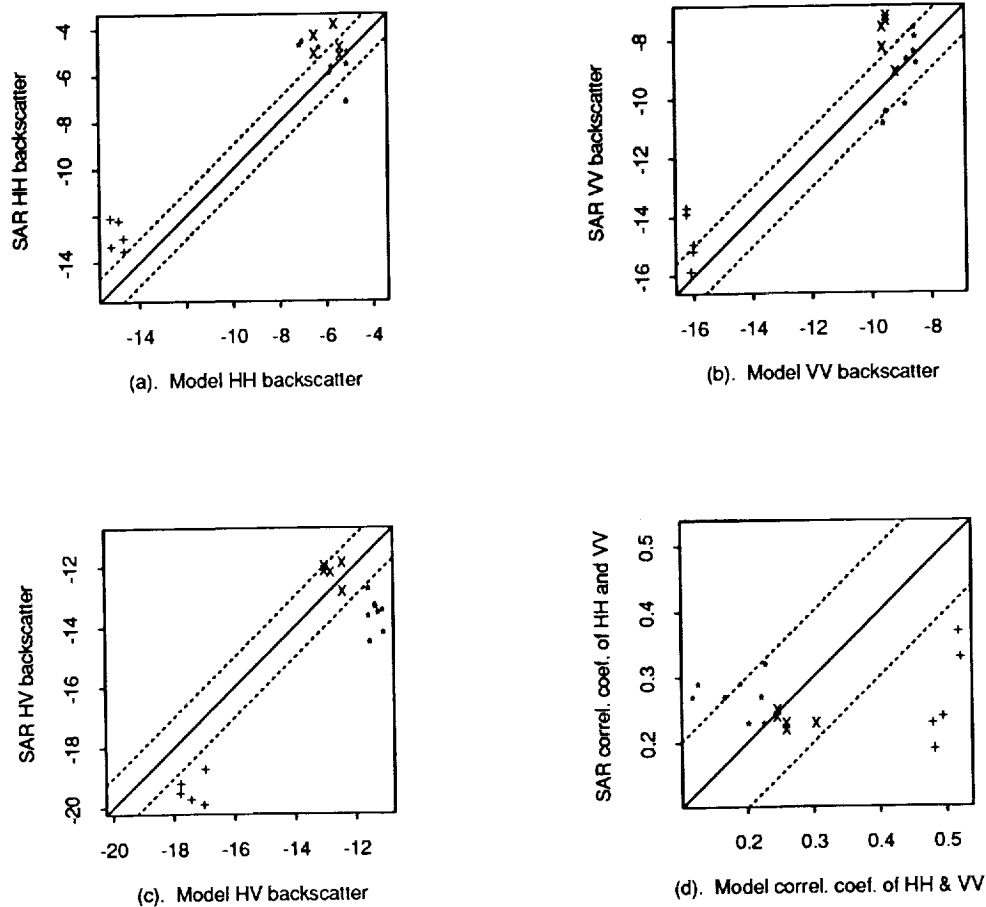
6. References:

- [1] J. A. Richards, G. Sun and D. S. Simonett, "L-band radar backscatter modeling of forest stands", *IEEE Trans. on Geosci. and Remote Sensing*, vol. GE-25, no. 4, pp. 487-498, 1987.
- [2] M. A. Karam and A. K. Fung, "Electromagnetic scattering from a layer of finite length, randomly oriented, dielectric, circular cylinders over a rough interface with application to vegetation", *Int. J. of Remote Sensing*, vol. 9, no. 6, pp. 1109-1134, 1988.
- [3] S. L. Durden, J. J. van Zyl, and H. A. Zebker, "Modeling and observation of the radar polarization signature of forests areas", *IEEE Trans. on Geosci. and Remote*

Sensing, vol. 27, no. 3, pp. 290-301, 1989.

- [4] F. T. Ulaby, K. Sarabandi, K. C. McDonald, M. Whitt, and M. C. Dobson, "Michigan Microwave Canopy Scattering Model (MIMICS)", *Int. J. of Remote Sensing*, vol. 11, no. 7, pp. 1223-1253, 1990.
- [5] G. Sun, D. S. Simonett, and A. H. Strahler, "A radar backscattering model for discontinuous coniferous forests", *IEEE Trans. on Geosci. and Remote Sensing*, vol. 29, no. 4, pp. 639-650, 1991.
- [6] Y. Wang, G. Sun, and John Day, "Santa Barbara microwave backscattering model for woodlands", submitted to *Int. J. Remote Sensing* for publication, pp. 27, 1991.
- [7] Y. Wang, J. L. Day, F. W. Davis, and J. M. Melack, "Modeling L-band radar backscatter of Alaskan boreal forest", submitted to *IEEE Trans. on Geosci. and Remote Sensing*, for publication, pp. 19.
- [8] Y. Wang, "Radar backscatter canopy modeling and applications", A Ph. D. Dissertation, The University of California at Santa Barbara, pp. 100, 1992.

Figure 1. Model results vs SAR data at P-band



Solid lines indicate the equality of modeled means to those of SAR data. Dotted lines show ± 1.0 dB calibration uncertainty for the HH, HV, and VV backscatter (Figure 1a-c) and ± 0.1 for the HH and VV correlation coefficient (Figure 1d). "+", "*", and "x" represent data points of stands "Sp2", "St2", and "St11", respectively.

SAR BACKSCATTER FROM CONIFEROUS FOREST GAPS

John L. Day and Frank W. Davis

Department of Geography, University of California, Santa Barbara, CA 93106

Introduction

A study is in progress comparing AIRSAR backscatter from coniferous forest plots containing gaps to backscatter from adjacent gap-free plots. We are asking "How do gaps in the range of 400 to 1600 m^2 (approximately 4-14 pixels at intermediate incidence angles) affect forest backscatter statistics?" and "What incidence angles, wavelengths, and polarizations are most sensitive to forest gaps?" In order to visualize the slant-range imaging of forest and gaps we make use of a simple conceptual model. This strictly qualitative model has led us to hypothesize that forest radar returns at short wavelengths (eg., C-band) and large incidence angles (eg., 50°) should be most affected by the presence of gaps, whereas returns at long wavelengths and small angles should be least affected. Preliminary analysis of 1989 AIRSAR data from forest near Mt. Shasta supports the hypothesis.

Current forest backscatter models such as MIMICS (Ulaby *et al.* 1990) and Santa Barbara Discontinuous Canopy Backscatter Model (Sun *et al.* 1991) have in several cases correctly predicted backscatter from forest stands based on inputs of measured or estimated forest parameters (McDonald *et al.* 1990, Wang and Paris 1992). These models do not, however, predict within-stand SAR scene texture, or "intrinsic scene variability" as Ulaby *et al.* (1986) has referred to it. For instance, the Santa Barbara model, which may be the most spatially coupled of the existing models, is not truly spatial. Tree locations within a simulated pixel are distributed according to a Poisson process, as they are in many natural forests, but tree size is unrelated to location, which is not the case in nature. Furthermore, since pixels of a simulated stand are generated independently in the Santa Barbara model, spatial processes larger than one pixel are not modeled. Using a different approach, Oliver (1991) modeled scene texture based on an hypothetical forest geometry. His simulated scenes do not agree well with SAR data, perhaps due to the simple geometric model used.

Insofar as texture is the expression of biological forest processes, such as succession and disease, and physical ones, such as fire and wind-throw, it contains useful information about the forest, and has value in image interpretation and classification. Forest gaps are undoubtedly important contributors to scene variance. By studying the localized effects of gaps on forest backscatter, guided by our qualitative model, we hope to understand more clearly the manner in which spatial heterogeneities in forests produce variations in backscatter, which collectively give rise to scene texture.

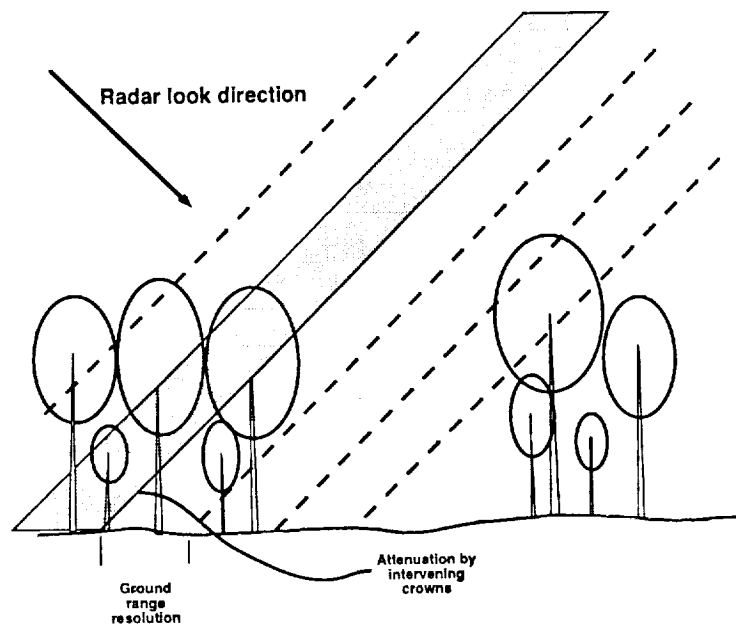
Shasta Forest Gaps: a Conceptual Model

The forest at the Mt. Shasta study site spans a range of tree sizes and stand densities, but for the purpose of a conceptual model, we assume crowns are interlocked and tree heights are 20-25 m. Forest gaps ranging from 400 to 1600 m^2 are assumed circular. Slant range pixel spacing is 6.7 m.

The imaging geometry is illustrated in Figure 1 for $\theta_o = 45^\circ$. One slant range-pixel is shown shaded. If canopy penetration is deep, as at P-band, the entire pixel

volume can contribute to backscatter. In this case, *effective range resolution* becomes a function not only of θ_o and slant-range resolution, but also of tree height, canopy depth, and extinction coefficient. *Effective range resolution* for long wavelengths and small incidence angles could be much coarser than ground range resolution. Conversely, at large incidence angles the pixel is oriented more vertically, which reduces the pixel volume intersecting the canopy. At short wavelengths, canopy extinction limits backscatter to the upper canopy, further reducing pixel volume. It follows that short wavelengths combined with large incidence angles should lead to the maximum *effective range resolution* of laterally oriented forest features (such as gaps), and to the greatest effects on local backscatter.

Figure 1



Methodology and Preliminary Results

To test this hypothesis, 238 forest gaps were located on orthophotoquads of the region. Gap coordinates in three SAR images ($\theta_o \approx 23^\circ$, 40° , and 50°) were determined by co-registering a digitized map of the forest gaps to the SAR images. We are currently comparing backscatter from plots containing gaps in several size classes to adjacent areas without gaps. The mean and median of the backscatter distributions from 5x7 pixel windows have proven insensitive to the presence of gaps in the 500-900 m^2 size range. A more effective test statistic is the difference in backscatter at the lower quartiles of the gap and non-gap backscatter distributions. Tests on a subset of the data ($n=12$ pairs) indicate that the lower quartile backscatter at C-band, HH polarization, for $\theta_o \approx 50^\circ$ is significantly lower (at the 95% confidence level) for gap-containing plots than for gap-free plots (Table 1). Lower quartile differences for other bands and angles are not significant. Following analysis of the full data set, we plan to test other parameters, such as the difference in the coefficient of variation of gap and non-gap windows, so as to build a clearer empirical understanding of the effects of forest spatial heterogeneities on backscatter.

Table 1. Difference between backscatter from gap-containing and gap-free forest plots

	C-band			L-band			P-band		
	HH	HV	VV	HH	HV	VV	HH	HV	VV
25°	0.56	0.65	0.41	-0.34	-0.01	0.22	0.27	0.06	-0.22
40°	-0.39	-0.09	-0.38	-0.18	-0.31	-0.08	-0.45	-0.01	-0.76
50°	*-1.42	-0.85	-0.40	-0.02	-0.66	-0.52	-0.36	0.29	-0.86

Values shown are the mean differences in backscatter (dB) between the lower quartiles of gap-containing plots and the lower quartiles of gap-free plots. * indicates significance at the 95% confidence level for the 12 pairs of plots tested.

Acknowledgements

This research is funded by CalSpace under award #cs-86-90, and by the NASA SIR-C/X-SAR project through JPL under contract # 958468

References

- McDonald, K. C., M. C. Dobson, and F.T. Ulaby, 1990,
Using MIMICS to model L-band multiangle and multitemporal backscatter from a walnut orchard. *IEEE Transactions on Geoscience and Remote Sensing*, vol. GE-28, no. 4, pp. 477-491
- Oliver, C. J., 1991,
Natural clutter in coherent imaging, *International Journal of Remote Sensing*, vol. 12, no. 2, pp. 329-338,
- Sun, G., D. S. Simonett, and A. H. Strahler, 1991,
A radar backscattering model for discontinuous coniferous forests, *IEEE Transactions on Geoscience and Remote Sensing*, vol. 29, no. 4, pp. 639-650.
- Ulaby, F. T., F. Kouyate, B. Brisco, and T. H. Lee Williams, 1986, Textural information in SAR images, *IEEE Transactions on Geoscience and Remote Sensing*, vol. GE-24, no. 2, pp. 235-245,
- Ulaby, F. T., K. Sarabandi, K. C. McDonald, M. Whitt, and M. C. Dobson, 1990a,
Michigan Microwave Canopy Scattering Model (MIMICS), *International Journal of Remote Sensing*, vol. 11, no. 7, pp. 1223-1253.
- Wang, Y., and J. F. Paris, 1992,
Inclusion of a simple multiple scattering model into the Santa Barbara microwave backscatter canopy model for woodland, submitted to *IEEE Transactions on Geoscience and Remote Sensing*

A. Beaudoin, T. Le Toan and F. Zagolski

CESR, 9 Ave Colonel Roche, 31400 Toulouse, France / Tel: 61.55.66.71

C.C. Hsu, H.C. Han and J.A. Kong

MIT, Cambridge MA02139, USA / Tel: (613)253-5625

1. INTRODUCTION

The analysis of JPL AIRSAR data over the Landes forest in South-West France revealed strong correlation between L- and especially P-band σ^0 and the pine forest biomass (*Le Toan et al. 1992*). To explain the physical link of radar backscatter to biomass, a polarimetric backscattering model was developed and validated (*Hsu et al. 1992*). Then the model was used in a simulation study to predict σ^0 sensitivity to undesired canopy and environmental parameters (*Beaudoin et al. 1992*). This paper reports main results concerning the data analysis, modeling and simulation at P-band.

2. EXPERIMENT AND DATA ANALYSIS

The test site is a managed forest of maritime pine (*Pinus Pinaster*), including clear-cuts and forest stands from seedlings up to 46 years old, providing a wide range of forest parameters (height, dbh, tree density, etc.). The collected parameters concern forest inventory, measurements during radar overflight and tree structure sampling. P-L-C band quad-pol AIRSAR data were acquired on August 16, 1989. A complete polarimetric calibration procedure was applied to the data.

Of particular interest for applications are the above-ground biomass by parts (needle, branch and trunk biomass), which can be estimated using tree basal area and tree density. Fig. 1 shows biomass by parts which is increasing quasi linearly with age. High correlation was found between L- and especially P-band σ^0 and most forest parameters, especially biomass (tons/ha), for example total above-ground biomass as shown in Fig. 2. As σ^0 was found statistically correlated to many forest parameters (age, height, dbh, biomass), which are themselves biologically interrelated, theoretical modeling is needed to explain the interaction between incident wave and different parts of forest canopies.

3. MODELING

A radiative transfer model is used for the modeling of the pine forest backscatter (*Hsu et al. 1992*), which includes a branching model for vegetation clusters found in pine forests. The forest is modelled as a 4-layer discrete random medium over a slightly rough ground (crown, trunk, bush and grass layers). Vegetation constituents are modelled as clusters of dielectric cylinders accounting for needles, twigs, branches and trunks. Both incoherent and coherent scattering from these multiscale clusters are

computed. The model gives the expression of the 1st-order solution to the RT equations as the sum of volume and surface-volume scattering terms in each layer. For hilly terrains, the model considers the ground slope and aspect angles. Fig.2 shows model/measurement comparison of P-band σ^0 at HH, HV and VV polarizations at $\theta=45^\circ$, as a function of the total above-ground biomass, while Fig. 3 presents the main scattering contributions at HH and VV. The HH return is mainly governed by crown and crown-ground scattering for young forest, and trunk-ground scattering for mature forest. The VV and HV returns are dominated by crown scattering, which comes from the primary branches. Thus, VV and especially HV σ^0 are directly linked to radius, length, density and moisture content of primary branches. Hence σ^0 increases with increasing branch fresh biomass. Relations between σ^0 and forest height, trunk or total biomass are therefore indirect. The above results provide a significant improvement of our knowledge on the scattering mechanisms and consequently our understanding of the relationships σ^0 - forest biomass.

4. CHANGING FOREST AND ENVIRONMENTAL PARAMETERS

To extend the above observations to various forest and environmental conditions, a simulation study is performed.

1) Ground slope effects: Fig.4 presents σ^0 as a function of local ground slope facing the radar. VV and HV are not changed significantly, whereas HH is fastly decreasing for old forests where the trunk-ground term dominates, and is approaching to the crown scattering term.

2) Varying understory conditions: σ^0 is computed for a canopy without and with an understory vegetation (1m high, LAI=1.0). As expected, HV and VV returns are not affected, whereas a 1dB decrease of σ^0 for HH is due to the attenuation of the trunk-ground term.

3) Vegetation moisture condition was varied from 55% to 65% to simulate seasonal or diurnal effects. HH is not significantly sensitive to this variation, whereas VV and HV returns are more affected (about 1dB).

3) Crown structure: σ^0 was simulated as a function of β , the mean elevation angle of the primary branches, which is a major species-dependent structural parameter. At HV and VV, the maximum sensitivity to crown biomass is found in the range 45° - 60° . For low or high β (erectophile or planophile species), there is no significant sensitivity to crown biomass. For HH returns, no effect of β on the σ^0 sensitivity to biomass is observed, as the return results mainly from trunk-ground interaction.

5. DISCUSSION & CONCLUDING REMARKS

At present, the modeling and simulation studies were performed at P-band, which was found optimal for retrieval of forest biomass. HH return was found governed by trunk-ground scattering, and thus can be significantly affected by environmental conditions such as soil moisture, ground slope and bush layer. On the other hand, VV and especially HV returns were found tightly linked to crown biomass and thus unaffected directly by environmental conditions. Therefore, it is possible to derive total above-ground biomass from P-band HV or VV SAR data, knowing relations between biomass by parts. HH return offers the advantage of being less species dependent.

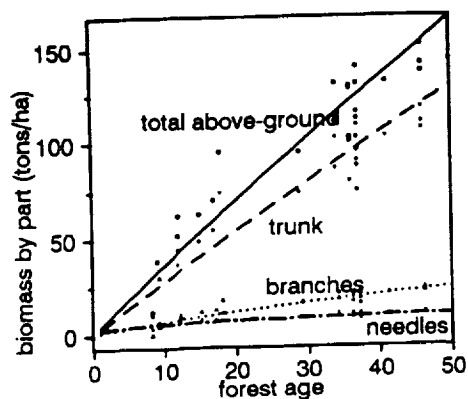


Fig. 1: biomass by parts as a function of age

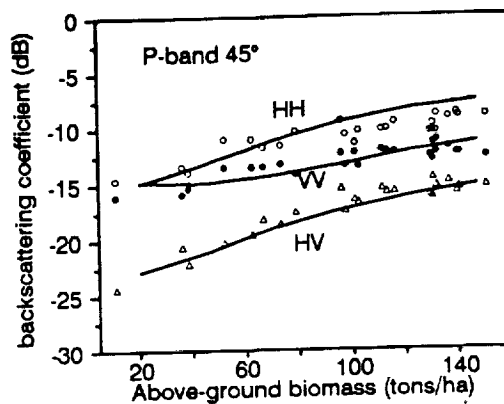


Fig. 2: Model/measurements comparison

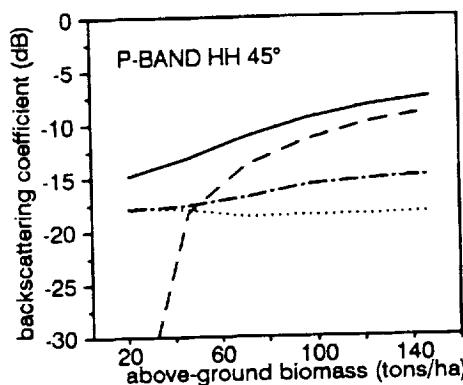


Fig. 3: Major contributions to total HH and VV P-band backscatter, as a function of total above-ground biomass

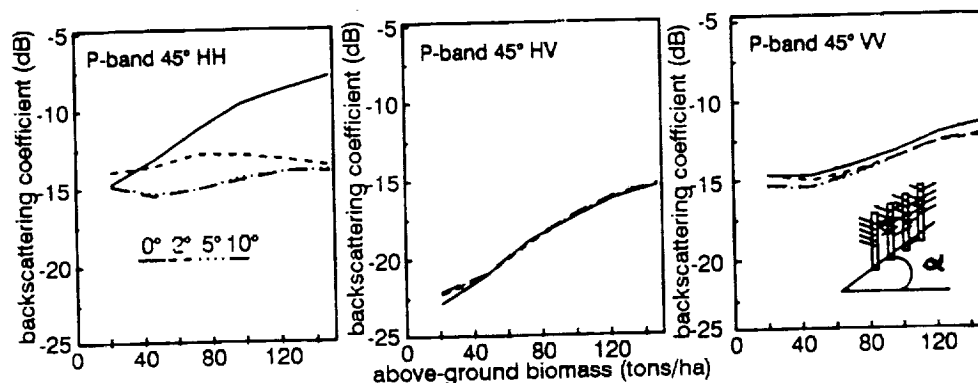
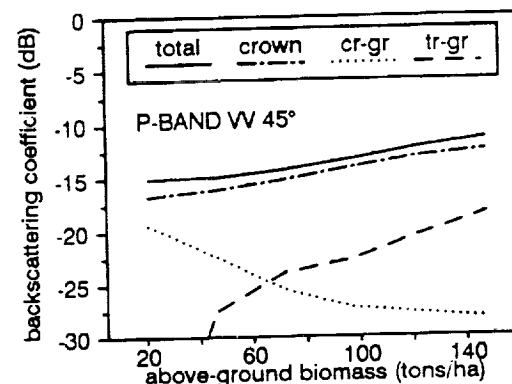


Fig. 4: P-band backscatter at HH, HV and VV as a function of biomass, for different ground slope angles

REFERENCES

- [1] T. Le Toan, A. Beaudoin, J. Riou and D. Guyon (1992), "Relating forest biomass to SAR data", IEEE Trans. on Geo. and Rem. Sens., Vol.30, No 2, March 1992.
- [2] C.C. Hsu, H.C. Han, R.T. Shin and J.A. Kong, T. Le Toan and A. Beaudoin, "Radiative Transfer theory for polarimetric remote sensing of pine forest", IGARSS'92 Proceedings, Houston, USA, May 1992.
- [3] A. Beaudoin, T. Le Toan, C.C. Hsu, H.C. Han, J.A. Kong and R.T. Shin, "Simulation of forest backscatter as a function of forest and ground parameters", IGARSS'92 Proceedings, Houston, USA, May 1992.

CHARACTERIZATION OF WETLAND, FOREST, AND
AGRICULTURAL ECOSYSTEMS IN BELIZE WITH AIRBORNE
RADAR (AIRSAR)

Kevin O. Pope
Jose Maria Rey-Benayas

Geo Eco Arc Research
2222 Foothill Blvd., Suite E-272, La Canada,
California 91011

Jack F. Paris

Department of Biology
California State University, Fresno
Fresno, California 93740

1. Introduction

The Shuttle Imaging Radar-C/X-SAR Experiment includes the study of wetland dynamics in the seasonal tropics. In preparation for these wetland studies, we analyzed airborne P, L, and C band radar (AIRSAR) data of Belize, Guatemala, and Mexico acquired by NASA and JPL in March 1990. The first phase of our study focuses on AIRSAR data from the Gallon Jug test site in northwestern Belize, for which ground data were also collected during the three days prior to the overflight. One of the main objectives of the Gallon Jug study is to develop a method for characterizing wetland vegetation types and their flooding status with multifrequency polarimetric radar data.

2. Methods of AIRSAR Analysis

We converted the four look AIRSAR data acquired from JPL in the compressed Stokes matrix format into five re-scaled 8-bit rasters for each frequency (Table 1). The image was rectified to ground range. The HH and VV rasters were corrected for scene and sensor effects caused by changes in look angle across track. This was accomplished by compiling backscatter means for three sets of 7 sample polygons of homogeneous upland forest distributed across track, and then performing a regression analysis to determine the angular dependency of HH and VV. The regression equation was then applied to correct the image for variable look angles. Next, we filtered each raster with two iterations of a 3 x 3 modal filter to reduce

the effects of speckle. Since we were primarily interested in characterizing vegetation types, we transformed the AIRSAR parameters from each band into four indices that reflect aspects of the vegetation (Table 1). These indices (except for the biomass index) have the added benefit of being mostly independent of terrain slope, thus allowing for better measures of vegetation characteristics. The canopy structure index provides a measure of the dominance of vertical structures such as stems or trunks. The volume scattering index provides a measure of volume scattering, which can be related to canopy thickness. The biomass index reflects the relative amount of woody compared to leafy biomass in forests and therefore has higher values for deciduous than for evergreen forests due to absorption by green leaves, especially in L and P band. The biomass index for herbaceous types more closely reflects total above ground biomass. The interaction type or phase angle difference index measures the importance of single bounce or volume scattering relative to double bounce interactions. The possible 360 degrees of phase shift have been scaled in a monotonic fashion so that interactions containing appreciable amounts of double bounce have lower values. It is important to note that these indices must be interpreted with caution, especially in comparisons between ecosystem types with very different structure.

The final step was a clustering analysis. Clustering was first run on a pixel by pixel basis for the four indices from P, L, and C band using the Isoclass algorithm with 45 classes. A second clustering of the 45 classes, based on class means, was performed using the centroid method in the SAS statistical package.

3. Results

The cluster analysis identified 12 distinct land cover types in the Gallon Jug test site that were verified with field data: 1) pasture and cultivated lands, 2) water, 3-4) two types of marsh, 5) recently cut forest, 6) regrowth, 7) flooded swamp forest, 8) non-flooded swamp forest, 9) flooded swamp thicket, and 10-12) three types of upland forest. Examination of the indices for each of the 12 types helps clarify differences. The two marsh types represent low (C band BM=29) and high (C band BM=92) biomass marshes. The swamp forests have a high percentage of woody compared to leafy biomass (P band BM=63-72), especially when swamp forests are compared with upland forests (see

below). Swamp forest flooding is indicated by the lower PD (P band PD=43) as compared with the non-flooded swamp forest (P band PD=62). The swamp thicket has less woody biomass (P band BM=33) than the swamp forests, and again flooding is indicated by the low PD (P band PD=45). The three forest types represent a gradient from semi-deciduous to semi-evergreen as indicated by decreasing woody biomass (P band BM = 46, 40, 27). This decrease in BM is mirrored by an increase in P and L band volume scattering (e.g. P band VS = 49, 50, 52), which may reflect an increase in canopy closure or thickness. The BM index for the agricultural ecosystems shows an increase from pasture/cultivation (e.g. P band BM=6) to regrowth (e.g. P band BM=14), although some of the dense forest regrowth was classified as forest. The recently cut forest has felled trees with no leaves, which give a very high woody biomass value (P band BM=85), a low volume scattering value (P band VS=40), and a low canopy structure index (P band CAN=40).

Table 1. AIRSAR parameters and indices used in analysis (compiled for P, L, and C band).

Initial parameters derived from Stokes matrix*

Backscatter amplitude parameters

$$\begin{array}{ccccc} \text{HH} & \text{VV} & \text{CS} = \frac{\text{HV} + \text{VH}}{2} & \text{LK} = \frac{\text{VV} + \text{HH}}{2} \end{array}$$

Backscatter phase angle parameter

$$\text{HH, VV phase angle difference} = \text{PD}$$

AIRSAR indices

$$\begin{array}{llll} \text{Canopy structure} = \text{CAN} & = & \frac{\text{VV}}{\text{VV} + \text{HH}} \\ \text{Volume scattering} = \text{VS} & = & \frac{\text{CS}}{\text{CS} + \text{LK}} \\ \text{Biomass} = \text{BM} & = & \text{LK} \end{array}$$

$$\begin{array}{llll} \text{Interaction type} = \text{PD} & = & \text{PD converted to} \\ \text{(HH, VV phase angle diff.)} & & \text{monotonic scale} \end{array}$$

*Derivation of these parameters is described in detail in J. F. Paris, Processing Airborne Imaging Radar (AIR) Data on a Microcomputer Workstation. Technical Report TR-89-04, Department of Geography, California State University, Fresno, 1989.

STRATEGIES FOR DETECTION OF FLOODPLAIN INUNDATION WITH MULTI-FREQUENCY POLARIMETRIC SAR

Laura L. Hess* and John M. Melack**

*Dept. of Geography and **Dept. of Biological Sciences
University of California, Santa Barbara, CA 93106

Introduction

Mapping of floodplain inundation patterns is a key element in developing hydrological and biogeochemical models for large tropical river basins such as the Amazon. Knowledge of the time sequence of inundation is necessary to determine both water routing and biogenic gas fluxes (Richey et al. 1990). SAR is uniquely suited for this application because of its ability to penetrate cloud cover and, in many cases, to detect flooding beneath a forest or herbaceous canopy (Hess et al. 1990). We are currently developing a procedure for discriminating flooded forest, flooded herbaceous vegetation, and open water from other cover types for a coastal wetland site on the lower Altamaha floodplain, Georgia, emphasizing robust classifiers that are not site-specific.

Study site and methods

Multiple datatakes over a range of incidence angles were obtained for the Altamaha site by the JPL polarimetric SAR in March 1990 and again in May 1991. For both dates, the Altamaha was at high flood stage, and the entire floodplain other than sand ridges was inundated. Water levels were documented by extensive ground observations during the overflight. A rich variety of wetland types occur in the study site, including cypress-tupelo swamp (*Taxodium distichum*, *Nyssa aquatica*), bottomland hardwood forest (*Nyssa* spp., *Taxodium distichum*, *Fraxinus* spp., *Acer rubrum*, *Liquidambar styraciflua*), and marshes dominated by *Spartina alterniflora*, *Juncus roemerianus*, and *Zizaniopsis miliacea*. Upland sites are predominantly loblolly pine (*Pinus taeda*) plantations. Results given in this summary are for a March 1990 scene calibrated with JPL's SUPERCAL software using corner reflectors. The radar variables used in the analysis are HH, VV, and HV radar cross-sections per unit area (σ^0) and HH-VV phase difference for C, L, and P-bands, and ratios directly derived from these parameters. A 5X5 median filter was applied to the radar cross-sections to reduce within-class variability. Initial analysis was performed on 100 pixels in each of five cover types: open water, clearing, marsh, pine, and flooded forest. For each category, five 20-pixel windows were selected, representing a range of incidence angles and vegetation variability within each category. Because nearly all hardwood forests in the scene were flooded at the time of the overflight, pine forests are used to represent unflooded forests.

Discrimination of cover types

Discussion in this summary will be limited to two of the radar parameters found to be the most useful: PHH to CHH ratio and L-band phase difference. In Figure 1, σ_{PHH}^0 is plotted vs. σ_{CHH}^0 for unfiltered and median-filtered data; each plotted character represents a pixel. Separation between the classes is good, though not absolute, for the filtered data; overlap in the unfiltered data makes discrimination impossible. For the filtered data, mean σ^0 values for flooded forest and pine respectively are -8.2 dB and -12.8 dB at CHH and -1.1 dB and -4.6 dB at PHH. Although the means are distinct at both bands, there is enough spread in the data to cause confusion between the pine and

flooded forest categories.

Figure 2 demonstrates the behavior of phase difference at L band and C band for flooded forest. These phase difference histograms are presented on a circular scale rather than the usual linear one. There is a distinct shift toward phase differences close to 180° for flooded forests at L band, indicative of double-bounce scattering; this is not the case for pines. However, the phase difference distribution is too broad to perform well as a classifier, and phase difference, because of its circular nature, does not lend itself to techniques such as median filtering. We have found that by classifying the phase difference into one of three types and then applying a modal filter, confusion between pines and flooded forests is largely eliminated. Phase differences from 0° - 70° or 270° - 360° are classed as type 1, those centered on 180° (110° - 250°) are considered type 3, and intermediate phase differences (70° - 110° or 250° - 290°) are type 2. A 3X3 pixel modal filter is then applied to the data, creating regions of uniform phase difference type. Although this technique is conceptually very simple, results to date show excellent separation between flooded forest and other categories. Table 1 shows the number of pixels classified in each type for 1000 pixels each from the marsh, pine, and flooded forest categories. Ninety-nine percent of the flooded forest pixels were classed as type 3. Only 1 non-flooded-forest pixel was type 3, and six flooded forest pixels were type 2.

Table 1. LHH-LVV phase difference types for 1000-pixel samples of marsh, pine, and flooded forest			
	Type 1	Type 2	Type 3
Marsh	520	479	1
Pine	970	30	0
Flooded forest	0	6	994

The scatter plot for filtered σ_{PHH}^0 vs. σ_{CHH}^0 suggests that, following widely used parametric classification procedures, combinations of parameters could be found to provide a highly accurate separation between the cover types. The classification procedure would be tailored to the radar signatures (means and covariance matrices) for that particular scene. The limitation of this approach is that good results usually would not be obtained when applying the signatures to other scenes. Even for the same scene, signatures will vary temporally due to seasonal changes in scene properties such as leaf area index. Because we plan to apply this procedure to a broad spatial and temporal domain, scene-by-scene optimization of parametric classifiers is impractical. A knowledge-based approach using convergent evidence (Wharton 1989) seems best suited to this task.

Acknowledgements

This work is funded by the NASA SIR-C/XSAR program, JPL contract #958469.

References

- Hess, L.L., J.M. Melack, and D.S. Simonett, 1990, Radar detection of flooding beneath the forest canopy: a review. *Int. J. of Remote Sensing* 11(7): 1313-1325.
- Richey, J.E., J.B. Adams, and R.L. Victoria, 1990, Synoptic-scale hydrological and biogeochemical cycles in the Amazon River basin: a modeling and remote sensing perspective. In R.J. Hobbs & H.A. Mooney, eds., *Remote sensing of biosphere functioning*. New York: Springer-Verlag.
- Wharton, S.W., 1989, Knowledge-based spectral classification of remotely sensed image data. In G. Asrar, ed., *Theory and applications of optical remote sensing*. New York: John Wiley & Sons.

Fig. 1a. Unfiltered data, Clearing (C), Marsh (M), Pine (P), Flooded Forest (F)

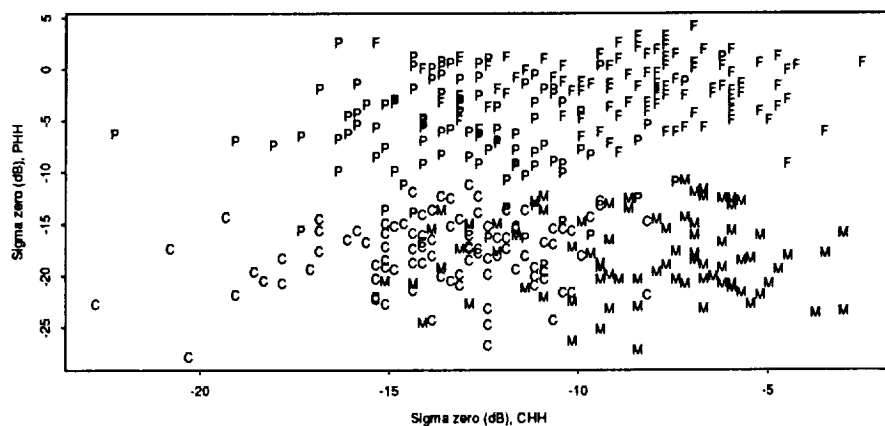


Fig. 1b. Filtered data, Clearing (C), Marsh (M), Pine (P), Flooded Forest (F)

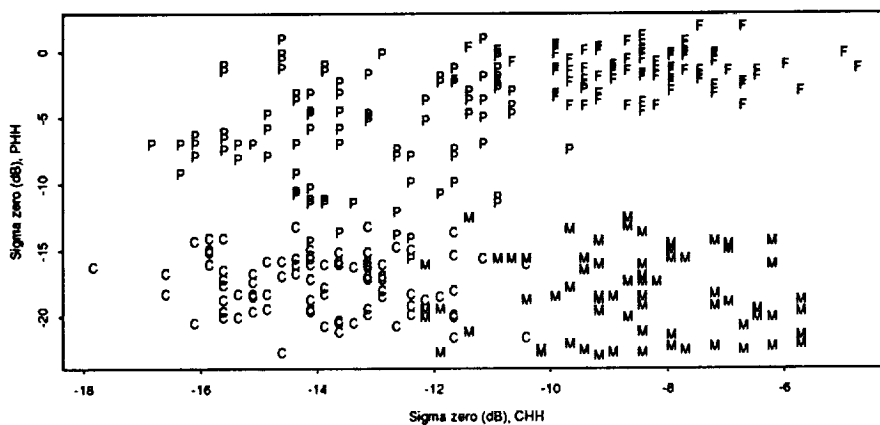


Fig. 2a. HH-VV phase difference

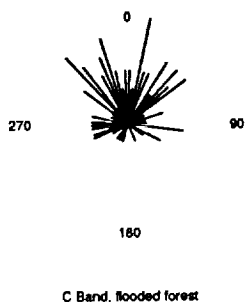
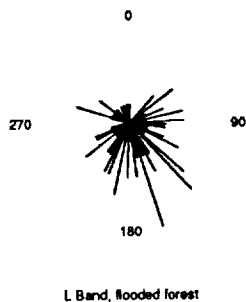


Fig. 2b. HH-VV phase difference



SUPERVISED FULLY POLARIMETRIC CLASSIFICATION OF THE BLACK FOREST TEST SITE: FROM MAESTRO1 TO MAC EUROPE

G. De Grandi, C. Lavallo, H. De Groof, A. Sieber

*Commission of European Communities
Joint Research Center
Institute for Remote Sensing Applications
21020 - Ispra (VA) Italy*

1. INTRODUCTION

We present a study on the performance of a supervised fully polarimetric maximum likelihood classifier for SAR data when applied to a specific classification context: forest classification based on age classes and in the presence of a sloping terrain.

For the experimental part of the study we use the polarimetric AIRSAR data at P, L, and C band, acquired over the German Black Forest near Freiburg in the frame of the 1989 MAESTRO-1 campaign and the 1991 MAC Europe campaign. MAESTRO-1 was an ESA/JRC sponsored campaign, and MAC Europe (Multi-sensor Aircraft Campaign) was organized by NASA; in both cases the multi-frequency polarimetric JPL-AIRSAR radar was flown over a number of European test sites.

The study is structured as follows. At first we investigate the general characteristics of the classifier and the dependencies from some parameters, like frequency bands, feature vector, calibration, using test areas lying on a flat terrain. Once we have determined the optimal conditions for the classifier performance, we then move on to the study of the slope effect. The bulk of this work is performed using the Maestro1 data set.

Next we consider the classifier performance with the MAC Europe data. The study here is divided into two stages: first we repeat some of the tests done on the Maestro data, to highlight the improvements due to the new processing scheme that delivers 16 look data. Second we experiment with multi images classification with two goals: to assess the possibility of using a training set measured from one image to classify areas in different images; to classify areas on critical slopes using different viewing angles.

In this summary paper we will list the main points of the study and highlight only some of the results obtained so far.

2. CLASSIFIER PRINCIPLES

The principles of the fully polarimetric maximum likelihood classifier are described in [Kong et al. 1987]. Suffice here only to say that the discriminant function, in the form of a minimum distance, is given by:

$$d_m(\mathbf{x}) = \mathbf{x}^* \cdot \mathbf{C}_m^{-1} \cdot \mathbf{x} + \ln |\mathbf{C}_m|, \quad (1)$$

where $\mathbf{x} = [HH \ HV \ VV]^T$ is the complex feature vector for the unknown pixel and \mathbf{C}_m is the spatially averaged covariance matrix of the training class.

3. GENERAL CLASSIFIER CHARACTERIZATION

3.1 Methodology

For the study of the classifier performance, we define training and test sets using the ground data collected during the Maestro1 campaign [Churchill 1989]; the forest is

segmented into stands characterized by the mean tree age. The tree ages have been grouped into four main classes: young trees (10–30 years), mature trees (30–70 years), adult trees (70–110), old trees (> 110 years). The training and test areas are taken on a flat terrain, to filter out from this analysis the influence of slope.

At this level of the study we then investigate the following points (see also [De Grandi et al. 1992]):

- characterization of the training sets through their covariance matrices
- classification performance as a function of the frequency bands
- dependency from the off diagonal terms of the covariance matrix
- dependency from polarimetric calibration
- relative weight of the feature vector elements in the discriminant function
- performance in the case of a one channel and a two channels feature vector

3.2 Results and discussion

As an example we report in table I the results of the classification of 3 forest age classes, an urban area and an arable field at P, L and C bands.

Table I – Confusion Matrix for 3 Forest Age Classes, an Arable Field and an Urban Area; Maestro1 Freiburg Data Set at P-, L- and C Bands

	P band					L band					C band				
	urban	arable	age1	age2	age4	urban	arable	age1	age2	age4	urban	arable	age1	age2	age4
urban	27.8	0.0	15.7	10.1	28.4	16.3	0.0	15.4	19.9	11.4	0.0	4.6	9.5	9.2	2.6
arable	0.0	100.	0.0	0.0	0.0	0.0	75.7	0.0	0.0	0.0	0.0	87.0	1.9	1.9	9.3
age1	0.0	0.0	92.7	4.9	2.4	0.0	0.0	75.6	17.1	7.3	0.0	14.6	34.2	22.0	29.3
age2	0.8	0.0	16.5	63.9	18.8	0.0	0.0	36.1	51.9	12.0	0.0	5.3	21.1	42.9	30.1
age4	3.1	0.0	4.0	30.9	61.8	0.0	0.0	49.7	28.3	21.9	0.0	7.5	19.7	26.1	46.8

Given the classification parameters of our test case, P band appears to be the most suitable for forest discrimination.

4. SLOPE EFFECT

4.1 Methodology

The Maestro1 Freiburg data set has been georeferenced [De Groof et al. 1991] and it is, therefore, possible to attach to each pixel in the image space the corresponding coordinates in the map space, and additional layers of information, such as the local incidence angle, and the slope. This processing step has then allowed us to divide each polygon representing an age class into sets of pixels having a given slope angle. In particular we defined 6 slope classes with angular spacing of 5 degrees. This spacing was chosen from considerations on the variance of the powers of the 3 polarimetric channels.

4.2 Discussion

The test set for 3 age classes exhibits high between groups variance when the 6 slope classes are considered and the confusion in the classification is therefore relevant. A

possible correction to the slope influence could be to drive the classifier with the knowledge of the slope angle for each pixel; in other words, the classifier could be switched among a number of different training sets, according to the slope angle of the pixel to be classified. Unfortunately this method works only for certain slope classes; indeed for positive slope angles greater than 10 degrees, the class separation is also affected, and therefore the classification accuracy is degraded even if a proper training set is taken into account. This can be seen for instance calculating the distance between 2 age classes and the 6 slope classes.

5. MAC EUROPE DATA

5.1 Methodology

The MAC Europe data have been processed with a new correlator and one of the available products is a 16 look data set. Moreover for the Freiburg test site we have at disposal a number of flights paths, both in the same direction and at orthogonal directions. This paves the way to an interesting experiment in multi image classification. First and essential step for this purpose is an accurate radiometric and polarimetric calibration of the data sets, and their co registration. By the time of writing of this summary this processing step is under way.

The plans are to explore the possibility of classifying multiple scenes using a training set measured on one scene, and to exploit the different viewing angles to resolve the confusion in forest age classification introduced by the terrain slope.

5.2 Preliminary results

Classification based on the same training set used in the test case with the Maestro data reported in section 3.2 has been performed on the Mac Europe data set with scene identifier cm3207. The results are reported in table II. The classification accuracy is significantly improved at P band with respect to the Maestro1 case.

**Table II – Confusion Matrix for 3 Forest Age Classes and an Arable Field;
MAC Europe Freiburg Data Set at P-, L- and C Bands**

	P band				L band				C band			
	arable	age1	age2	age4	arable	age1	age2	age4	arable	age1	age2	age4
arable	96.69	1.24	0.00	0.00	93.80	2.89	0.00	0.41	92.15	3.72	0.41	2.07
age1	0.00	92.86	3.57	3.57	7.14	64.29	25.00	3.57	21.43	57.14	17.86	3.57
age2	0.00	9.90	86.46	3.65	0.00	38.02	54.69	7.29	25.52	7.81	42.19	24.48
age4	0.00	1.06	8.46	90.48	0.00	56.34	28.85	14.80	34.74	14.50	13.29	37.46

6. REFERENCES

- J. A. Kong, A. A. Swartz, H. A. Yuch, "Identification of Terrain Cover Using the Optimum Polarimetric Classifier", *J. Electromagn. Waves Appl.*, vol. 2. pp. 171-194, 87
- P.N. Churchill, "Procedures for the Collection and Compilation of Forest Ground Data in Microwave Experiments", *JRC Ispra Tech Note July 1989*.
- G. De Grandi, G. Lemoine, A. Sieber, "Supervised Fully Polarimetric Classification: An Experimental Study on the Maestro1 Freiburg Data Set", *Proc. IGARSS '92, Houston May 1992*.
- H. De Groof, G. De Grandi, A.J. Sieber, "Geometric Rectification and Geocoding of JPL AIRSAR Data Over Hilly Terrain", *Proc. Third AIRSAR Workshop, Pasadena May 23-24, 1991*.

RELATING MULTIFREQUENCY RADAR BACKSCATTERING TO FOREST BIOMASS: MODELING AND AIRSAR MEASUREMENT

Guoqing Sun¹ and K. Jon Ranson²

¹ Ressler Associates, Inc. 14440 Cherry Lane, Suite 212, Laurel, MD, 20707, USA.

² Biospheric Sciences Branch, GSFC Greenbelt, MD 20771, USA.

1. INTRODUCTION

During the last several years, significant efforts in microwave remote sensing have been devoted to relating forest parameters to radar backscattering coefficients (e.g., Le Toan et al., 1991; Kasischke, et al., 1991). These and other studies showed that in most cases, the longer wavelength (i.e. P band) and cross-polarization (HV) backscattering had higher sensitivity and better correlation to forest biomass.

This research examines this relationship in a northern forest area through both backscatter modeling and SAR data analysis. The field measurements (Ranson and Smith, 1990) were used to estimate stand biomass from forest weight tables. The backscatter model described by Sun et al. (1991) was modified to simulate the backscattering coefficients with respect to stand biomass. The average number of trees per square meter or radar resolution cell, and the average tree height or diameter breast height (dbh) in the forest stand are the driving parameters of the model. The rest of parameters such as the dielectric constants of tree components and soils, roughness of the soil surface, orientation and size distributions of leaves and branches, remain unchanged in the simulations.

2. MODEL DESCRIPTION

2.1. Tree crown scattering

Tree crowns were modeled as ellipsoids consisting of a mixture of leaves and branches (scattering elements) with various sizes and orientations. The scattering can be characterized by the complex scattering matrix S . The Stokes matrix L derived from the complex scattering matrix S was averaged over all orientations and sizes of the scattering elements.

The extinction coefficient matrix κ is expressed in terms of the forward scattering amplitude, and was averaged over orientation and size distributions of scatterers in the same way as the Stokes matrix. Having multiplied by the number of scatterers per cubic meter in the tree crown, the Stokes and Extinction matrices then can be used in the radiative transfer equation to calculate the backscattering and attenuation from a tree crown layer.

Table 1 and 2 show some calculated results using input data from a hemlock forest stand (Chauhan et al., 1991). The first element of Stokes matrix ($L(1,1) = S_{vv}S_{vv}^*$) was used to compare the backscattering strength between leaves and branches, and between branches with various sizes. The first element of extinction matrix ($\kappa(1,1) = 2\text{Re}(i\lambda S_{vv}^f)$) was used to compare attenuation from various components within the tree crown.

Table 1 shows that a) attenuation by leaves is higher than branches in all bands; b) backscattering by branches is higher than leaves except at C band; c) backscattering by leaves at P (and L) band is negligible; and d) to account for scattering and

attenuation both leaves and branches must be considered in the model.

Table 2 shows that backscattering of branches at C band is mostly contributed by secondary branches, i.e. AA, BB and CC; at L band by A, B, and C branches, and at P band by the large primary branches, i.e. B, C and D branches.

Table 1. Backscattering and attenuation of leaves and branches. 196000 needles and 105.3 branches per m^3 were assumed.

Type	C Band		L Band		P Band	
	L_{11}	κ_{11}	L_{11}	κ_{11}	L_{11}	κ_{11}
Leaves	2.39e-3	0.6384	1.02e-5	0.13348	2.31e-7	0.07630
Branches	1.47e-3	0.1158	1.0e-3	0.06862	5.57e-4	0.003876

Table 2. Branch physical parameters and their relative volume backscattering (vv) strength. Percentages reflect branch size probabilities.

Type	Diameter (cm)	length (cm)	Probability	Relative σ (%)		
				C Band	L Band	P Band
AA	0.2	15	0.86684	13.66	0.26	0.0
BB	0.4	30	0.10312	43.49	1.26	0.09
CC	0.6	40	0.01605	14.88	1.47	0.11
DD	0.8	75	0.00619	8.01	3.88	0.38
A	1.1	90	0.00481	5.15	14.05	1.3
B	2.4	165	0.00154	4.65	35.64	18.90
C	3.0	260	0.00119	7.44	37.42	54.81
D	3.5	350	0.00025	2.72	6.03	24.57

2.2. Model simulation

The following major backscattering components were considered by the model: 1) direct backscattering from tree crowns; 2) direct backscattering from ground surface attenuated by tree canopy; 3) crown-ground double-bounce scattering; 4) trunk-ground double-bounce scattering; and 5) direct backscattering from trunks.

In the model the ground surface was characterized as very rough - with the standard deviation of the surface height (rms height) of 24.3 cm, and correlation length of 1.0 meter. A geometrical optics model was used to calculate both the backscattering and the scattering in the specular direction. Because of the high attenuation from the tree canopy and the roughness of the surface, the components 3 and 4 were very low, even in P band. The dominant component is the direct backscattering from the tree crown, with some contribution from component 2 at HH and VV polarizations, especially in low biomass and long wavelength cases. The HV backscattering was solely from tree crown scattering. A random leaning angle (normal distribution with mean of zero and standard deviation of 5 degrees) was assigned to each tree, but the contribution to HV backscattering from the direct trunk backscattering was not significant.

Figure 1 shows some simulation results. As mentioned earlier, the number of trees per pixel and average height or dbh are inputs to backscatter model. Thus, both the backscattering coefficients and the total biomass of this pixel can be calculated. The lines in these figures show the simulations results. Biomass of several stands were calculated from available ground truth and are plotted in the figures along with backscattering coefficients extracted from JPL AIRSAR data of June 9, 1991.

3. CONCLUSIONS

Generally, the simulations give satisfactory results, except that the backscattering from L band is about 2 dB higher than the JPL SAR data. The possible coupling between branch sizes and L band wavelength may be the cause of this problem. The

eight distinct categories of branches are far from representing reality.

Also shown in the figure are the ratios of P/C and L/C. In another study (Ranson and Sun, 1992), it was found that the ratio of HV backscattering from a longer wavelength (P or L) to that from a shorter wavelength (C) was a better combination for mapping forest biomass. This ratio enhanced the correlation of the image signature to the standing biomass and compensated for a major part of the variations in backscattering attributed to radar incidence angle.

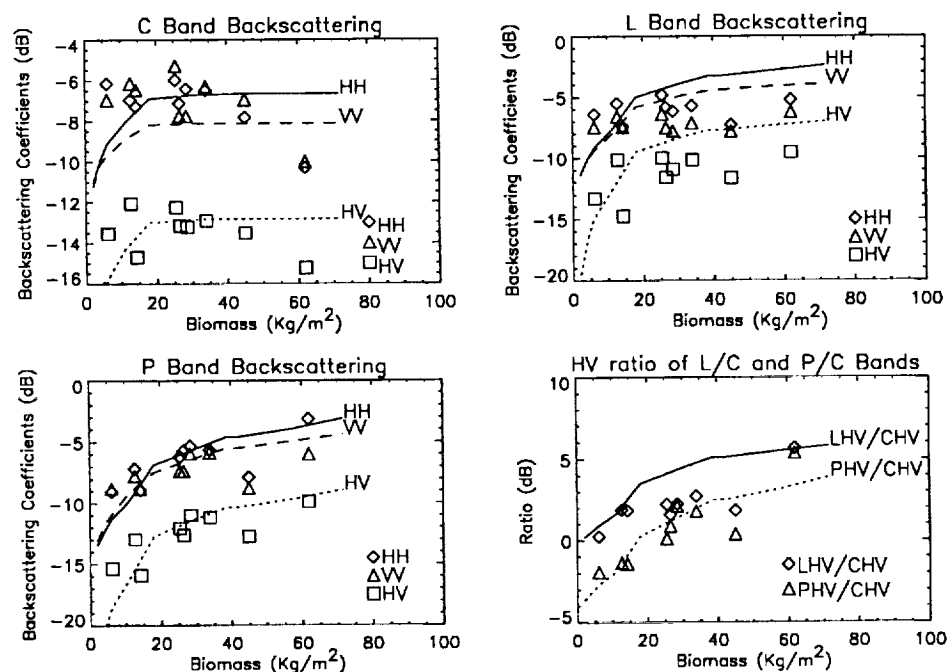


Figure 1. The relationships between backscattering and forest biomass: lines indicate modeling results, and symbols indicate JPL AIRSAR data.

4. REFERENCES

- N. S. Chauhan, R. H. Lang, and K. J. Ranson, Radar modeling of a Boreal forest, *IEEE Transactions on Geoscience and Remote Sensing*, Vol. 29, No. 4, 1991, pp. 627 - 638.
- E. S. Kasischke, N. L. Cristensen, Jr., and M. C. Dobson, The relationship between aboveground biomass and radar backscatter as observed on Airborne SAR imagery, *Proceedings of the Third Airborne Synthetic Aperture Radar (AIRSAR) Workshop*, May 23 and 24, 1991, Jet Propulsion Laboratory, Pasadena, California, pp. 11-21.
- T. Le Toan, A. Beaudoin, J. Riou, and D. Guyon, Relating forest parameters to SAR data, *IGARSS'91*, 1991, pp. 689-692.
- K. J. Ranson, and J. A. Smith, Airborne SAR experiment for forest ecosystems research - Maine 1989 Experiment, *IGARSS'90*, The University of Maryland, College Park, Maryland, 1990, pp. 861-864.
- K. J. Ranson, and G. Sun, Mapping biomass for a northern forest ecosystem using multi-frequency SAR data, *Proceedings of IGARSS'92*, May 1992, Houston, Texas, USA.
- G. Sun, D. S. Simonett, and A. H. Strahler, A radar backscatter model for discontinuous coniferous forests, *IEEE Transactions on Geoscience and Remote Sensing*, Vol. 29, No. 4, 1991, pp. 639-650.

SAR OBSERVATIONS IN THE GULF OF MEXICO

David Sheres

Center for Marine Science
University of S. Mississippi
Stennis Space Center, Mississippi 39529

1. INTRODUCTION

The Gulf of Mexico (GOM) exhibits a wealth of energetic ocean features; they include the Loop Current with velocities of about 2 m/s and strong shear fronts, mesoscale eddies, double vortices, internal waves and the outflow of the "Mighty Mississippi" river. These energetic features can have a strong impact on the economies of the states surrounding the Gulf. Large fisheries, oil and gas production as well as pollution transport are relevant issues. These circulation features in the Gulf are invisible to conventional IR and visible satellite imagery during the Summer months due to cloud cover and uniform surface temperatures. SAR imagery of the Gulf does penetrate the cloud cover and shows a rich assembly of features there year-round. Below are preliminary results from GOM SAR imagery taken by SEASAT in 1978 and by the AIRSAR program in 1991.

2. SEASAT IMAGERY

A search at JPL archive for SAR data (optically processed) along the edges of the Loop Current yielded images with a rich array of features. A number of these images were selected and digitally processed. Here we will look at some of them with an emphasis on circular doughnut like features and their comparison with Shuttle photography of what appears to be the same

features. These features have a relatively dark center surrounded by a bright "doughnut". Their spatial scales vary but are generally of the order of 10 km. They have been observed before (Fu and Holt, SEASAT Views Oceans and Sea Ice With SAR, JPL publication 81-120, 1982) and described as local atmospheric downdrafts with the dark center as a tropical rain cell. Indeed recent in-situ measurements by Trizna at NRL show the inhibiting effect of rain on radar returns confirming the above interpretations of these features.

Large areas in these images are relatively bright or dark suggesting large areas with either high or low radar crosssections. The boundary between these areas is a front, most likely the edge of the Loop Current. These SEASAT images show the power of SAR to monitor energetic features in the GOM during the Summer months when other remote sensors are practically blind. Thus the modulation of waves is a useful means for observing energetic ocean features under all-weather conditions.

AIRSAR IMAGERY OF THE GULF OF MEXICO

During May 19, 1991 we obtained AIRSAR imagery from the JPL/NASA DC-8 in conjunction with in-situ data taken from the RV Tommy Munro and tracked drifter data. A small number of SAR images were processed by the synoptic processor; they do, however, show some interesting characteristics. During the period of the experiment high winds and waves were prevalent. The DC-8 flew a box pattern, off the shelf over the Northern GOM, that included two equivalent passes with a 45 minute time difference between them. These passes were to the West and in one of them a linear bright front was clearly seen while in the other the front was missing. The presentation will include wind data from the RV Munro that was in the same area at the time plus a discussion of different mechanisms for the generation of a linear front. This work is still in progress and I will present as much data as will be available at the time of the presentation.

INVESTIGATION OF AIRSAR SIGNATURES OF THE GULF STREAM

G.R. Valenzuela, J.S. Lee, D.L. Schuler,
G.O. Marmorino, F. Askari, K. Hoppel,
J.A.C. Kaiser, and W.C. Keller

Center for Advanced Space Sensing
Naval Research Laboratory
Washington, DC 20375-5000

1. INTRODUCTION

Extensive AIRSAR measurements were made on 20 July 1990 during the NRL Gulf Stream (GS) experiment which addressed a number of scientific questions relating to SAR imaging of the ocean surface in the presence of variable currents and the background thermohaline circulation (Valenzuela et al. 1991).

In this paper we concentrate on the nature of the electromagnetic (e.m.) backscatter from the North edge of the GS using polarimetric signatures and amplitude imagery from the AIRSAR data.

2. STUDY SITE

On 20 July 1990 the AIRSAR operated from 9 h 49 min to 15 h 45 min EDT. It provided extensive coverage from Norfolk, VA to 37°N, 72°W on the North edge of the GS and South across the GS towards the center of a cold ring (34°18'N, 71°20'W), and return back to Norfolk. For details on the tracks and specific patterns performed see Kobrick (1990).

During the AIRSAR data collection the R/V Cape Henlopen was stationed near the North edge of the GS and remained within 30 km of 36.75°N, 72°W the location of the main thermal front. The winds ranged from 6 to 10 m/s from the south-west (230°T) and waves were almost 1 m high.

3. POLARIMETRIC SIGNATURES

The AIRSAR imagery contained a strong linear feature about 20 km south of the North edge (thermal front) of the GS and weaker signatures were evident on the South edge (Valenzuela et al. 1991). These signatures in the amplitude imagery are strongly frequency and polarization dependent. Therefore, a full polarimetric study was done to obtain further insight on the nature of the e.m. backscatter for these features.

Van Zyl et al. (1987) discussed the theory and application of co-polarized polarimetric signatures to identify the scattering mechanisms from earth surfaces using the shape of the three-dimensional display (Intensity as a function of Orientation and Ellipticity angles) as derived from the transmit and receive polarization vectors operating on the Stokes matrix of the AIRSAR imagery.

In preliminary analysis of polarimetric co-polarized signatures for the North edge of the GS (using one frame from pass GS NS 135-1) (Figure 1) and comparisons with numerical simulations from a second order tilted-Bragg model (Schuler et al. 1992) we have been able to identify that P- and L-band backscatter for the background ocean were consistent with Bragg scattering, while for the linear feature and C band other contributions are present (Figure 2).

4. THERMAL FRONTS SIGNATURES

In addition to the strong linear feature discussed in the previous section, weaker signatures were present in the SAR imagery right on the North edge of the GS (the main thermal front) and another signature on a thermal front about 7 km north.

We have extensive sea truth on these fronts for a quantitative correlation with the SAR imagery (one frame from pass GS SS 360-1) (Figure 3), but here we investigate the frequency and polarization dependence of these signatures for the amplitude imagery. From study of the SAR imagery for these features at P, L and C bands and various polarizations, it is clear that the signatures are largest for HH and HV polarization, and nearly absent for VV polarization.

Furthermore, we note that the mean intensities for P and L bands do not change with azimuth in the image, while C band intensity increases by 2-3 dB towards the warm GS waters (Figure 4). The main thermal front is about pixel 800 in the azimuthal cut and the other front 7 km to the North is about pixel 200. This increase in mean intensity towards the GS is consistent with Ku band scatterometer data from the Henlopen and the NRL/P-3 aircraft.

5. SUMMARY AND CONCLUSIONS

In this work we have used polarimetric analysis and amplitude imagery to investigate the nature of the e.m. backscatter from AIRSAR data near the North edge of the GS during 20 July 1990. The e.m. backscatter for the background ocean is tilted-Bragg for P and L bands, while C band backscatter contains other mechanisms as well, probably specular scattering.

Acknowledgments

We are grateful to the AIRSAR team for collecting and providing the SAR images used in this study.

References

- Kobrick, M., AIRSAR Data Digest Summer 1990, Jet Propulsion Laboratory JPL D-8123, Pasadena, CA, December 1990.
- Schuler, D.L., J.S. Lee, K. Hoppel, and G.R. Valenzuela, Polarimetric SAR Image Signatures of Gulf Stream Features and Ship Wakes, Proc. IGARSS '92, Clear Lake, TX, 24-27 May 1992.
- Valenzuela, G.R., R.P. Mied, A.R. Ochadlick, M. Kobrick, P.M. Smith, F. Askari, R.J. Lai, D. Sheres, J.M. Morrison, and R.C. Beal, The July 1990 Gulf Stream Experiment, Proc. IGARSS '91, I, Espoo, Finland, 3-6 June 1991, pp. 119-122.
- van Zyl, J.J., H.A. Zebker, and C. Elachi, Imaging Radar Polarization Signatures: Theory and Observations, Radio Sci., 22(4) 529-543, 1987.

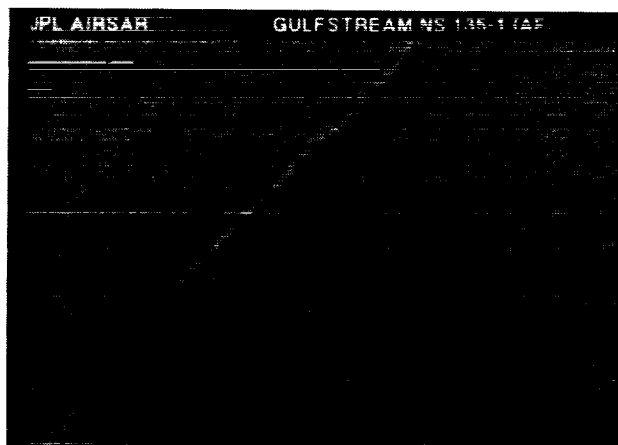


Figure 1. JPL AIRSAR total-power image for a strong linear ocean feature about 20 km south of the North edge of the GS seemingly related to a region of large current gradient.

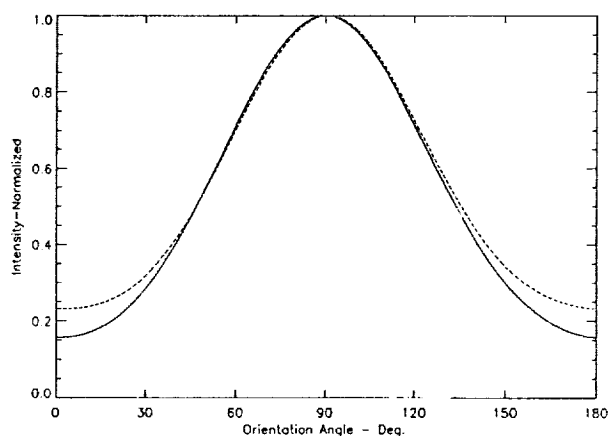


Figure 2. A (linear-pol) slice (40° incidence) of the 3-D polarimetric display of intensity for both the background ocean (solid line) and the strong linear feature (broken line) of Figure 1. Note the increase in horizontal polarization at 0° and 180° angles.

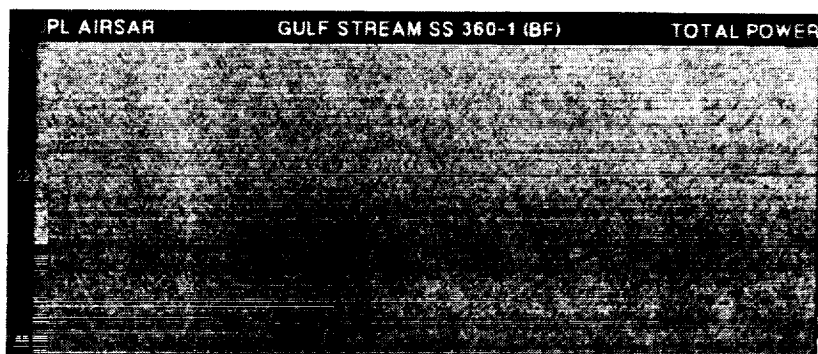


Figure 3. JPL AIRSAR total-power image for the North edge of the GS. The two signatures are associated with the temperature fronts, the one on the r.h.s. is the main front, the North edge of the GS. North is towards the left.

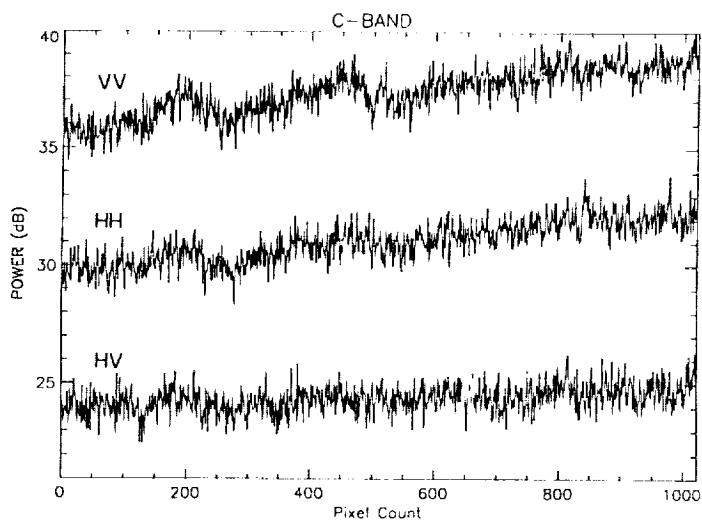


Figure 4. Azimuthal intensity cuts (averages of 50 pixels) of AIRSAR image of Figure 3 for C band and various polarizations at about 55° incidence. The North edge of the GS is about pixel 800, the other temperature front to the north is about pixel 200.

C.J. Calkoen, G.J. Wensink, G.H.F.M. Hesselmanns

Delft Hydraulics
p.o. box 152, 8300 AD Emmeloord, the Netherlands

1. Introduction

Under suitable conditions the bottom topography of shallow seas is visible in remote sensing radar imagery. Two experiments have been performed to establish which remote sensing technique or combination yields optimal imaging of bottom topography and which hydro-meteorological conditions are favourable. A further goal is to gain experience with these techniques.

Two experiments were performed over an area in the North Sea near the measuring platform Meetpost Noordwijk (MPN). The bottom topography in the test area is dominated by sand waves. The crests of the sand waves are perpendicular to the coast line and the dominating (tidal-)current direction. A 4x4 km² wide section of the test area was studied in more detail.

The first experiment was undertaken on August 16, 1989. During the experiment the following remote sensing instruments were used: Landsat-Thematic Mapper, and NASA/JPL Airborne Imaging Radar (AIR). The hydro-meteorological conditions: current, wind, wave, and air and water temperature were monitored by MPN, a ship of Rijkswaterstaat (the OCTANS), and a pitch-and-roll WAVEC-buoy.

The second experiment took place on July 12, 1991. During this experiment data were collected with the NASA/JPL polarimetric SAR, and a five-band helicopter-borne scatterometer. Again the hydro-meteorological conditions were monitored at MPN and the OCTANS. Furthermore, interferometric radar data have been collected.

2. Imaging mechanism and implementation

The imaging mechanism of both the optical and the microwave system is generally agreed to consist of the three following steps:

1. Interaction between bathymetry and (tidal-)current causes modulations in the surface current velocity.
2. Modulations in the surface current give rise to variations in the sea surface roughness or wave spectrum.
3. Variations in the sea surface roughness show up as local modulations in the reflected sun light or radar backscatter.

Based on the above three stage imaging mechanism, an one-dimensional model suite has been implemented:

1. The interaction between bottom topography and current has been modeled by a two stage mechanism. First the depth averaged current is calculated, then the surface current is determined from the current profile (*Davies 1987, Zitman 1992*).
2. The modulation of the spectrum of the short surface waves through wind, dissipation and wave-wave interaction is described by the action balance equation (*Hasselmann 1960, Willebrand 1975*).
3. Finally, the interaction between sea surface and radar is modelled by a two-scale radar backscatter model (*Donelan and Pierson 1987, Calkoen et al. 1990*).

3. Data assimilation

Using the above suite of models, the bottom topography and additional information about sea surface temperature, wind speed, and average current, the radar backscatter can be predicted. In this paper, interest is focused on the inverse: estimation of the

depth from radar backscatter imagery. In principle this can be achieved by explicit inversion of the equations. However, this is not feasible, unless some simplifications are made, because the equations are non-linear, and noise added to the radar backscatter may result in signals outside the range of values attainable by the model. Furthermore, additional information obtained from surveys and charts cannot be used. The data assimilation approach doesn't have these disadvantages. It provides the most likely bottom topography given all available information. The data assimilation approach selects the bottom, which minimizes the difference between measurements and model predictions.

3. Results

The measurements have been compared with results obtained from the numerical models.

1. The measured depth averaged current and the current profile are in good agreement with model predictions (see figure 1).
2. Sea bottom topography was observed in both optical and microwave imagery. However, the practical use of optical data is severely limited by the required sun elevation angle and absence of clouds. Sea bottom topography was not observed in the C-band SAR imagery. The usefulness of the recorded L-band imagery is limited by dark broad bands caused by interference problems in the radar system. Both HH and VV polarized P-band imagery show the bottom topography distinctly. The VV polarized P-band imagery corrected for incidence angle dependence is shown in figure 2.
3. Inversion of the model suite by means of the data-assimilation approach is possible. The estimated depth based on VV polarized P-band imagery is shown in figure 3.

4. Conclusions and discussion

The best depth estimates were obtained from VV polarized P-band imagery. The position of the crests of the sand waves can be assessed within 25 metres (two pixels), and the height of the crests within 1 m. The errors can partially be explained by the time difference between the depth information (1984) and the radar data (1989). At present the data obtained during the second experiment are still being calibrated and/or pre-processed. The interferometric radar data can be used to determine the movements of the water surface. Therefore, it may provide additional information useful in the data-assimilation scheme.

5. References

- Calkoen, C.J., van Halsema, D., Jähne, B., Janssen, J.A.M., Oost, W.A., Snoeij, P., and Vogelzang, J., 1990, *VIERS-1 progress report part-2, completion of the laboratory experiments*, BCRS-report, bcrs 90-27.
- Davies, A.M., 1988, On formulating two-dimensional vertically integrated hydrodynamic numerical models with an enhanced representation of bed stress. *Journal of Geophysical Research*, **93C**, 1241-1263.
- Donelan, M.A., and, Pierson, W.J., 1987, Radar scattering and equilibrium ranges in wind generated waves with application to scatterometry. *Journal of Geophysical Research*, **92C**, 4971-5029.
- Hasselmann, K., Grundgleichungen der Seegangsvorhersage, 1960, *Schiffstechnik*, **7**, 191-195.
- Willebrand, J., 1975, Energy transport in a nonlinear and inhomogeneous random gravity wave field. *Journal of Fluid Mechanics*, **70**, 113-126.
- Zitman, T.J., 1992, Quasi 3-dimensional current modelling based on a modified version of Davies' shape function approach. *Continental Shelf Research*, **12**, 143-158.

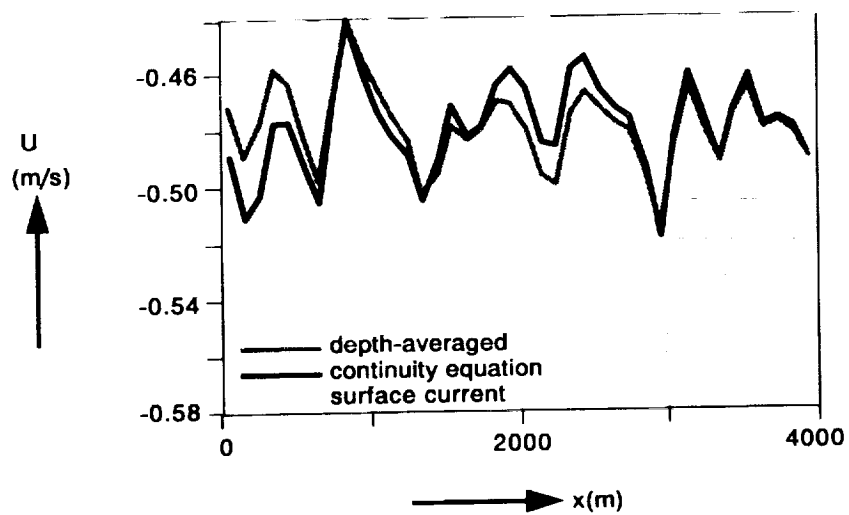


Figure 1. Comparison of predicted current and measured current.

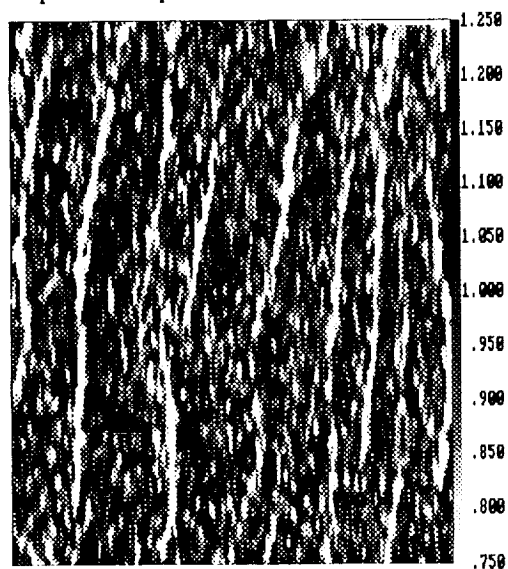


Figure 2. VV-polarized P-band radar backscatter corrected for incidence angle dependence.

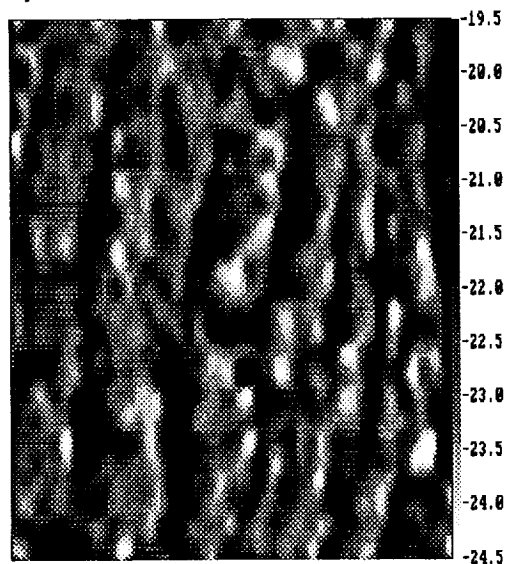


Figure 3. Estimated depth based on VV-polarized P-band radar backscatter imagery.

SEA BOTTOM TOPOGRAPHY IMAGING WITH SAR

M.W.A. van der Kooij¹, G.J. Wensink², J. Vogelzang³

¹Physics and Electronics Lab TNO, P.O. Box 96864, 2509 JG The Hague, The Netherlands, ²Delft Hydraulics, ³Department of Water Control

It is well known that under favorable meteorological and hydrodynamical conditions the bottom topography of shallow seas can be mapped with airborne or spaceborne imaging radar. This phenomenon has been observed for the first time in 1969 by de Loor and co-workers in Q-band Side Looking Airborne Radar (SLAR) imagery of sandwaves in the North Sea (de Loor and Brunsveld van Hulst '78, Alpers and Hennings '84, Shuchman et al '85).

It is now generally accepted that the imaging mechanism consists of three steps:

1. Interaction between (tidal) current and bottom topography causes spatial modulations in the surface current velocity.
2. Modulations in the surface current velocity give rise to variations in the spectrum of wind-generated waves, as described by the action balance equation.
3. Variations in the wave spectrum show up as intensity modulations in radar imagery.

In order to predict radar backscatter modulations caused by sandwaves, an imaging model, covering the three steps, has been developed by the Dutch Sea Bottom Topography Group (Vogelzang et al '89a, Vogelzang et al '89b, Vogelzang et al '91a). This model and some model results will be shown.

On August 16, 1989 an experiment has been performed with the polarimetric P-, L-, and C-band SAR of NASA/JPL. One scene has been recorded in SAR mode (Vogelzang et al '91b). On July 12 1991 another three scenes were recorded, of which one was in the ATI-mode (Along-Track Interferometer).

These experiments took place in the test area of the Sea Bottom Topography Group, 30 km off the Dutch coast, where the bottom topography is dominated by sand waves. In-situ data were gathered by a ship in the test area and on "Measuring Platform Noordwijk", 20 km from the centre of the test area.

The radar images made during the experiment were compared with digitized maps of the bottom. Furthermore, the profiles of radar backscatter modulation were compared with the results of the model. During the workshop some preliminary results of the ATI measurements will be shown.

- [1] W. Alpers and I. Hennings, "A theory of the imaging mechanism of under-water bottom topography by real and synthetic aperture radar", *Journal of Geophysical Research* 89C, pp 10529-10546, 1984
- [2] G.P. de Loor and H.W. Brunsveld van Hulten, "Microwave measurements over the North Sea", *Boundary Layer Meteorology* 13, pp 113-131, 1978.
- [3] R.A. Shuchman, D.R. Lyzenga and G.A. Meadows, "Synthetic Aperture Radar imaging of ocean bottom topography via tidal-current interactions : theory and observations", *International Journal of Remote Sensing* 6, pp 1179-1200, 1985.
- [4] J. Vogelzang, "The mapping of bottom topography with imaging radar : a comparison of the hydrodynamic modulation in some existing models", *International Journal of Remote Sensing* 9, pp 1503-1518, 1989.
- [5] J. Vogelzang, G.J. Wensink, G.P. de Loor, H.C. Peters and H. Pouwels, "Mapping bottom topography with X-band SLAR", in *Proceedings IGARSS '89*, 1989, pp 2338-2341.
- [6] J. Vogelzang, G.J. Wensink, M.W.A. van der Kooij and G. van der Burg, "Sea bottom topography with polarimetric P-, L- and C-band SAR", in *Proceedings IGARSS '91*, 1991, pp 2031-2034.
- [7] J. Vogelzang, G.J. Wensink, M.W.A. van der Kooij and G. van der Burg, "Sea bottom topography with polarimetric P-, L- and C-band SAR", Netherlands Remote Sensing Board, report 91-40, 1991.

**PRELIMINARY RESULTS OF POLARIZATION SIGNATURES
FOR GLACIAL MORAINES IN THE MONO BASIN,
EASTERN SIERRA NEVADA.**

Richard R. Forster, Andrew N. Fox and Bryan Isacks

Cornell University
Department of Geological Sciences
Snee Hall
Ithaca, New York 14853-1504

1. INTRODUCTION

The valleys of the Mono Basin contain several sets of lateral and terminal moraines representing multiple stages of glaciation. The semi-arid climate with slow weathering rates has preserved sequences of nested younger moraines within older ones. There is a well established relative chronology (Sharp and Birman 1963, Burke and Birkeland 1979, Gillespie 1982) and recently exposure dating has provide a new set of numerical dates (Phillips et al. 1990). The moraines span the late Wisconsin (11-25 ka) to the Illinoian (130-190 ka) glaciations. We are using the Mono Basin area as a "calibration site" to establish remote dating techniques for eventual transfer to the more inaccessible but geomorphically and climatically similar moraines of the South American Andes Mountains. Planned polarimetric SAR imagery acquired by JPL AIRSAR (South American Campaign) and SIR-C (Andes super-site) will be analyzed to establish chronologies of previously undated moraine sequences in a study of Pleistocene climatic change in the Southern Hemisphere.

The dry climate and sparse vegetation is also favorable for correlation of ground surface roughness with radar polarization signature. The slow weathering processes acting over thousands of years reduce the size, frequency and angularity of surface boulders while increasing soil development on the moraines. Field observations based on this hypothesis (Sharp and Birman 1963) result in relative ages consistent with those inferred from nested position within the valley. Younger moraines, therefore, will appear rougher than the older smoother moraines at scales measurable at AIRSAR wavelengths. Previously documented effects of ground surface roughness on polarization signatures (Evans et al. 1988, Ray et al. 1991) suggest that analysis of moraine polarization signatures can be useful for relative dating. The technique may be extended to predict numerical ages.

The data set reported here were acquired on September 8, 1989 with the JPL AIRSAR collecting polarimetric imagery at C- (5.6 cm), L-(24 cm) and P-band(68 cm) with a flight-line parallel to the strike of the mountains. Phase calibration was performed on the analyzed scene by setting the co-phase of a smooth lake to zero as described in Zebker and Lou (1990). Absolute amplitude calibration was not possible because corner reflectors were not deployed.

2. ANALYSIS

The Walker Valley moraine complex (Bloody and Saw Mill Canyon) was chosen for initial analysis because it contains moraines from five distinguishable glacial episodes (Table 1). Estimates of the surface roughness of the crests of the moraines were determined from 1-D Fourier transforms of a series of 15 m linear push-rod profiles (10 cm horizontal spacing, 1.0 mm vertical resolution) from the moraine crests (Fox 1989). This measure of surface roughness was found to correlate with the relative moraine ages

(Table 1). The crests were measured because they were the areas of minimum soil development and least vegetation, enhancing boulder exposure, and thus provide the optimal discrimination based on ground surface roughness. Efforts were made to avoid vegetation during profiling. Fox found that surface roughness correlated best with the image pixel DN values for P-band HH when compared to linear polarizations of the three bands (Fox 1991). The following preliminary analysis will focus on P and L-band polarization signatures because of their sensitivity to the large scale roughness presented by individual boulders.

Moraine (Glaciation)	Age [ka] (best estimate)	Surface Roughness
Tioga	14 a	6.70
Tenya	40 a	6.51
Tahoe Younger	60-85 b	6.37
Tahoe Older	<118 c	6.22
Mono Basin	130 a	5.12

Table 1. Walker Valley moraine classification with estimated age and measured ground surface roughness. a- (Crook and Gillespie 1986) b- (Bursik 1989) c- (Gillespie 1982)

Polarization signatures were created for each moraine from pixels along and adjacent to their crests'. The initial results are based on calculations from typical signatures of each moraine. Further research will include more samples for a statistically sound study.

The scattering from an object will become more diffuse as the roughness of the target increases relative to the illuminating wavelength. Polarization signatures reflect the degree of diffuse scattering in their measure of co- and cross-polarized radar cross section as a function of all possible transmit polarizations. The most common way of estimating the diffuse component is with the pedestal height (vanZyl et al. 1987) calculated as the ratio of the co-polarized minimum to the signature maximum. An alternative approach which uses only circular polarization for estimation of diffusivity is the circular polarization ratio (referred to here after as CPR) as defined by Ray et al. (1991). The right-hand circular polarization ratio is calculated by dividing the cross-polarization right-hand response (transmit RH receive LH, expected for a smooth object) by the co-polarized right-hand response (transmit RH receive RH expected from a diffuse object), thus comparing the directly reflected power to the diffusely scattered power. Rough objects would theoretically have lower CPR's than smooth objects (relative to wavelength).

Pedestal heights and right-hand CPR (direct/diffuse) values for the five moraines at P- and L-bands are shown in Table 2. The P-band data show consistent trends for decreasing roughness with successive glaciations. The pedestal height decreases and the right-hand CPR increases. The L-band data show the same trends except for the Mono Basin moraine, it does not appear to be the smoothest (oldest) using either the pedestal or the CPR technique.

Moraine (Glaciation)	Pedestal Height		R-H Circular Polarization Ratio	
	L	P	L	P
Tioga	.1280	.1633	.4621	.1243
Tenya	.1230	.1587	.5776	.2143
Tahoe Younger	.0888	.0904	.6549	.4429
Tahoe Older	.0714	.0702	1.000	.6143
Mono Basin	.1178	.06442	.7698	1.000

Table 2. Walker Valley moraine classification with L- and P-band pedestal heights and right-hand circular polarization ratios (normalized)

3. SUMMARY

The preliminary results indicate that the polarization signatures from the glacial moraines of the Walker Valley may be used as a relative dating tool. Specifically, the parameters of pedestal height and the ratio of circular expected to circular diffuse polarization have shown correlation with moraine age at P-band and to a lesser degree at L-band. The established correlation of relative moraine age with crest ground surface roughness provides the physical link from scattering mechanism to relative age. The violation of the trends at L-band for the Mono Basin moraine may be the result of diffuse scattering from vegetation creating the "appearance" of a rougher surface. The Mono Basin moraines have the most densely vegetated crests. The ground shrubs may have less of a response at the longer P-band wavelength. This hypothesis may be further supported if the Mono Basin moraine appears even rougher at C-band.

Additional signatures need to be acquired at more locations representing a diverse set of incidence angles, local incidence angles, pixel numbers used for signature, and crest orientations to confirm the observed trends. The shape of the polarization signatures will be further analyzed for implications of the nature of the scattering mechanism. A more detailed and comprehensive characterization of the moraine surface roughness is planned through a high resolution DEM to be generated from low altitude stereo photogrammetry. The potential exists for relative dating of moraines in inaccessible areas from remote polarimetric SAR platforms.

REFERENCES

- Burke, R. M., and Birkeland, P. W., 1979, Reevaluation of multiparameter relative dating techniques and their application to glacial sequences along the eastern escarpment of the Sierra Nevada, California. *Quaternary Research*, 11, 21-51.
- Bursik, M. I., 1989, Late Quaternary volcano-tectonic evolution of the Mono Basin Eastern California, Ph. D. Thesis, Calif. Instit. Tech.
- Crook, R., Gillespie, A. R., 1986, Weathering rates in granitic boulders measured by p-wave speeds, in Rates of Chemical Weathering of Rocks and Minerals, Colman, S. M. and Dethier, D. P., eds., Academic Press, Orlando, p.395.
- Evans, D. L., Farr, T. G., van Zyl, J. J., Zebker, H. A., 1988, Radar Polarimetry: Analysis Tools and Applications, *IEEE Transactions on Geoscience and Remote Sensing*, 26, 774-789.
- Fox, A. N., Isacks, B., Bloom, A., Fielding, E., McMury, D., 1991, Airborne SAR determination of relative ages of Walker Valley moraines, Eastern Sierra Nevada, *Proceedings of the Third Airborne AIRSAR Workshop*, JPL Publication 91-30, 128.
- Fox, A. N., 1989, Change in surface roughness through time on moraines in Mono Basin, California: A comparison of field profiler and aircraft radar data, *Geological Society of America Abs. with Prog.*, 21,270.
- Gillespie, A. R., 1982, Quaternary glaciation and tectonism in the South-eastern Sierra Nevada, Inyo County, California, Ph. D. Thesis, Calif. Instit. Tech.
- Phillips, F. M., Zreda, M. G., Smith, S. S., Elmore, D., Kubik, P. W., Sharma, P., 1990, Cosmogenic Chlorine-36 chronology for glacial deposits at Bloody Canyon, Eastern Sierra Nevada, *Science*, 248, 1529-1532.
- Ray, T. W., Farr, T. G., vanZyl, J. J., 1991, Polarization signatures for abandoned agricultural fields in the Manix Basin Area of the Mojave Desert, *Proceedings of the Third Airborne AIRSAR Workshop*, JPL Publication 91-30, 117-125.
- Sharp R. P., and Birman, J. H., 1963, Applications to classical sequence of Pleistocene glaciations, Sierra Nevada, California, *Geological Society of America Bulletin*, 72, 1079-1086
- vanZyl, J. J., Zebker, H. A., Elachi, C., 1987, Imaging radar polarization signatures: Theory and observation, *Radio Science*, 22, 529-543.
- Zebker, H. A., Lou, Y., 1990, Phase calibration of imaging radar polarimeter Stokes Matrices, *IEEE Transactions on Geoscience and Remote Sensing*, 28, 246-252.

DETECTING SURFACE ROUGHNESS EFFECTS ON THE ATMOSPHERIC BOUNDARY LAYER VIA AIRSAR DATA: A FIELD EXPERIMENT IN DEATH VALLEY, CALIFORNIA

Dan G. Blumberg and Ronald Greeley

*Department of Geology, Arizona State University
Tempe, Arizona 85287-1404*

1. INTRODUCTION

The part of the troposphere influenced by the surface of the earth is termed the atmospheric boundary layer (*Stull 1988*). Flow within this layer is influenced by the roughness of the surface; rougher surfaces induce more turbulence than smoother surfaces and, hence, higher atmospheric transfer rates across the surface. Roughness elements also shield erodible particles, thus decreasing the transport of windblown particles. Therefore, the aerodynamic roughness length (z_0) is an important parameter in aeolian and atmospheric boundary layer processes as it describes the aerodynamic properties of the underlying surface. z_0 is assumed to be independent of wind velocity or height, and dependent only on the surface topography (*Bagnold 1941; Greeley and Iversen 1985*). It is determined using *in situ* measurements of the wind speed distribution as a function of height. For dry, unvegetated soils the intensity of the radar backscatter (σ^0) is affected primarily by surface roughness at a scale comparable with the radar wavelength. Thus, both wind and radar respond to surface roughness variations on a scale of a few meters or less. *Greeley et al. (1991)* showed the existence of a correlation between z_0 and σ^0 . This correlation was based on measurements over lava flows, alluvial fans, and playas in the southwest deserts of the United States. In this report we show that the two parameters behave similarly also when there are small changes over a relatively homogeneous surface.

2. EXPERIMENTAL DETAILS

A study was conducted during the Spring of 1991, in which the atmospheric boundary layer was assessed and compared with σ^0 values obtained from AIRSAR data. Five masts equipped with wind anemometers, wind vanes, and temperature sensors were deployed over an unvegetated alluvial fan on the eastern edge of the Stove Pipe Wells Dune Field in Death Valley, California. The alluvial fan lies at sea level below the Grapevine Mountains, and receives its deposits primarily from Mud Canyon. The predominant airflow in this area is NNW-SSE, across the fan.

Micrometeorologic data were collected for a period of 10 weeks and reduced following a procedure by White (*unpublished*) to derive the surface shear velocity, the Richardson number (*Stull 1988*), z_0 per wind profile, and a mean z_0 per data set. Each data set consisted of approximately 100 wind profiles for a given wind direction per site (Table 1). AIRSAR data were obtained at the site using bands C (5.6 cm), L (24 cm), and P (68 cm). The radar data were calibrated using POLCAL software (*vanZyl et al. 1990*), based on trihedral corner reflectors that were deployed prior to the imaging.

3. RESULTS

Mean σ^0 values were extracted for the location of each of the five masts (Table 2) (values did not need to be normalized for variations in incidence angles, as all incidence angles were between 45° to 47°). Figure 1 shows that σ^0 and z_0 change simultaneously and in the same direction for winds from the north-northwest, suggesting that they are responding to similar surficial changes. These variations are probably induced by roughness changes comparable with the radar wavelength. Surface roughness measurements were conducted using an electronic distance meter, a surface template, and a laser profiler. The surface roughness data are being analyzed to determine if the changes in surface roughness corroborate the radar and wind results. Winds from the south-southeast showed larger variations of z_0 , suggesting that they are affected by the fluvial dissection found south of the study site.

4. CONCLUSIONS

Based on the north-northwesterly winds we conclude that z_0 and σ^0 have similar spatial patterns even when measured over a relatively homogeneous surface. L-band cross-polarized data correlate best with z_0 over a dry, unvegetated alluvial fan. Further work is required to determine the scales of roughness affecting these parameters.

Table 1. z_0 across the alluvial fan

Mast	Distance from northwest to southeast (m)	z_0 (m) southeasterly winds	z_0 (m) northwesterly winds
2	200	0.00608	0.00208
3	400	0.00055	0.00076
4	700	0.00806	0.00288
5	1000	0.00240	0.00310

Table 2. σ^0 variations across the alluvial fan

Mast	C-band (dB)			L-band (dB)			P-band (dB)		
	HH	HV	VV	HH	HV	VV	HH	HV	VV
1	-12.72	-20.97	-12.32	-21.92	-34.70	-20.06	-31.31	-47.01	-27.14
2	-14.29	-22.40	-12.77	-24.43	-36.94	-22.46	-34.27	-49.73	-30.78
3	-13.87	-22.52	-12.85	-25.34	-40.61	-22.96	-35.00	-50.65	-31.87
4	-13.16	-22.47	-13.00	-23.40	-37.39	-21.18	-32.74	-48.78	-29.67
5	-12.35	-21.71	-11.66	-22.36	-35.66	-20.48	-32.20	-49.01	-29.04

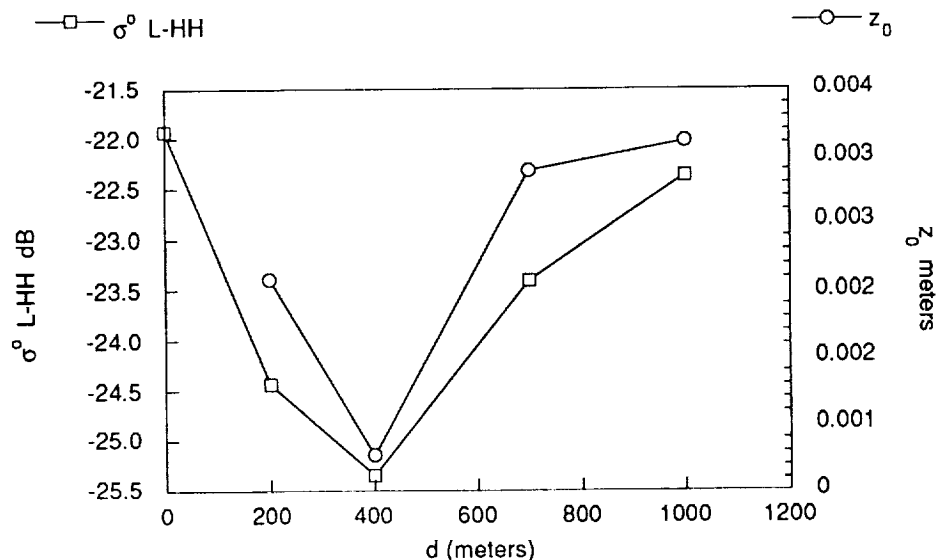


Figure 1: Mean radar backscatter in L-band (24 cm) , and z_0 values for northwesterly winds versus the locations of the masts across the alluvial fan. For the most northern station no z_0 value was determined due to instrument problems.

References

- Bagnold R.A., 1941, *The Physics of Blown Sand and Desert Dunes*, Methuen, London, pp. 265.
- Greeley R., and J.D. Iversen, 1985, *Wind as a Geological Process*, Cambridge, New York, pp. 333.
- Greeley R., L. Gaddis, N. Lancaster, A. Dobrovolskis, J. Iversen, K. Rasmussen, S. Saunders, J. vanZyl, S. Wall, H. Zebker, and B. White, 1991, Assessment of Aerodynamic Roughness via Airborne Radar Observations, *Acta Mechanica*, Suppl. 2, pp. 77-88.
- Stull R.B., 1988, *An Introduction to Boundary Layer Meteorology*, Kluwer Academic Publishers, Netherlands, pp. 666.
- vanZyl J., C.F Burnette, H.A. Zebker, A. Freemcan, and J. Holt, 1990, *POLCAL Users Manual*, JPL, D-7715, Pasadena, pp. 49.

EXTRACTION OF QUANTITATIVE SURFACE CHARACTERISTICS FROM AIRSAR DATA FOR DEATH VALLEY, CALIFORNIA

K. S. Kierein-Young and F. A. Kruse

Center for the Study of Earth from Space (CSES)
Cooperative Institute for Research in Environmental Sciences (CIRES)
University of Colorado, Boulder, Colorado 80309-0449
and

Department of Geological Sciences
University of Colorado, Boulder, Colorado 80309

1. INTRODUCTION

Polarimetric Airborne Synthetic Aperture Radar (AIRSAR) data were collected for the Geologic Remote Sensing Field Experiment (GRSFE) over Death Valley, California, USA, in September 1989 (Evans and Arvidson, 1990; Arvidson et al, 1991). AIRSAR is a four-look, quad-polarization, three frequency instrument. It collects measurements at C-band (5.66 cm), L-band (23.98 cm), and P-band (68.13 cm), and has a GIFOV of 10 meters and a swath width of 12 kilometers. Because the radar measures at three wavelengths, different scales of surface roughness are measured. Also, dielectric constants can be calculated from the data (Zebker et al, 1987).

The AIRSAR data were calibrated using in-scene trihedral corner reflectors to remove cross-talk; and to calibrate the phase, amplitude, and co-channel gain imbalance (van Zyl, 1990). The calibration allows for the extraction of accurate values of rms surface roughness, dielectric constants, σ_0 backscatter and polarization information. The radar data sets allow quantitative characterization of small scale surface structure of geologic units, providing information about the physical and chemical processes that control the surface morphology. Combining the quantitative information extracted from the radar data with other remotely sensed data sets allows discrimination, identification and mapping of geologic units that may be difficult to discern using conventional techniques.

2. INVERSION AND ANALYSIS

The first-order small perturbation model (van Zyl et al, 1991; Valenzuela, 1967) was used to estimate the surface power spectral density at every pixel by performing an inversion of the AIRSAR data. This model is valid only for very smooth surfaces. Therefore, only playa, smooth salt pans and alluvial fan surfaces were used in this study. Results from the small perturbation model inversion are three values, one for each of the radar frequencies, that describe the power spectral density of the surface. The power spectrum of a geologic surface is approximately linear in log-log space (Brown and Scholz, 1985). Fitting the three points from the inversion with a line using a least-squares method produces slope and intercept values that allow calculation of the fractal dimension of the surface and a rms surface roughness value.

The slope of the power spectrum is related to the two-dimensional fractal dimension of the surface. The fractal dimension of a surface describes the scaling properties of the topography (Mandelbrot, 1982). A surface may have a fractal dimension between 2 and 3 and as the fractal dimension increases, heights of nearby points become more independent (Brown and Scholz, 1985). The intercept of the power spectrum can be directly related to a rms surface roughness using forward modelling. Using the fractal dimension and rms surface roughness calculated from the radar inversion power spectrum, a synthetic three dimensional plot can be made that represents the surface (Huang and Turcotte, 1989; Kierein-Young et al, 1992).

3. RESULTS AND CONCLUSIONS

Radar inversions were performed using two dielectric constant cases for polygon averages of four surfaces in Death Valley. The surfaces include a playa, smooth salt, alluvial fan with desert pavement, and a rough alluvial fan. In both of the dielectric constant cases, the rms surface roughness is smallest for the playa, increases for the smooth salt and fan with desert pavement, and is largest for the rough fan. The fractal dimension is largest for the smoothest surface, the playa, and smaller for the rougher surfaces. This indicates that nearby points on the smoother surfaces are more independent and nearby points on the rougher surfaces are more correlated. Therefore, the smooth surfaces have a more equal distribution of all wavelengths of roughness while the rough surfaces have more longer wavelength roughness. Figure 1 shows the synthetic surfaces for the four areas with the dielectric constants equal to 3.0. In the case when dielectric constants are calculated in the inversion, some bad values were obtained so more analysis is needed. In this case the fractal dimensions are slightly smaller and the rms roughness values are higher than in the dielectric constant equals 3.0 case. The values of the dielectric constants calculated in the inversion fall within a reasonable range for the surfaces studied (Ulaby et al, 1982). Dielectric field and laboratory measurements will be made to verify the accuracy of these values.

Combining knowledge of the surface structure and roughness of geologic units with data from other instruments allows for the determination of the processes that control the surface. For example, water vapor and liquid water maps were generated from Airborne Visible/Infrared Imaging Spectrometer (AVIRIS) data in Death Valley (Kierein-Young and Kruse, 1991). These maps show the distribution of a hydrological process, the water content of the surface. The water distribution was found to correspond with the surface roughness variations where wet areas are smooth and drier areas rougher. The combination of surface water distribution with surface structure information will help in determining why the salt flats are spatially variant.

4. ACKNOWLEDGEMENTS

Portions of this work were supported under a NASA Graduate Student Researchers Grant NGT-50728. Portions of this work were supported under the SIR-C project by NASA/JPL contract 958456.

5. REFERENCES

- Arvidson et al., 1991, GRSFE CD-ROM and documentation, version 1: USA_NASA_PDS_GR_0001, Planetary Data System, NASA (9 CD-ROMs).
- Brown, Stephan R. and Christopher H. Scholz, 1985. Broad bandwidth study of the topography of natural rock surfaces, *Journal of Geophysical Research*, V. 90, No. B14, pp. 12,575-12,582.
- Evans, D. L., and Arvidson, R. E., 1990, The Geologic Remote Sensing Field Experiment (GRSFE): Overview of initial results: in *Proceedings, IGARSS '90*, University of Maryland, College Park, Md., The Institute of Electrical and Electronics Engineers, Inc. (IEEE), New York, p. 1347.
- Huang, J. and D. L. Turcotte, 1989. Fractal mapping of digitized images: Application to the topography of Arizona and comparisons with synthetic images, *Journal of Geophysical Research*, V. 94, No. B6, pp. 7491-7495.
- Kierein-Young, K. S., F. A. Kruse and A. B. Lefkoff, 1992. Quantitative analysis of surface characteristics and morphology in Death Valley, California using AIRSAR data, in *Proceedings IGARSS '92* (in press).

- Kierein-Young, K. S. and F. A. Kruse, 1991. Quantitative Investigations of Geologic Surfaces utilizing Airborne Visible/Infrared Imaging Spectrometer (AVIRIS) and Polarimetric Radar (AIRSAR) Data for Death Valley, California, in Proceedings of the Eighth Thematic Conference on Geologic Remote Sensing, V.1, pp. 495-506.
- Mandelbrot, B. B., 1982. The Fractal Geometry of Nature, W. H. Freeman, San Francisco, California.
- Ulaby, Fawwaz T., Richard K. Moore, and Adrian K. Fung, 1982. Microwave Remote Sensing Active and Passive, Addison-Wesley Publishing Company, Massachusetts.
- Valenzuela, G. R., 1967. Depolarization of EM waves by slightly rough surfaces, IEEE Transactions on Antennas and Propagation, V. AP-15, No. 4, PP. 552-557.
- van Zyl, Jakob J., 1990. Calibration of Polarimetric Radar Images Using Only Image Parameters and Trihedral Corner Reflector Responses, IEEE Transactions on Geoscience and Remote Sensing, V. 28, No. 3, pp.337-348.
- van Zyl, Jakob J., Charles F. Burnette and Tom G. Farr, 1991. Inference of surface power spectra from inversion of multifrequency polarimetric radar data, Geophysical Research Letters, V. 18, No. 9, pp. 1787-1790.
- Zebker, Howard A., Jakob J. van Zyl, and Daniel N. Held, 1987. Imaging Radar Polarimetry From Wave Synthesis, Journal of Geophysical Research, V. 92, No. B1, pp. 683-701.

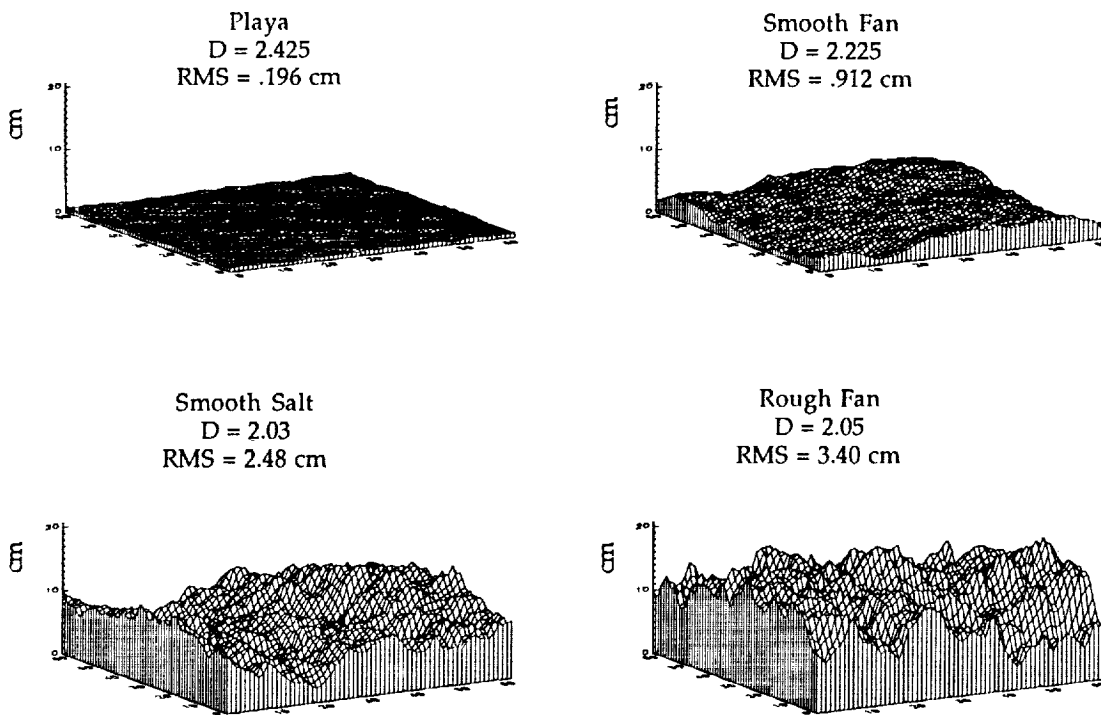


Figure 1. Synthetic surfaces calculated from radar inversion results assuming dielectric constants equal to 3.0.

The TOPSAR Interferometric Radar Topographic Mapping Instrument

HOWARD A. ZEBKER, SØREN N. MADSEN, JAN MARTIN
Jet Propulsion Laboratory
California Institute of Technology

GIOVANNI ALBERTI AND SERGIO VETRELLA
CO.RI.S.T.A.

ALESSANDRO CUCCI
Alenia S.p.A.

Abstract

We have augmented the NASA DC-8 AIRSAR instrument with a pair of C-band antennas displaced across track to form an interferometer sensitive to topographic variations of the Earth's surface. The antennas were developed by the Italian consortium Co.Ri.S.T.A., under contract to the Italian Space Agency (ASI), while the AIRSAR instrument and modifications to it supporting TOPSAR were sponsored by NASA. A new data processor was developed at JPL for producing the topographic maps, and a second processor was developed at Co.Ri.S.T.A. All the results presented below were processed at JPL. During the 1991 DC-8 flight campaign, data were acquired over several sites in the United States and Europe, and topographic maps were produced from several of these flight lines. Analysis of the results indicate that statistical errors are in the 2-3 m range for flat terrain and in the 4-5 m range for mountainous areas.

Introduction

We have implemented an interferometric synthetic aperture radar system for topographic mapping applications (TOPSAR) on the NASA DC-8 aircraft. NASA /JPL currently operates a multifrequency (P, L, and C bands), multipolarimetric radar (AIRSAR) on board this aircraft. The TOPSAR implementation uses much of the existing AIRSAR hardware, although several modifications were required to optimize performance in the topographic mapping mode. When in use, TOPSAR effectively replaces the C-band polarimeter instrument, but the remaining L- and P-band systems are undisturbed and operate together with the topographic mapper; therefore the combined instrument produces simultaneous L- and P-band fully polarimetric plus C-band VV polarization backscatter images in addition to the topographic product.

In this paper we first describe our implementation, including system design parameters, required modifications to the existing AIRSAR hardware, and new antenna design. We then discuss data processing strategy and display some example interferometric images. Finally, we analyze an image acquired over Ft. Irwin, California, in terms of height accuracy.

Background

Interferometric radar has been proposed and successfully demonstrated as a topographic mapping technique by Graham [1], Zebker and Goldstein [2], and Gabriel and Goldstein [3]. Two distinct implementation approaches have been discussed for topographic radar interferometers which differ in how the interferometric baseline is formed. In one case a single antenna and radar system illuminates a given surface at two different times but with nearly the same viewing geometry, forming a synthetic interferometer. This case has been implemented both from spaceborne platforms (see, for example, Goldstein *et al.*, [4]) and also from aircraft (Gray and Farris-Manning [5]). In the second approach the baseline is formed by two physical antennas which illuminate a given area on the ground simultaneously. This is the approach used originally by Graham [1] and also by Zebker and Goldstein [2] for the NASA CV-990 radar; it is the approach used here.

Review of theory

Consider a set of two antennas A1 and A2 as shown in figure 1. The surface topography is given by $z(y)$,

h is the aircraft altitude, the baseline distance is B , the range to a point on the ground is ρ , the look angle θ , and the angle of the baseline with respect to horizontal is α . Radar echoes are transmitted from antenna A1 and received simultaneously at A1 and A2; thus the difference in path lengths is δ , which depends on the baseline distance, baseline angle, range, look angle, and the height of the point $z(y)$. The measured phase of the interferometer is directly proportional to this distance, with the constant of proportionality $\frac{2\pi}{\lambda}$. A little algebra and geometry yield the following equations for height as a function of these parameters:

$$\delta = \frac{\lambda\phi}{2\pi} \quad (1)$$

$$\sin(\alpha - \theta) = \frac{(\rho + \delta)^2 - \rho^2 - B^2}{2\rho B} \quad (2)$$

$$z(y) = h - \rho \cos \alpha \cos(\alpha - \theta) - \rho \sin \alpha \sin(\alpha - \theta) \quad (3)$$

where ϕ is the measured phase, and λ is the wavelength.

Differentiation of (1-3) yields the error in height estimate as a function of the error in phase estimate:

$$\sigma_h = \frac{\lambda\rho}{2\pi B} [\sin \alpha - \cos \alpha \tan(\alpha - \theta)] \sigma_\phi \quad (4)$$

where σ_h and σ_ϕ are the standard deviations of height and phase, respectively.

There exists an optimum baseline distance that minimizes the total height error [Rodriguez and Martin, 6]; this optimum is quite broad and for high (≥ 10 dB) signal to noise ratio systems can be anywhere in the range of 0.2 - 0.8 of the critical value which may be calculated by (Zebker and Villasenor [7]):

$$B_c = \frac{\lambda\rho}{R_y} \tan \theta \quad (5)$$

where R_y is the slant range resolution. Note that this equation differs from that of Zebker and Villasenor by a factor of $2 \cos \theta \sin \theta$ as they were restricted to horizontal baselines, used the ground rather than slant range resolution, and assumed a single antenna in repeat-track configuration rather than two physical antennas as we use in TOPSAR. Another significant error source results from errors in knowledge of the aircraft attitude, the most important component of which is roll angle, which in our system translates directly to an error in look angle. Again differentiation yields

$$\sigma_h = \rho \sin \theta \sigma_\theta \quad (6)$$

Thus, good motion compensation is a prerequisite of any practical system.

TOPSAR design

Several TOPSAR system parameters are summarized in Table 1.

Table 1. TOPSAR radar system parameters

Parameter	TOPSAR value
Peak power, watts	1000
Pulse rate, Hz	600 nominal
Pulse length, μ sec	5.0
Antenna length, m	1.6
Antenna width, m	0.11
Antenna gain, dB	25
Range bandwidth, MHz	40
Receiver noise temperature, K	2100
Antenna baseline, m	2.58
Baseline angle (α), deg	62.77

Given the baseline separation and the signal to noise ratio we can then analyze performance of the interferometer. Figure 2 (Li and Goldstein [8], Zebker and Villasenor [7]) gives the expected phase error as

a function of signal to noise ratio and number of looks for a radar interferometer. Thus we may expect a phase error of 3.3° if the data are processed to 16 looks assuming an SNR of 13 dB, which implies a statistical error of 1.50 m in height precision. Knowledge of the roll angle is also needed for accurate data reduction. At present our system can correct for attitude errors to the 0.015° level, which (6) implies a height error of 1.9 m.

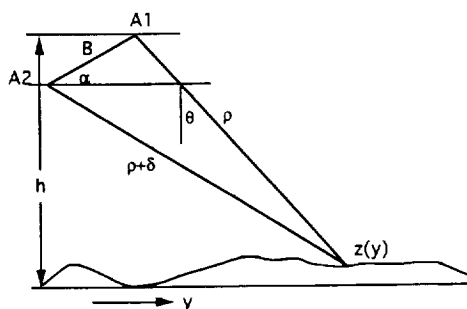
Figure 3 shows a set of data acquired over Fort Irwin in the Mojave Desert in California. The data shown represent ground coordinate rectified topographic maps in which the color contour interval is 6 m, thus one trip around the color wheel corresponds to 96 m for our 16 entry color table. The spatial resolution is 10 m. The accuracy of the map obtained over Ft. Irwin is described in the next section.

Verification procedure

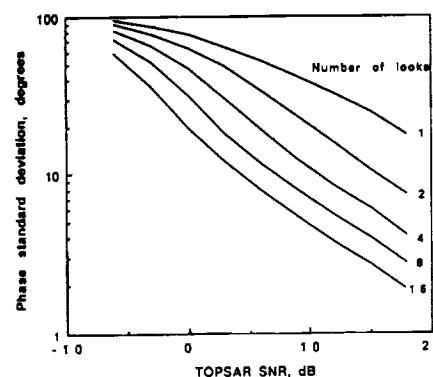
Verification of this mapping technique involves comparing the radar-derived height map with pre-existing high-resolution digital elevation models (DEMs) and characterizing the differences. Comparison was done on a data set from the Ft. Irwin area in California using the USGS 7.5' DEM with 30 m grid spacing and 7 m rms height error. Figures 4 shows a sample cut through the DEM and radar-generated terrain maps, and the difference between them is shown in the upper part of the figure. It is clear from examination of this figure that the error is dominated by differences in areas of high relief, and is caused both by errors in overall cross-track slope and by position errors.

References

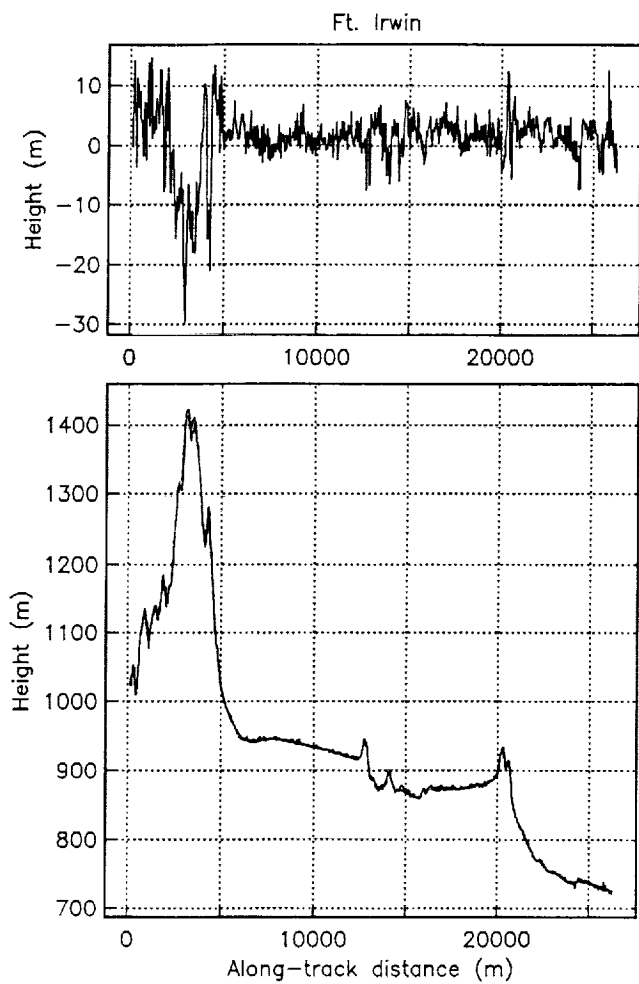
- [1] Graham, L.C., Synthetic interferometer radar for topographic mapping, Proc. IEEE, vol 62, 763-768, 1974.
- [2] Zebker, H. and R. Goldstein, Topographic Mapping from Interferometric SAR Observations. Journal of Geophysical Research v.91, No. B5, p. 4993-4999.1986.
- [3] Gabriel, A. K. and R. M. Goldstein, Crossed orbit interferometry: theory and experimental results from SIR-B, Int'l Journal Remote Sensing, vol 9., no. 8, pp. 857-872, 1988.
- [4] Goldstein, R. M., H. A. Zebker and C. Werner. Satellite radar interferometry: two-dimensional phase unwrapping, Radioscience, vol. 23, no. 4, pp 713-720, July-August 1988.
- [5] Gray, A. Laurence and P. J. Farris-Manning, Two-pass interferometry with airborne synthetic aperture radar, submitted to IEEE Trans. Geo. Rem. Sens., 1991.
- [6] Rodriguez, E. and J. Martin, Theory and design of interferometric SARs, submitted to Proceeding of the IEE, 1991.
- [7] Zebker, H.A. and J. Villasenor, Decorrelation in interferometric radar echoes, submitted to IEEE Trans. Geo, Rem. Sensing, August, 1991.
- [8] Li, F. and R. M. Goldstein, Studies of multi-baseline spaceborne interferometric synthetic aperture radars, IEEE Trans. Geo. Rem. Sens., vol. 28, no. 1, pp. 88-97, January 1990.



1. TOPSAR geometry. Radar echoes are transmitted from antenna A1 and received simultaneously at A1 and A2. The phase difference of the two echoes is proportional to the difference in path lengths δ , which depends on the baseline distance B, baseline angle α , range ρ , look angle θ , aircraft altitude h, and the height of the point $z(y)$.



2. Sensitivity of phase standard deviation to signal-to-noise ratio and number of looks in processor. Increasing number of looks is an effective means to reduce statistical variation, especially for the first 8 looks or so.



3. Topographic data acquired over Fort Irwin in the Mojave Desert in California. The data shown represent ground coordinate rectified topographic maps in which the color contour interval is 6 m.



4. DEM / radar map height difference from the Fort Irwin data.

EVALUATION OF THE TOPSAR PERFORMANCE BY USING PASSIVE AND ACTIVE CALIBRATORS

G. Alberti (*), A. Moccia (~), S. Ponte (~), and S. Velrella (*)

(*) CO.RI.S.T.A. Consortium
P.le Tecchio, 80, 80125 Napoli, Italy
(~) Faculty of Engineering, University of Naples
P.le Tecchio, 80, 80125 Napoli, Italy

This paper presents the preliminary analysis of the C-band cross-track interferometric data (XTI) acquired during the MAC Europe 1991 campaign over the Matera test site, in Southern Italy. 23 passive calibrators (Corner Reflector, CR) and 3 active calibrators (Active Radar Calibrator, ARC) were deployed over an area characterized by homogeneous background (Fig. 1). Contemporaneously to the flight, a ground truth data collection campaign was carried out (CO.RI.S.T.A. 1991).

The DC-8 NASA airplane was equipped with the JPL AIRSAR, which had been modified at the Ames Research Center to accommodate two C-band antennas designed and developed by the CO.RI.S.T.A. Consortium and to receive the two channels by using the existing hardware (TOPSAR, *Zebker et al.*, 1992).

The research activity has been focused on the development of motion compensation algorithms, in order to improve the height measurement accuracy of the TOPSAR system. Moreover, we intend to derive the system impulse response by comparing and integrating a theoretical model, the available ancillary data, and the CR's phase history.

In the following we present a status report of our research, which has been mainly devoted to compute a reference function for azimuth compression, that accounts for phase errors due to the airplane dynamics. In this work, after the characterization of the doppler histories of the CRs and the ARCs, we carry out a correlation between the attitude data and the phase of the range-compressed calibrators. Experimental results show a satisfactory correspondence between the airplane dynamics described in the ancillary data and the one reconstructed from the phase history of the calibrators (shown in Fig. 2). At this stage we are able to derive a range-dependent azimuth reference function which compensates also velocity and attitude perturbations. In order to validate this procedure, we perform an

image quality analysis for several calibrators, evaluating their one-dimensional 3dB resolutions, ISLR (Integrated Sidelobe Ratio), PSLR (Peak Sidelobe Ratio) and SCR (Signal-to-Clutter Ratio) (*JPL SIR-C Team et al.*, 1990), and consequently an estimate of their radar cross section. A preliminary comparison of numerical results with theoretical performance, ground truth and anechoic chamber data is encouraging, and allows a refinement of the azimuth filter.

Then, the raw data gathered by the two antennas are processed separately and combined to form an interferogram. The reconstructed airplane dynamics is also used to derive the baseline time variation, that is necessary for the 2π phase unwrapping procedure. To this end we have developed a computer code based on a two-dimensional algorithm which uses the calibrators as ground control points, both to solve the first 2π ambiguity and to overcome decorrelation problems when possible.

Finally, the computed terrain elevation is compared with the 1:25000 scale contour levels of the Italian Istituto Geografico Militare (IGM), in order to assess the height accuracy of the system and to evaluate the improvement consequent to a more sophisticated interferometric processing.

This work has been carried out under the sponsorship of the Italian Space Agency (ASI).

References:

CO.RI.S.T.A. Internal Document "Aquaterra Campaign 1991", 1991

Zebker, H. A., Madsen, S. M., Martin, J., Wheeler, K. B., Miller, T., Lou, Y., Vettorello, S., Cucci, A., Alberti, G., "The TOPSAR Interferometric Radar Topographic Mapping Instrument", accepted for publication on IEEE Transactions on Geoscience and Remote Sensing, 1992

JPL SIR-C Team, DLR NE-HF X-SAR Team, I-PAF X-SAR Team, "Data Products and Image Quality Specifications for the SIR-C/X-SAR Mission", JPL D-7193, March 1990

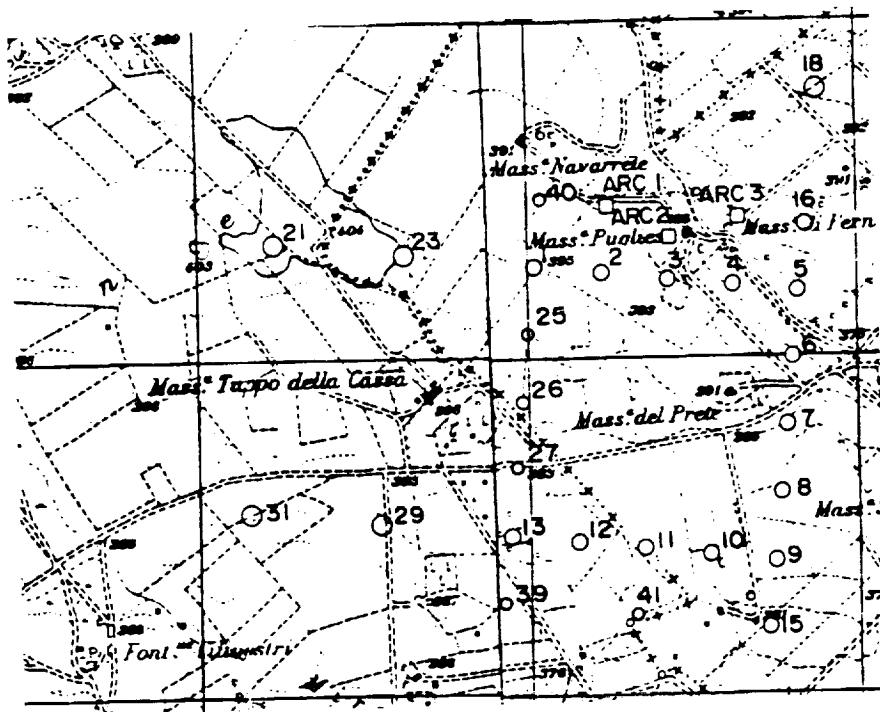


Fig. 1. Location of CRs and ARCs in the test site.

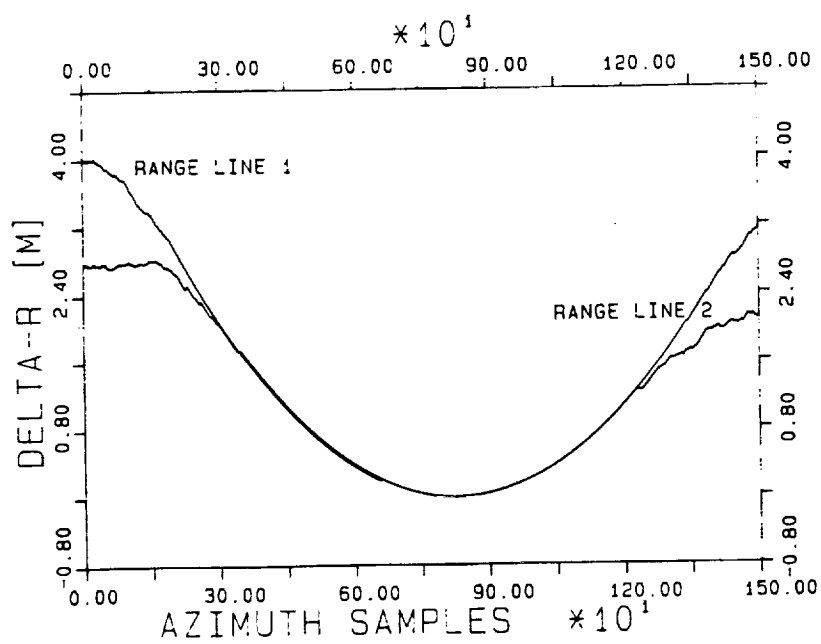


Fig. 2. Differences of the airplane-CR distance along two adjacent range bins in the range-compressed data.

FITTING A THREE-COMPONENT SCATTERING MODEL TO POLARIMETRIC SAR DATA

A. Freeman and S. Durden

Jet Propulsion Laboratory
M/S 300-235, 4800 Oak Grove Drive
Pasadena, CA 91109

1.0 INTRODUCTION

A major problem in analyzing polarimetric SAR data such as that produced by the NASA/JPL AIRSAR is in understanding the scattering mechanisms which give rise to features in the different polarization parameters. Researchers, on examining some polarimetric SAR data from their scene of interest for the first time, often notice unusual bright or dark features when displaying one of the many possible polarization representations of the data (e.g. total power, HH, VV or HV cross-section, HH-VV phase difference, HH-VV correlation coefficient, etc.) It is usually pertinent to ask what scattering mechanisms give rise to the unusual features?

Much excellent work has recently been done on modelling polarimetric radar backscatter for both naturally occurring terrain and man-made objects. These models are usually complex, and require a large number of input parameters to successfully predict the observed backscatter. For example, in modelling the backscatter return from a forest, measurements of tree heights and diameters, tree density, leaf size and angular distribution, branch size and angular distribution, trunk dielectric constants, ground roughness and dielectric constant are commonly required as inputs. All these models solve the 'forward problem', in predicting backscatter from a number of ground-based measurements of the imaged objects. It is difficult, if not impossible, to invert these models to provide a unique solution, simply because the number of input parameters (the 'ground truth') is often much larger than the number of output parameters (the radar measurements) in the forward problem.

In this paper, a new technique for fitting a three-component scattering mechanism model to the polarimetric SAR data itself, without utilising any ground truth measurements, is presented. The three scattering mechanism components included in the model are volume scatter from randomly oriented dipoles, first-order Bragg surface scatter and a dihedral scattering

mechanism for two surfaces with different dielectric constants. The model fit yields an estimate of the contribution to the total backscatter of each of the three components. The backscatter contributions can also be compared to give the relative percentage weight of each. The model fit has an equal number of input parameters (the polarimetric radar backscatter measurements) and output parameters (the backscatter contributions from each of the three components and two parameters describing them). The model can be applied to entire images or to small areas within an image to give a first-order estimate of the relevant scattering mechanisms. The model has been applied to many C-, L- and P-band AIRSAR images of different types of terrain. Results will be presented at the workshop.

2. THE MODEL

The model fit includes three very simple scattering mechanisms. First, for volume scattering, it is assumed that the radar return is from randomly oriented, very thin cylinder-like scatterers. By making several simplifying assumptions the second-order statistics of the resulting scattering matrix can be derived. After normalizing with respect to the VV cross section, these are:

$$\langle |S_{HH}|^2 \rangle = \langle |S_{VV}|^2 \rangle = 1, \langle S_{HH} S_{VV}^* \rangle = \langle |S_{HV}|^2 \rangle = 1/3 \quad (1)$$

The double-bounce scattering component is modelled by scattering from a dihedral corner reflector, where the reflector surfaces can be made of different dielectric materials, corresponding to a ground-trunk interaction for forests, for example. The vertical surface (e.g. the trunk) has Fresnel reflection coefficients R_{th} and R_{tv} for horizontal and vertical polarizations, respectively. The horizontal surface (the ground) has Fresnel reflection coefficients R_{gh} and R_{gv} . The scattering matrix for double-bounce scattering is then:

$$S = \begin{bmatrix} -R_{gv} R_{tv} & 0 \\ 0 & R_{gh} R_{th} \end{bmatrix} \quad (2)$$

The second-order statistics for double-bounce scattering, after normalization with respect to the VV term, are:

$$\langle |S_{HH}|^2 \rangle = |\alpha|^2, \langle |S_{VV}|^2 \rangle = 1, \langle S_{HH} S_{VV}^* \rangle = -\alpha, \langle |S_{HV}|^2 \rangle = 0$$

where $\alpha = R_{gh} R_{th} / R_{gv} R_{tv}$ (3)

For the surface scatter, a first-order Bragg model is used, with second order statistics (after normalization):

$$\langle |S_{HH}|^2 \rangle = |\beta|^2, \langle |S_{VV}|^2 \rangle = 1, \langle S_{HH} S_{VV}^* \rangle = \beta, \langle |S_{HV}|^2 \rangle = 0 \quad (4)$$

where β is real. For all of these backscatter components, it is assumed that the like- and cross-polarized returns are uncorrelated, and that the backscatter is reciprocal. Further, assuming that the volume, double-bounce and surface scatter components are uncorrelated, the total second order statistics are the sum of the above statistics for the individual mechanisms. Thus the model for the total backscatter is:

$$\begin{aligned}\langle |S_{HH}|^2 \rangle &= f_s |\beta|^2 + f_d |\beta|^2 + f_v \\ \langle |S_{VV}|^2 \rangle &= f_s + f_d + f_v \\ \langle S_{HH} S_{VV}^* \rangle &= f_s \beta - f_d \alpha + f_v/3 \\ \langle |S_{HV}|^2 \rangle &= f_v/3\end{aligned}\tag{5}$$

where f_s , f_d and f_v are the surface, double-bounce and volume scatter contributions to the VV cross section.

The above model gives four equations in five unknowns. A solution can only be found if one of the unknowns is fixed. Since neither the surface nor the double-bounce mechanism contribute to the HV term, this can be used to estimate the volume scatter contribution directly. This can then be subtracted off the three remaining terms, leaving three equations in four unknowns. The sign of the real part of the residual $S_{HH} S_{VV}^*$ term can then be used to decide whether double-bounce or surface scatter is dominant. If $\text{Re}(S_{HH} S_{VV}^*)$ is positive, then surface scatter is determined to be dominant, and α is set to 1. If $\text{Re}(S_{HH} S_{VV}^*)$ is negative, then double-bounce scatter is determined to be dominant, and β is set to 1. Then f_s , f_d , f_v and β or α can be estimated from the residual radar measurements.

3. SUMMARY

A new technique for fitting simple backscatter mechanisms to polarimetric SAR data has been presented. The model can be used to determine to first order what the dominant scattering mechanisms are which give rise to observed backscatter in polarimetric SAR data. Results of application of the model to AIRSAR images of different types of terrain will be presented at the workshop.

4. ACKNOWLEDGEMENT

The research described in this paper was carried out by the Jet Propulsion Laboratory, California Institute of Technology under a contract with the National Aeronautics and Space Administration.

APPLICATION OF SYMMETRY PROPERTIES TO POLARIMETRIC REMOTE SENSING WITH JPL AIRSAR DATA

S. V. Nghiem, S. H. Yueh, R. Kwok, and F. K. Li
Jet Propulsion Laboratory
California Institute of Technology
4800 Oak Grove Drive
Pasadena, California 91109

1. INTRODUCTION

Based on symmetry properties, polarimetric remote sensing of geophysical media is studied in this paper. From the viewpoint of symmetry groups, media with reflection, rotation, azimuthal, and central symmetries are considered. The symmetries impose relations among polarimetric scattering coefficients, which are valid to all scattering mechanisms in the symmetrical configurations. Various orientation distributions of non-spherical scatterers can be identified from the scattering coefficients by a comparison with the symmetry calculations. Experimental observations are then analyzed for many geophysical scenes acquired with the Jet Propulsion Laboratory (JPL) airborne polarimetric SAR at microwave frequencies over sea ice and vegetation. Polarimetric characteristics of different ice types are compared with symmetry behaviors. The polarimetric response of a tropical rain forest reveals characteristics close to the central symmetry properties, which can be used as a distributed target to relatively calibrate polarimetric radars without any deployment of man-made calibration targets.

2. SYMMETRY PROPERTIES

Relations among polarimetric backscattering coefficients have been derived (Nghiem *et al.* 1992) for both reciprocal and non-reciprocal geophysical media with reflection, rotation, azimuthal, and central symmetries. The corresponding symmetry groups can be constructed from three fundamental operations: mirror reflection, axial rotation, and linear translation (Hamermesh, 1972). The derivations are based on the invariance of the scattering coefficients under the symmetry transformations and applicable to all scattering mechanisms in the symmetrical configurations. These symmetries impose on the scattering coefficients a number of equations, which reduce the number of independent parameters in the covariance or Mueller matrix as summarized in Table 1. Central symmetry inherits azimuthal symmetry characteristics at all incident angles.

Table 1: Number of Independent Parameters in Covariance Matrix or Mueller Matrix

	Non-reciprocal	Reciprocal
No symmetry	16	9
Reflection Symmetry	8	5
Rotation Symmetry	6	3
Azimuthal Symmetry	3	2

3. ORIENTATION DISTRIBUTIONS

Non-spherical scatterers can take on needle-like shape or disc-like shape. The distribution of scatterer orientations is dependent on the scatterer species, environmental effects, and physiologic conditions. For species with no azimuthal preference such as leaves in trees, several distributions have been reported including spherical, uniform, planophile, plagiothile, erectophile, or extremophile distributions (*Goel and Strebel 1984*). Probability density functions of orientations are given in terms of inclination angles θ from 0 to 90°. These orientation distributions have certain symmetries which affect polarimetric scattering coefficients. In each case of the distributions, the ratio $\epsilon = \sigma_{hv}/\sigma_{hh}$ is calculated under independent scattering assumption from a theoretical model (*Tsang et al. 1985*) and then compared with the quantity $\epsilon_0 = (1 - |\rho|)/2$ as suggested by the central symmetry where ρ is the correlation coefficient between the hh and vv returns. For central symmetry, $\epsilon = \epsilon_0$ at arbitrary incident angles. Referred to this symmetry, the deviation of ϵ from ϵ_0 therefore indicates how the scatterers are structured. The results for the aforementioned orientation distributions show that, in general, ϵ/ϵ_0 is larger for more vertical orientation regardless of scatterer shape. For spherical distribution, $\epsilon/\epsilon_0 = 1$ manifests the central symmetry.

4. APPLICATIONS TO JPL SAR DATA

In this section, an analysis based on the symmetry is applied to JPL SAR data for sea ice and vegetation. Polarimetric SAR scenes of sea ice in the Beaufort sea were acquired during March 1988 in a series of NASA DC-8 airborne flights (*Cavaliere, 1988*). Weather and sea ice characteristic data were collected continuously during March at the Applied Physics Laboratory's drifting ice station (APLIS'88) located north-east of Prudhoe Bay, Alaska. Meteorological reports and ice measurements were recorded (*Wen et al. 1989*). Sea ice conditions consist of a transition from the extensive coastal first-year ice region to multi-year ice pack to the north. Air temperatures varied between -12° and -18° on March 11 and colder (below -25°) during an earlier period in March. First-year ice in the vicinity of the ice station was 1.5-m to 2.4-m thick and covered by a snow layer of 15.0-cm average depth. Multi-year ice was also covered by snow and hummocked up to 6.0-m height. Ice divergence occurring close to the period of data collection was experienced on March 10 when high ice drift velocities were recorded. Sea ice scenes on March 11 reveal images of new cracks and leads created by the divergent ice motion. Leads rapidly frozen under the cold condition became new thin ice formations. The results indicate that first-year ice signatures quite depart from central symmetry behavior as compared to multi-year ice. Structurally, first-year ice has a preferential vertical orientation of brine inclusions (*Weeks and Ackley 1982*) while scatterers in multi-year ice are more randomly distributed. Comparisons of the measured values for the polarimetric returns from sea ice with the symmetry calculations reveal the structural information which helps identify the ice types.

For vegetation, SAR scenes acquired over various forest types, including pine, mixed, and tropical rain forests, are considered. In the 1989 MAESTRO-1 Campaign, an experiment was conducted in Les Landes pine forest, south-west France, where the JPL SAR data were collected to relate SAR measurements and forest biophysical parameters (*Le Toan et al. 1991*). This scene consists of maritime pine trees at different ages from young to mature stages (more than 40 years). Also in June 1989, SAR images were obtained for Mt. Shasta in northern California. Forest areas in Mt. Shasta are dominated by ponderosa pine and white fir species

(Zebker *et al.* 1991). In Belize, a tropical rain forest was imaged. The forest in this scene has dense canopy and understory with various tropical species. At C-band frequency, the relation $\epsilon = \epsilon_0$, small phase of ρ , and the balance between hh and vv returns are well satisfied at all incident angle, especially for the Belize forest. This can be explained based on the symmetry properties. Azimuthal symmetry is often observed on leaves' orientation in forest canopies. For elevation orientations of vegetation elements, the distributions have been discussed in the last section. Foliage composed of leaves with spherical orientation distribution has central symmetry which requires the polarimetric scattering coefficients to satisfy $\epsilon = \epsilon_0$, $\text{Im } \rho = 0$, and $\gamma = \sigma_{vv}/\sigma_{hh} = 1$ at arbitrary incident angles. These relations are the direct consequence of the central symmetry due to the random orientation of leaves (spherical distribution). When the frequency is low such that the electromagnetic wave can penetrate through the foliage canopy, the central symmetry can be destroyed due to the horizontal branches or other structures of tree elements. From natural distributed targets, reflection together with central symmetries will allow the full relative calibration, including the cross talk and the channel imbalance, to all incident angles without the deployment of man-made calibration targets.

ACKNOWLEDGMENTS

The research described in this paper was carried out by the Jet Propulsion Laboratory, California Institute of Technology, under a contract with the National Aeronautics and Space Administration.

REFERENCES

- Cavalieri, D. J., "NASA Sea Ice and Snow Validation Program for the DMSP SSM/I: NASA DC-8 Flight Report," *NASA Tech. Memo.*, 100706, 1988.
- Goel, N. S., and D. E. Strebel, "Simple Beta Distribution Representation of Leaf Orientation in Vegetation Canopy," *Agronomy Journal*, 76, 800-802, 1984.
- Hamermesh, M., *Group Theory and its Application to Physical Problems*. Addison-Wesley, Reading, Massachusetts, 1972.
- Le Toan, T., A. Beaudoin, J. Riom, and D. Guyon, "Relating Forest Parameters to SAR Data," *Proceedings of IGARSS'91*, II. Helsinki University of Finland, Espoo, Finland, 689-692, 1991.
- Nghiem, S. V., S. H. Yueh, R. Kwok, and F. K. Li, "Symmetry Properties in Polarimetric Remote Sensing," submitted to *Radio Science*, February 1992.
- Tsang, L., J. A. Kong, and R. T. Shin, *Theory of Microwave Remote Sensing*, John Wiley & Sons, New-York, 1985.
- Weeks, W. F., and S. F. Ackley, *The Growth, Structure, and Properties of Sea Ice*, US Army Corps of Engineers, Cold Regions Research and Engineering Laboratory, Monograph 82-1, 1982.
- Zebker, H. A., J. J. van Zyl, S. L. Durden, and L. Norikane, "Calibrated Imaging Radar Polarimetry: Technique, Examples, and Applications," *IEEE Trans. Geosci. Remote Sensing*, 29, 6, 942-961, 1991.

EXTERNAL CALIBRATION OF POLARIMETRIC RADAR IMAGES USING DISTRIBUTED TARGETS

Simon H. Yueh, S. V. Nghiem, and R. Kwok

Jet Propulsion Laboratory
California Institute of Technology
4800 Oak Grove Drive
Pasadena, CA 91109

1. INTRODUCTION

A new technique is presented in this paper for calibrating polarimetric synthetic aperture radar (SAR) images using only the responses from natural distributed targets. The model for polarimetric radars is assumed to be (Yueh et al., 1990)

$$X = cRST \quad (1)$$

where X is the measured scattering matrix corresponding to the target scattering matrix S distorted by the system matrices T and R (in general $T \neq R^t$). To allow for the polarimetric calibration using only distributed targets and corner reflectors, van Zyl (1990) assumed a reciprocal polarimetric radar model with $T = R^t$; when applied for JPL SAR data, a heuristic symmetrization procedure is used by POLCAL to compensate the phase difference between the measured HV and VH responses and then take the average of both. This heuristic approach causes some non-removable cross-polarization responses for corner reflectors, which can be avoided by a rigorous symmetrization method based on reciprocity (Yueh et al., 1991). After the radar is made reciprocal, a new algorithm based on the responses from distributed targets with reflection symmetry is developed to estimate the cross-talk parameters (Yueh et al., 1992). The new algorithm never experiences problems in convergence and is also found to converge faster than the existing routines implemented for POLCAL. When the new technique is implemented for the JPL polarimetric data, symmetrization and cross-talk removal are performed on a line-by-line (azimuth) basis. After the cross-talks are removed from the entire image, phase and amplitude calibrations are carried out by selecting distributed targets either with azimuthal symmetry along the looking direction or with some well-known volume and surface scattering mechanisms to estimate the relative phases and amplitude responses of the horizontal and vertical channels.

2. APPLICATIONS TO SAR DATA

After this new technique is applied to the L-band polarimetric data collected over the Mt. Shasta area in 1989, the responses of corner reflectors were extracted after each step to assess the effectiveness of the methods. Tables 1 and 2 show the covariance matrix parameters of the corner reflectors after cross-talk removal. The data presented in Table 1 are symmetrized by the POLCAL's approach before cross-talks are removed, whereas the data shown in Table 2 are symmetrized based on reciprocity. Comparing Tables 1 and 2 for both e and γ indicates that the new technique yields superior performance. Note that the same algorithm for cross-talk removal is applied for both cases; therefore the difference

is caused by the symmetrization procedure alone.

Trihedral	e	γ	ρ	β	ξ
CR1	-16.78	-1.34	0.997 \angle 31.6	0.92 \angle 145	0.95 \angle - 113
CR2	-21.46	-0.97	0.995 \angle 29.9	1.04 \angle 144	1.05 \angle - 115
CR3	-24.79	-1.67	0.991 \angle 31.9	0.96 \angle 114	0.98 \angle - 86
CR4	-16.04	-1.2	0.958 \angle 35.5	0.97 \angle 133	1.02 \angle - 96
CR5	-20.27	-2.41	0.983 \angle 30.3	1.02 \angle 127	1.04 \angle - 99
CR6	-13.59	-3.01	0.985 \angle 22.1	1.01 \angle 126	1.00 \angle - 101
CR7	-13.44	-1.68	0.99 \angle 22.1	0.99 \angle 124	1.02 \angle - 102
CR8	-19.64	2.40	1.00 \angle 10.9	0.85 \angle - 31.5	0.86 \angle 40.6

Table 1. Covariance parameters of trihedral reflectors after symmetrization (POL-CAL) and cross-talk removal. $e = |HV|/|HH|$, $\gamma = |VV|/|HH|$, ρ : correlation of HH and VV , β : correlation of HH and HV , and ξ : correlation of HV and VV . e and γ are in dB. The phases of ρ , β , and ξ are in degrees.

Trihedral	e	γ	ρ	β	ξ
CR1	-24.0	0.07	0.994 \angle 80.6	0.76 \angle 176	0.79 \angle - 100
CR2	-100	0.00	0.991 \angle 81.6	-	-
CR3	-100	-0.96	0.984 \angle 83.8	-	-
CR4	-24.07	-0.07	0.969 \angle 84.6	1.01 \angle 137	1.15 \angle - 42
CR5	-100	-1.38	0.992 \angle 81.2	-	-
CR6	-100	-0.34	0.992 \angle 69.6	-	-
CR7	-100	0.21	0.998 \angle 68.7	-	-
CR8	-100	0.48	0.991 \angle 64.0	-	-

Table 2. Covariance parameters of trihedral reflectors after symmetrization and cross-talk removal based on the new technique.

For the phase calibration, we determined the relative phase errors between H and V channels for nine arbitrarily selected areas in the image, and linearly fit the phase correction factors along the range. Each azimuthal line is then calibrated by the interpolated phase factor. The resulting responses of corner reflectors are shown in Table 3. Comparing the phases of ρ between Tables 2 and

3, we can see that the relative phase errors between HH and VV are greatly reduced.

From the γ of the corner reflectors, it seems that the amplitudes of H and V channels are well balanced for L-band. Thus, additional correction on channel imbalance does not seem to be necessary.

ACKNOWLEDGMENTS

The research described in this paper was carried out by the Jet Propulsion Laboratory, California Institute of Technology, under a contract with the National Aeronautics and Space Administration.

REFERENCES

Yueh, S. H., J. A. Kong, and R. T. Shin, "Calibration of Polarimetric Radars Using In-Scene Reflectors," *Progress In Electromagnetics Research*, Elsevier, New York, Vol. 3, Chapter 9, 1990.

van Zyl, J. J., "Calibration of Polarimetric Radar Images Using Only Image Parameters and Trihedral Corner Reflectors Responses," *IEEE Trans. Geoscience and Remote Sensing*, Vol. 28, No. 3, 337-348, 1990.

Yueh, S. H., J. A. Kong, and R. T. Shin, "External Calibration of Polarimetric Radars Using Point and Distributed Targets," Proc. of the Third AIRSAR Workshop, 1991.

Yueh, S. H., S. V. Nghiem, and R. Kwok, "External Calibration of Polarimetric Radars Using Distributed Targets," submitted for publication in *IEEE Trans. Geoscience and Remote Sensing*, 1992.

Trihedral	e	γ	ρ	β	ξ
CR1	-24.0	0.07	$0.994\angle - 8.7$	$0.76\angle 131$	$0.79\angle - 145$
CR2	-100	0.00	$0.991\angle - 8.2$	-	-
CR3	-100	-0.96	$0.984\angle - 6.5$	-	-
CR4	-24.07	-0.07	$0.969\angle - 3.3$	$1.01\angle 94$	$1.15\angle - 86$
CR5	-100	-1.38	$0.992\angle - 7.0$	-	-
CR6	-100	-0.34	$0.992\angle - 10.5$	-	-
CR7	-100	0.21	$0.998\angle - 11.8$	-	-
CR8	-100	0.48	$0.991\angle - 16.7$	-	-

Table 3. Covariance parameters of trihedral reflectors after symmetrization, cross-talk removal, and phase calibration based on the new technique.

PROCESSING OF POLARIMETRIC SAR DATA FOR SOIL MOISTURE ESTIMATION OVER MAHANTANGO WATERSHED AREA

K.S. Rao, W.L. Teng and J.R. Wang
Goddard Space Flight Center, Greenbelt, MD. 20771

1. INTRODUCTION

Microwave remote sensing technique has a high potential for measuring soil moisture due to the large contrast in dielectric constant of dry and wet soils (Ulaby et al. 1982). Recent work by Pults et al. (1990) demonstrated the use of X/C-band data for quantitative surface soil moisture extraction from airborne SAR system. Similar technique was adopted in this study using polarimetric SAR data acquired with the JPL-AIRSAR system over the Mahantango watershed area in central Pennsylvania during July 1990. The data sets reported here include C-, L- and P-bands of July 10, 13, 15 and 17, 1990.

2. RESULTS AND DISCUSSION

SAR data was calibrated and registered with digital elevation data using a second degree polynomial to study the possible effects of local topography on σ° averaged over a corn field (Rao et al. 1992). The results did not show any significant effect of local topography on σ° within a single scene for the type of terrain in the study area. Multiparameter least square regression analysis was used to fit the soil moisture data with multifrequency, multipolarization σ° data to identify the best frequency - polarization combinations for the accurate estimation of soil moisture. There were 4 corn fields in the study area for which surface soil moisture data (0-5 cm) were available for July 10, 13, 15 and 17. The plant water content of these fields varied from 1.9 to 2.2 kg/sq.m. Neglecting the differences in the vegetation parameters, σ° of the 4 corn fields was plotted as a function of soil moisture. It was observed that σ° was linearly related to soil moisture in accordance with Ulaby et al. (1981). However, the degree of nonlinearity is more for L-band than for C-band.

Table 1 gives the correlation coefficient (r), standard error of estimation of soil moisture (s) and slope for C-, L- and P-bands; HH, VV and HV

polarizations; both for linear and nonlinear fittings. It can be seen from Table 1 that C-band showed higher r compared to L-band, and P-band showed the least. The trends were similar for s values. L-band showed higher slope values compared with C-band, indicating the higher sensitivity of L-band to soil moisture. The lesser sensitivity of C-band can be understood due to its less penetration ability through vegetation. Nonlinear fitting considering a square term showed a marginal improvement in the results.

Multifrequency linear least square fit was attempted considering several combinations of frequencies and polarizations and the results are shown in Table 2. It can be seen from Table 2 that the combination which includes all polarizations and frequencies gave the best correlation coefficient ($r = 0.9$) and standard error of estimation ($s = 2.83$). However, other combinations are also reasonably good. For further investigations, the combination of L-, C-bands with HH, VV and HV polarizations was considered which showed $r = 0.89$ and $s = 2.94$.

It should be noted that, in all the above calculations, the same data were used for computing the coefficients as well as for estimating r and s . To check if the coefficients are useful for other data sets, we estimated the coefficients using the data sets of July 10, 13 and 15. These coefficients were then used with σ^0 of July 17 to estimate the soil moisture. Comparison with field measured soil moisture showed good agreement between estimated and measured soil moisture for July 17. To assess how best these coefficients can be used for other corn fields in the study area, we estimated soil moisture values for some other corn fields and observed that they were on the same order of magnitude as that of the field measured soil moisture for all 4 dates. There were no ground truth data available for these fields to directly verify the results. However, the meteorological station within the study area recorded 1.3, 5.0, 18.1, 18.5, 19.8 and 0.0 mm for the dates July 10, 11, 12, 13, 16 and 17. The estimated soil moisture was in accordance with the precipitation rates.

3. CONCLUSION

In spite of the presence of corn fields in the

study area, SAR data showed good correlation with soil moisture for L- and C-bands. A simple linear regression of multipolarization, multifrequency approach gave correlation coefficient of 0.9 and standard error of estimation of 2.83. The regression coefficients derived from the 4 corn fields with ground data were useful for estimating soil moisture levels of other corn fields in the study area for the same date as well as for other dates. One limitation of the current approach is that the regression analysis considered each frequency measurement as independent. Therefore, there is a need to develop a model which makes use of the inter-relationships among frequencies (in terms of penetration capability) and polarizations (in terms of geometry of vegetation) in such a way that the effects of vegetation can be accounted for automatically. Our ongoing research addresses this problem.

4. ACKNOWLEDGEMENTS

The authors are thankful to E.T. Engman, Head of Hydrological Sciences branch, GSFC for providing the AIRSAR and ground truth data. They also gratefully acknowledge N. Chauhan for his useful discussions. K.S. Rao is thankful to the National Research Council for providing a senior research associateship during the course of the work.

REFERENCES

- Pultz T.J, R.Leconte, R.J.Brown and B.Brisco, "Quantitative soil moisture extraction from airborne sar data," Canadian Journal of Remote Sensing, Vol 16, No. 3, pp 56-62, October 1990.
- Rao K.S, W.L.Teng and J.R.Wang, "Terrain effects on backscattering coefficients derived from multifrequency, polarimetric SAR data," Proceedings of IGARSS-92.
- Ulaby F.T, A.Aslam and M.C.Dobson, "Effects of vegetation cover on the radar sensitivity to soil moisture," Remote Sensing Technical Report 460-10, University of Kansas, Lawrence, Kansas, 1981.
- Ulaby F.T, R.K.Moore and A.K.Fung, Microwave Remote Sensing: Active and Passive, Vol II, Addison-wesley, Reading, M.A., 1982.

TABLE 1. RESULTS OF THE LINEAR AND NONLINEAR
REGRESSION ANALYAIS

DATA σ°	LINEAR REGRESSION			NONLINEAR REGRESSION	
	r	s	SLOPE	r	s
C-HH	0.75	4.23	0.17	0.77	4.10
C-VV	0.83	3.57	0.19	0.83	3.56
C-HV	0.79	3.96	0.13	0.79	3.95
L-HH	0.77	4.06	0.32	0.81	3.73
L-VV	0.61	5.09	0.40	0.76	4.16
L-HH	0.79	4.00	0.29	0.79	3.94
P-HH	0.19	6.30	0.16		
P-VV	0.20	6.29	0.15		
P-HV	0.09	6.69	-0.05		

TABLE 2. RESULTS OF LINEAR LEAST SQUARE FITTING
FOR SEVERAL COMBINATIONS OF FREQUENCY AND
POLARIZATION

S.NO	BAND	POLARIZATION	r	s
1	C	HH, VV, HV	0.84	3.51
2	L	"	0.85	3.33
3	P	"	0.31	6.11
4	C, L, P	HH	0.80	3.83
5	"	VV	0.84	3.44
6	"	HV	0.84	3.52
7	C, L	HH, VV, HV	0.89	2.94
8	C, P	"	0.86	3.27
9	L, P	"	0.87	3.16
10	C, L, P	"	0.90	2.83
11	C, L	HH, HV	0.86	3.22
12	C, P	"	0.82	3.68
13	L, P	"	0.86	3.26
14	C, L	HH, VV	0.85	3.33
15	C, P	"	0.86	3.30
16	L, P	"	0.84	3.48
17	C, L, P	HH, VV	0.87	3.15
18	"	HH, HV	0.87	3.17

EVALUATION OF POLARIMETRIC SAR PARAMETERS FOR SOIL MOISTURE RETRIEVAL

Jiancheng Shi

Center for Remote Sensing and Environmental Optics
University of California, Santa Barbara, CA 93106

Jakob J. van Zyl

NASA/JPL California Institute of Technology

Edwin T. Engman

NASA/GSFC Hydrological Sciences Branch

This paper reports on results of ongoing efforts to develop an algorithm for soil moisture retrieval from SAR imagery. Estimates of soil moisture are of great importance in numerous environmental studies, including hydrology, meteorology, and agriculture. Previous studies [1] using extensive scatterometer measurements have established the optimum parameters for moisture retrieval as C-band HH radar operating at incidence angles between 10° to 15° . However, these parameters have not been tested or verified with imaging radar systems. The results from different investigators have shown considerable variability in the relationship between soil moisture and radar backscattering. This variability suggests that those algorithms are site-specific. Furthermore, the small incidence angle requirement limits the spatial application, especially for airborne radar systems.

The imaging radar polarimeter permits measurement of the full polarization signature of every resolution element in an image. The radar polarization signature of an object permits a more accurate description of the object of interest than single-polarization measurements [2]. Thus, the solution for geometric shape and dielectric constant of an object is less ambiguous, making the development of a quantitative algorithm for soil moisture retrieval from Synthetic Aperture Radar (SAR) data possible. Our previous work [3] indicated that the ratio of the co-polarization signals, that is, the ratio of σ^{hh} to σ^{vv} , could be used for soil moisture retrieval at longer wavelengths (L-band) and at larger incidence angles ($> 40^\circ$). The algorithm to infer soil moisture from imaging radar data was based on a first-order surface scattering model. This model predicts that the co-polarization ratio is sensitive to soil moisture at large incidence angles but not to surface roughness. However, the polarization signal ratio measurements are sensitive to the radar system noise and the other scattering contributions such as the multi-surface and volume scattering even if these effects only contribute a small portion of the total signal in the measurements. These factors result in an under-estimation of soil moisture when the first-order surface scattering algorithm was applied to imaging radar data.

To address these problems, JPL AIRSAR data, in May 1988 and in September 1989 acquired over an agricultural area near Fresno, California, were used to test the algorithm. We evaluated the effects of the radar system noise, the multi-surface scattering [4] and the volume scattering from soil [5] on the co-polarization ratio measurements.

Assuming the noise power to be the same in all channels, the effect of system noise on the ratio measurement of σ^{vv}/σ^{hh} can be expressed as

$$\frac{\sigma^{vv} + \text{noise}}{\sigma^{hh} + \text{noise}} \geq \frac{\sigma^{vv}}{\sigma^{hh}} \quad (1)$$

for all values under the condition of $\sigma^{hh} < \sigma^{vv}$. This results in an under-estimation of the soil moisture especially at larger incidence angle range because the signal to

noise ratio typically decreases as incidence angle increases. Based on the assumption that the noise power in the two co-polarized channels is typically of the same magnitude, the amount of noise in all channels can be estimated. This estimated noise can be then used to adjust the observed measurement before inferring soil moisture. We will show the principle and comparison of the estimated with the measured system noise power.

The surface scattering models assume that the scattering medium is a homogeneous dielectric half-space. In practice, natural soil is not a perfectly homogeneous dielectric medium. Instead, it is a mixture of soil particles, air pockets, and liquid water. This results in dielectric discontinuities inside the soil. Because soil is a densely packed medium, the effects of these discontinuities will be reduced for longer wavelengths, especially when the distance between scatterers is much smaller than the wavelength. The result is that the volume scattering of soil contributes only a small portion of the observed signals at longer wavelengths and that the dominant scattering source is the surface backscattering at the air-soil interface. In evaluating the magnitude of each co-polarization signal, the surface scattering can be used to explain the general relations between the backscattering measurements and soil physical properties. However, in attempting to relate the polarization ratio or difference to the physical properties of soils, the volume scattering contribution becomes significant even if it only contributes a small portion in the observed backscattering returns. This effect is also expected when using long-wavelength sensors because of deeper penetration. To overcome the volume scattering effect on estimation of soil moisture, we have developed an algorithm which is based on the first-order scattering model considering both the surface and volume scattering contributions [5].

Figure (A) shows an image of the inferred soil moisture map of the study sites from L-band SAR data. This map was produced using an first-order surface scattering model only. The soil moisture map shown in (B) was derived by the algorithm which includes both surface and volume scattering of soil. The black regions are vegetation covered fields. When applying the first-order surface scattering algorithm, only about 20 to 30 percent pixels were within the possible physical conditions predicted by the first-order surface scattering model. As shown in Figure (A), there are many pixels with missing values even after post-processing. It is especially evident at large incidence angles. However, applying the algorithm with both surface and volume scattering considerations, about 80 percent of the pixels were within the physical limits. During the SAR flights, the volumetric soil moisture for the sampled dry fields varied between 3 and 10 percent. Most bare fields were dry because none of them had been irrigated for at least several weeks. The inferred soil moisture from SAR data agrees well with the field measurements and value ranges from 2 to 14 percent were inferred.

To evaluate the polarimetric SAR parameters for retrieval of bare soil moisture, we examined (1) the applicability of the first-order surface scattering model through the measurements of the depolarization factor at P-, L-, and C-band from bare fields, and (2) all ratios of the co-polarized signals and their linear combinations through the model predictions.

The measurements of the depolarization factor at C-band indicate a significant multi-scattering involved in the C-band measurements, but not at L- and P-band. When the surface is relatively rough, the higher-order surface scattering decreases the difference between the co-polarization signals. This also causes an underestimation of the soil moisture if we apply the first-order inversion algorithm. When second-order terms are added in the scattering calculations [2], the co-polarization ratio measurements become sensitive to roughness differences, but this sensitivity is reduced at larger incidence angles and for smoother surfaces.

First-order surface backscattering models predict that the ratio of the backscat-

tering coefficients of the co-polarizations is sensitive to soil moisture and insensitive to surface roughness. Similarly, the ratios of the linear combinations from the co-polarized returns have the same properties. The task is to select the measurements which maximize the sensitivity to soil moisture. Through the model simulations, we found that in all possible co-polarization ratios, σ^{vv}/σ^{hh} and $\sigma^{hh}/(\sigma^{vv} - \sigma^{hh})$ provide the greatest sensitivity to soil moisture at larger incidence angles.

As discussed above, the polarimetric SAR parameters for retrieval of bare soil moisture are likely to be L-band, the co-polarization ratios of σ^{vv}/σ^{hh} and $\sigma^{hh}/(\sigma^{vv} - \sigma^{hh})$, and incidence angles above 40° .

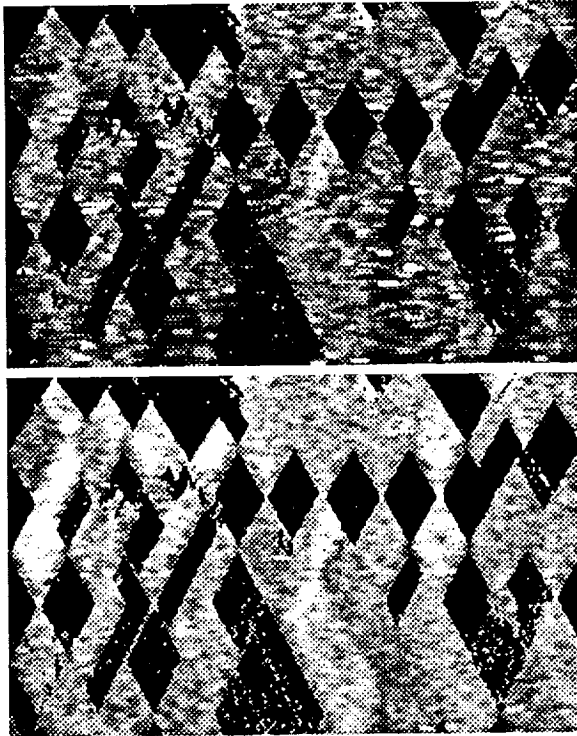


Figure. Comparison of inferred soil moisture map by using the first-order surface scattering model at top in (A), and by the algorithm which includes both surface and volume scattering at bottom in (B). The image brightness is proportional to soil moisture ranging from 2 to 14 percent by volume.

References

- [1] F. T. Ulaby and P. P. Batlivala. "Optimum radar parameters for mapping soil moisture," *IEEE Trans. on Geosci. Electron.*, vol GE-14, no. 2, pp 81-93, 1976.
- [2] J. J. van Zyl, H. A. Zebker, and C. Elachi. "Imaging radar polarization signatures: Theory and observation," *Radio Science* vol. 22, no. 4, pp. 529-543, 1987.
- [3] J. Shi, J. V. Soares, L. Hess, E. T. Engman, and J. J. van Zyl. "SAR-derived soil moisture measurements for bare fields," *Proceedings IGARSS '91*, vol. I, IEEE No. 91CH2971-0, pp. 393-396, 1991
- [4] J. J. van Zyl, J. V. Soares, J. Shi, and E. T. Engman. "Inference of soil moisture from imaging radar data," submitted to *Microwave-Signature 92*.
- [5] J. Shi, J. J. van Zyl, and E. T. Engman. "Development of soil moisture retrieval algorithm for L-band SAR measurements," submitted to *Proceedings IGARSS '92*.

Interaction Types and Their Like-Polarization Phase-Angle Difference Signatures

Jack F. Paris

GeoInformation Processing Systems
California State University, Fresno
Fresno, California 93740-0073

1. Introduction

The JPL Airborne SAR (AIRSAR) measures the full polarimetric properties of scene objects. AIRSAR data contain a complete set of *magnitudes* {for all linearly-polarized combinations [viz., VV, HH, and CS (cross polarization)]} and *phase-angle differences* (for all pairs of linearly-polarized components) for each image pixel. Radar image users have been greatly interested in the like-polarization (LK) phase-angle difference parameter, $\Delta\phi_{LK}$. Usually, it is associated with the *type* of interaction between microwaves and scene-object scattering-elements. One value of $\Delta\phi_{LK}$ is said to be produced by a dominant single scattering (or reflection) event, and another value is said to be the result of a dominant double-scattering (or double reflection) event. These are often called "single bounce" and "double bounce" interaction signatures, respectively. There appears to be a significant amount of confusion about how the interaction processes produce the characteristic values of $\Delta\phi_{LK}$ and about what value of $\Delta\phi_{LK}$ should be associated with each specific type. This paper attempts to address this issue.

2. Polarized Reflection Coefficients for a Smooth Interface

Most electromagnetic (EM) wave theory references present equations for calculating the (electric-field) reflection coefficients, ρ_H and ρ_V , of a smooth interface between two media, where ρ_H is for the case of the electric-field vector oscillating in the direction *normal to the plane of incidence* [viz., the TE or horizontal polarization (H) case], and ρ_V is for the case of the electric-field vector oscillating *within the plane of incidence* [viz., the TM or vertical polarization (V) case]. It is important to note that ρ is a complex number which relates the magnitude and phase of the electric field of the reflected wave to the magnitude and phase of the electric field of the incident wave *near the interface*.

There are many ways to express the ρ equations. One set is as follows:

$$\rho_H = \frac{n_1 \cos \theta_1 - n_2 \cos \theta_2}{n_1 \cos \theta_1 + n_2 \cos \theta_2} \quad \text{and} \quad \rho_V = \frac{n_1 \cos \theta_2 - n_2 \cos \theta_1}{n_1 \cos \theta_2 + n_2 \cos \theta_1} \quad (1a, 1b)$$

where n_1 is the complex index of refraction for Medium 1, n_2 is the complex index of refraction for Medium 2, θ_1 is the incidence angle in Medium 1, and θ_2 is the refraction

angle in Medium 2. The reader may notice that Eq. (1b) has the *opposite sign* to expressions for ρ_V given in some reference materials. In other words, the numerator terms in Eq. (1b) are sometimes reversed in standard references.

It is important to understand the reason for the sign discrepancy in expressions for ρ_V . Interestingly, a sign discrepancy never occurs in expressions for ρ_H . The genesis of the error is the way in which the reflection problem is posed. For the H case, the incident and reflected electric fields are both parallel to the interface and are, therefore, parallel to each other. Thus, phase-angle comparisons are easy to make for this case. For the V case, however, the incident and reflected electric fields are, in general, not parallel to each other (see Fig. 1b). Since phase-angle comparisons between oscillating electric fields must be made for parallel components, one has to choose which set of components to use for the V case. For this case, one set of electric field components is perpendicular to the interface, and the other set is parallel to the interface. **When the perpendicular components of the incident and reflected waves are chosen, the derived expression for ρ_V has a sign error. When the components parallel to the interface are chosen, the sign for ρ_V is correct.** This simple error has led to the confusion referenced above.

3. The Single-Bounce Case

The correctness of Eq. (1b) is easily verified by considering the case where $\theta_1 = \theta_2 = 0$ (i.e., the case of *normal incidence*). This is the case for a *single-bounce interaction* that can produce significant “backscattering” to a SAR imaging system. In this case, both ρ_H and ρ_V are equal to $[(n_1 - n_2) / (n_1 + n_2)]$. If the sign of Eq. (1b) were reversed, the expected equality of reflection coefficients for normal incidence fails to occur. Also, note that both reflection coefficients are always *negative* for the usual case where $n_2 > n_1$. **An important implication of the above is that the phase angles of the electric fields for both polarizations change by 180 degrees due to normal (single-bounce) reflection from a denser medium.** If Medium 1 and/or Medium 2 are lossy (i.e., have significant imaginary parts), then the phase angle shift will differ somewhat from 180 degrees. Nevertheless, for normal incidence, ρ_H and ρ_V are the same, and $\Delta\phi_{LK}$ equals 0.

Since a double-bounce interaction appears to be simply two single-bounce interactions, one after the other, one might believe that $\Delta\phi_{LK}$ will still be zero for this type of interaction. This is not the case. AIRSAR data analysts often observe values of $\Delta\phi_{LK}$ for double-bounce objects that are 180 degrees away from the values of $\Delta\phi_{LK}$ for single-bounce objects. The solution to this perplexing inconsistency is given in the next section of this paper.

4. The Double-Bounce Case

Consider the double-bounce case for H polarization in Fig. 1a. Due to the reflection from Interface A, the H wave undergoes a reversal of phase. For the usual case of $n_2 > n_1$, $(n_2 \cos \theta_2)$ is always greater than $(n_1 \cos \theta_1)$. Thus, the phase of the reflected H wave

will always be reversed by the reflection. Another phase reversal occurs in the H wave as the result of the second reflection from Interface B. Thus, the phase-angle difference between the incident wave and the corner-reflected "backscattering" wave will be near zero (depending on the material complex indices of refraction for the media on both sides of the two interfaces involved). The V wave (see Fig. 1b) undergoes similar changes in phase during each of the two reflections; however, one must be careful to apply the phase reversals to the electric field components of the V wave which are parallel to the two interfaces involved. When this is done, one sees that the corner-reflected "backscattered" wave will be approximately 180 degrees out of phase with the incident wave. Therefore, the difference in the phase-angles of the H wave and the V wave, $\Delta\phi_{LK}$, will be about 180 degrees for this double-bounce interaction. Thus, it is the geometry of the corner reflection itself, that "turns" the direction of the electric field for V-polarization without a corresponding "turning" the H polarization, which causes the unique like-polarization phase-angle difference signature of double-bounce dominated scene objects [e.g., wetlands and some forests and woodlands (with a smooth, wet substrate)]. An exception will occur when any local angle of incidence exceeds the Brewster angle on either interface. This (Brewster condition) happens when $(n_1 \cos \theta_2)$ is greater than $(n_2 \cos \theta_1)$. In this case, the phase shift of the V wave is affected, and $\Delta\phi_{LK}$ reverts to near zero. For angles near the Brewster condition, the magnitude of the V component also drops towards zero; therefore, the use of phase-angle differences for near the Brewster condition is ill advised. Other propagation phenomena also affect $\Delta\phi_{LK}$. For example, birefringent media for some volume-scattering situations (e.g., a corn crop with highly-oriented vertical stalks) will also alter $\Delta\phi_{LK}$ through the effects of differential speeds of propagation with polarization. Since single-scattering interactions affect more pixels than other interactions, one may calibrate $\Delta\phi_{LK}$ by noting the mode of its distribution.

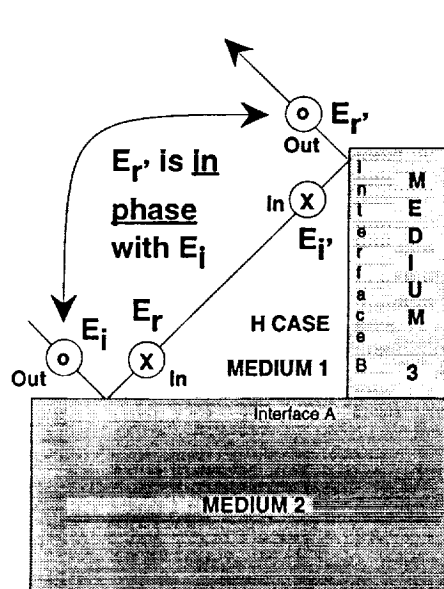


Figure 1A. Horizontal Polarization.

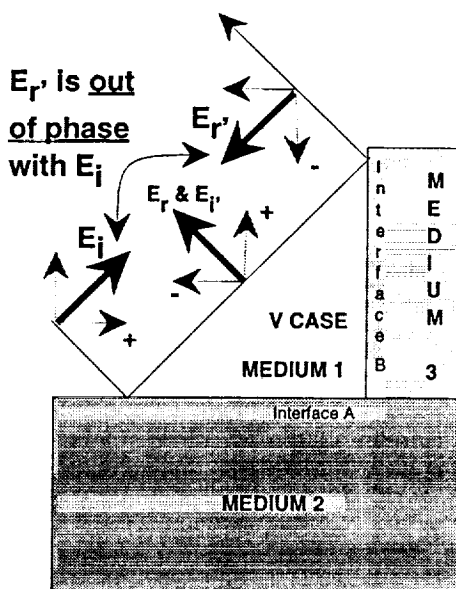


Figure 1B. Vertical Polarization.

APPLICATION OF MODIFIED VICAR/IBIS GIS TO ANALYSIS OF JULY 1991 FLEVOLAND AIRSAR DATA

L. Norikane, Broek, B.*, and Freeman, A.

Jet Propulsion Laboratory
California Institute of Technology
4800 Oak Grove Drive
Pasadena, CA 91109

*TNO-FEL
250g JG Den Haag
The Netherlands

1. INTRODUCTION

Three overflights of the Flevoland calibration /agricultural site were made by the JPL AIRSAR on July 3, July 12, and July 28, 1991 as part of MAC-Europe '92. A polygon map was generated at TNO-FEL which overlayed the slant range projected July 3 data set. Each polygon was identified by a sequence of points and a crop label. The polygon map was composed of 452 uniquely identified polygons and 15 different crop types.

Analysis of the data was done using our modified VICAR/IBIS GIS [1]. This GIS is an extension of the VICAR/IBIS GIS first developed by Bryant [2] in the 1970's which is itself an extension of the VICAR (Video Image Communication and Retrieval) image processing system also developed at JPL [3].

The VICAR/IBIS GIS requires that all images be coregistered to a georeference image. The georeference image must contain uniquely identified polygons representing homogeneous areas such as counties or vegetation stands. After conversion to a ground range projection, the Flevoland polygon map was ideally suited for use as the required georeference image.

To integrate the AIRSAR data into the VICAR/IBIS GIS, we generated 5 VICAR-labeled ground range projected images for each frequency and each data set (or overflight). The image set consisted of HH, HV, VV, HHVV* phase, and HHVV* amplitude images. For each image, we also generated an "info" file which contained a table of conversions from pixel value to "actual" value such as radar backscatter or radians.

The images from July 12 and July 28 were coregistered to the July 3 images using a two step process: image rotation/scaling and image warping. Both steps use tiepoints which are selected by hand.

Once all images had been coregistered, the following statistics were calculated for each polygon, frequency, and data set: average HH, HV, and VV backscatter, average HHVV* phase and amplitude, correlation coefficient using the averaged statistics, odd-bounce, double-bounce, and volume scattering percentage contributions [4], and average incidence angle (per data set only). These data were stored in columns of the georeference info file.

For each data set, selected columns in the info file were written into a text file which served as input to a Bayes classifier [5]. Depending on the features selected, the classifier identified each polygon with a high degree of accuracy.

2. PRELIMINARY RESULTS

We attempted to classify each polygon into 1 of 9 classes. (6 of the original 15 classes were eliminated due to insufficient numbers of representative polygons.) To do this we used a Bayes classifier and assumed Gaussian distributions.

Different combinations of features from the July 3 and July 28 data sets were used to classify the polygons with varying degrees of success.

Figure 1 shows the results from using only C-band HH, HV, VV, HHVV* phase, and correlation coefficients from both data sets. Using only these features yielded good classification results (i.e. no polygon was misclassified more than 25% of the time).

Features used:

July 3 / C-Band HH, HV, VV, HHVV* phase, correlation coefficient
 July 28 / C-Band HH, HV, VV, HHVV* phase, correlation coefficient

Actual Percent Classified As...

Crop Type	RAP	GRA	POT	WHE	SBT	COR	BAR	BEA	FRU
RAP	100	0.0	0.0	0.0	0.0	0.0	0.0	0.0	0.0
GRA	0.0	87.5	4.2	2.1	4.2	2.1	0.0	0.0	0.0
POT	0.0	1.0	96.1	0.0	1.9	1.0	0.0	0.0	0.0
WHE	0.0	4.3	0.0	91.5	4.3	0.0	0.0	0.0	0.0
SBT	0.0	3.8	0.0	0.0	96.3	0.0	0.0	0.0	0.0
COR	0.0	6.3	6.3	0.0	12.5	75.0	0.0	0.0	0.0
BAR	0.0	0.0	0.0	0.0	0.0	0.0	100	0.0	0.0
BEA	0.0	0.0	0.0	0.0	0.0	0.0	0.0	100	0.0
FRU	0.0	0.0	0.0	0.0	6.3	0.0	0.0	0.0	93.8

[RAP = rapeseed, GRA = grass, POT = potatoes, WHE = wheat, SBT = sugarbeet, COR = corn, BAR = barley, BEA = beans, FRU = fruit]

FIGURE 1

Other combinations of features have been tried. Results will be presented at the workshop.

From our analysis thus far, it is clear that there are more features available for classification than are truly needed. Additional work needs to be done in order to assess which features are highly correlated and thus not necessary for classification.

3. SUMMARY

We have successfully integrated the three 1991 Flevoland calibration/agricultural site AIRSAR overflight data sets in our modified VICAR/IBIS GIS. The images were successfully coregistered to a georeference image generated from a polygon map which overlaid the July 3 data set. Statistics and other information were accumulated and saved in the georeference info file. Selected columns from the info file were used as features in a Bayes classifier assuming Gaussian distributions. Using these features polygons were correctly classified at least 75% of the time in the example shown. Additional work needs to be done to assess which features are highly correlated and thus not necessary for classification.

4. ACKNOWLEDGEMENTS

Part of this work was carried out under contract with the National Aeronautics and Space Administration at the Jet Propulsion Laboratory, California Institute of Technology under NASA's Applied Information Systems Program.

5. REFERENCES

- [1] Norikane, L. et. al., 1992, A System for Verifying Models and Classification Maps by Extraction of Information from a Variety of Data Sources, International Geoscience and Remote Sensing Symposium (IGARSS) 1992 Proceedings.
- [2] Bryant, Nevin A., and A. L. Zobrist, 1976, IBIS: A geographic information system based on digital image processing and raster datatype: Symposium on Machine Processing of Remotely Sensed Data, Purdue University.
- [3] LaVole, Susan, et. al., 1989, VICAR User's Guide, Jet Propulsion Laboratory Internal Document D-4186 Rev A.
- [4] Freeman, A. and Durden, S., 1992, Fitting a Three-Component Scattering Model to Polarimetric SAR Data, AIRSAR Workshop '92
- [5] Duda, R. and Hart, P., 1973, Pattern Classification and Scene Analysis, Chapter 2, John Wiley & Sons, Inc.

RADAR ANALYSIS AND VISUALIZATION ENVIRONMENT (RAVEN): SOFTWARE FOR POLARIMETRIC RADAR ANALYSIS

K. S. Kierein-Young ^{1,2}, A. B. Lefkoff ¹, and F. A. Kruse ^{1,2}

¹ Center for the Study of Earth from Space (CSES)
Cooperative Institute for Research in Environmental Sciences (CIRES)
University of Colorado, Boulder, Colorado 80309-0449

² Department of Geological Sciences
University of Colorado, Boulder, Colorado 80309

1. INTRODUCTION

Imaging radar data provides information about the geometric and dielectric properties of the Earth's surface (Ulaby et al, 1982). The Jet Propulsion Laboratory (JPL) polarimetric Airborne Synthetic Aperture Radar (AIRSAR) is currently obtaining imaging radar data for use in geologic, vegetation, snow and ice, and oceanic studies (Held et al., 1988; Zebker et al, 1987). In the near future, the Shuttle Imaging Radar C (SIR-C/X-SAR) and the Earth Observing System Synthetic Aperture Radar (EOS SAR) will also collect polarimetric radar data (JPL, 1986, 1991).

A need exists for a user-friendly, interactive software package for analysis of these polarimetric radar data sets. Previous software packages, such as JPL's Multiview (Burnette, 1988), while providing some analysis capabilities for these data, did not allow interactive viewing and were tied to specific image display hardware with operating system dependencies.

A prototype software system, the "Radar Analysis and Visualization Environment" (RAVEN) under development at the Center for the Study of Earth from Space (CSES) at the University of Colorado, is designed to deal with data from the JPL AIRSAR instrument and other proposed polarimetric radar instruments. RAVEN is being developed using the Interactive Data Language (IDL) (Research Systems, 1991). It takes advantage of high speed disk access and fast processors running under the UNIX operating system in a X-windows environment to allow for rapid, interactive visualization of AIRSAR data in both image and graphical ways. It provides a user-friendly interface through the use of menus, sliders, buttons, and display windows (Figure 1).

2. DISPLAY FEATURES

Analysis of polarimetric radar data requires innovative display of both images and quantitative information. The images provide spatial information and the graphics provide frequency and polarimetric information. It is necessary to view an entire scene and at the same time be able to see subscenes at full resolution, and enlarged to observe details. RAVEN is designed to create and manage multiple data windows. An entire AIRSAR scene subsampled to fit in a scroller window allows selection of an area to be displayed at full resolution in a image window. A zoom window allows for a subset of the image to be panned and zoomed from 1 to 16 times. RAVEN also provides the capability to interactively select and display synthesized polarimetric images for three frequencies as gray scale images, density-sliced images, or as color composites. These images are displayed as sigma-zero backscatter or total power values. Images of any polarization combination can be synthesized in RAVEN using the Stokes matrices for the calculations. This synthesis, however, takes approximately 2 minutes and is not considered real-time. Therefore, RAVEN also uses a band sequential format data set that contains various pre-synthesized polarization images. This makes possible rapid display of gray scale and color images.

Rapid viewing of frequency and polarization information for individual pixels allows users to get an idea of the variation in a data set. It also allows definition of areas for detailed analysis. RAVEN uses co-polarized and cross-polarized signature windows that provide real-time viewing of cross sections of polarization signatures. A window is also provided to view frequency plots. Frequency plots and full polarization signatures from multiple pixels are saved in another window and allow the user to compare different units.

3. ANALYSIS FEATURES

The analysis capabilities of RAVEN presently include creating and viewing polarization and frequency signatures for the three AIRSAR frequencies using a pull-down menu in the main RAVEN window. Calculation of polarization signatures and frequency plots for both individual pixels and polygon regions is provided. Polarization signatures are 3-dimensional plots that represent the radar backscatter as a function of all ellipticity and orientation polarizations (van Zyl et al, 1987). The polarization signatures generated in RAVEN are displayed as both 3-dimensional plots and 2-dimensional images. These plots and images are displayed as either gray scale or density-sliced color. Polarization signatures extracted from the data can be compared to each other or to theoretical polarization signatures created for specified input scattering matrix values. A signature viewer window also allows both subtraction and division operations to be performed on polarization signatures.

Images of RMS surface roughness, fractal dimension, and dielectric constants are imported from an inversion program and displayed in RAVEN (Kierein-Young and Kruse, 1992). The images allow the user to view the spatial variance of these parameters and help in creating maps of different units.

4. FUTURE DEVELOPMENT

RAVEN is a prototype software tool under development for analysis of polarimetric radar data. Features are being added to deal specifically with analysis requirements for geologic targets. Classifications, library functions, polarimetric matching techniques, and inversion models are some of the future enhancements planned for the RAVEN package.

5. ACKNOWLEDGEMENTS

Portions of this work were supported under a NASA Graduate Student Researchers Grant (NGT-50728). Portions of this work were supported under the SIR-C/X-SAR project by NASA/JPL contract 958456.

6. REFERENCES

Burnette, Fred, 1988, JPL Multipolarization Software Package, JPL internal publication, 142 p.

Held, D. N. et al. 1988, The NASA/JPL multifrequency, multipolarization airborne SAR system: in Proceedings, IGARSS '88, The Institute of Electrical and Electronics Engineers, Inc. (IEEE), New York, p. 345-349.

Jet Propulsion Laboratory, 1986, Shuttle imaging radar-C science plan: JPL Publication 86-29, Jet Propulsion Laboratory, Pasadena, California.

Jet Propulsion Laboratory, 1991, The Earth Observing System Synthetic Aperture Radar (EOS SAR): Report to the Space Science and Applications Advisory

Committee (SSAC) for the Office of Space Science and Applications (OSSA)
1992 Strategic Plan, 25 p.

Kierein-Young K. S., and Kruse, F. A., 1992, Extraction of quantitative surface characteristics from AIRSAR data for Death Valley, California: in Proceedings of the Fourth AIRSAR Workshop (this volume).

Research Systems, Inc. (1991), IDL® User's Guide Version 2.2.

Ulaby, Fawwaz T., Richard K. Moore, and Adrian K. Fung, 1982, Microwave Remote Sensing Active and Passive, Addison-Wesley Publishing Company, Massachusetts.

van Zyl, J. J., H. A. Zebker, and C. Elachi, 1987, Imaging radar polarization signatures: Theory and observation, Radio Science, V. 22, No. 4, pp. 529-543.

Zebker, Howard A., Jakob J. van Zyl, and Daniel N. Held, 1987, Imaging Radar Polarimetry From Wave Synthesis, Journal of Geophysical Research, V. 92, No. B1, pp. 683-701.

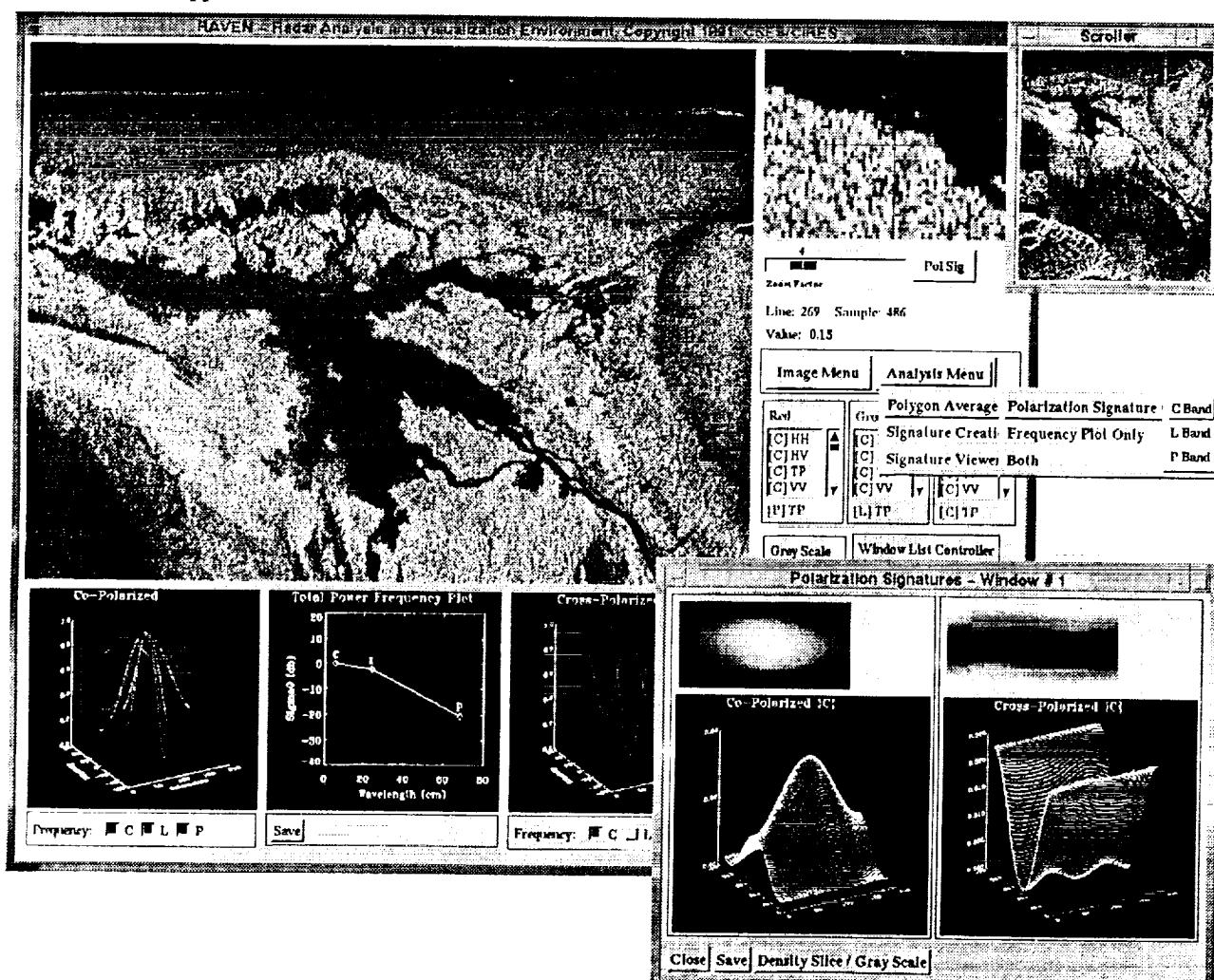


Figure 1. An example of the RAVEN software display screen.

Measuring Ocean Coherence Time with Dual-Baseline Interferometry

Richard E. Carande
 Jet Propulsion Laboratory
 California Institute of Technology
 4800 Oak Grove Drive, Pasadena, CA 91109

ABSTRACT

Using the JPL AIRSAR interferometer, measurements of the ocean coherence time at L and C band can be made at high spatial resolution. Fundamental to this measurement is the ability to image the ocean interferometrically at two different time-lags, or baselines. By modifying the operating procedure of the existing two antenna interferometer, a technique has been developed make these measurements. L band coherence times are measured and presented in this paper.

Introduction

Over the past 20 years or so there have been many theories and models put forth concerning microwave sensing of the ocean surface and the importance of the time scale at which the scattering remains coherent. The coherence time in SAR is particularly important since SAR imaging relies on coherent integration to achieve the along-track resolution. Some recent estimates of the ocean coherence time at L band have been made on the order of 0.05 to 0.1 seconds [1,2,3].

The along-track interferometric SAR used by JPL [4] to measure ocean surface "velocities" makes a direct measurement of the coherence of the ocean surface over the lag time separating the observations by the two antennas. A technique has been devised [5] where measurements at two baselines, or lag times, may be acquired simultaneously with the existing AIRSAR two antenna L band system by taking advantage of the multichannel transmit and receive capability required for polarimetric data acquisition. The AIRSAR polarimeter acquires full polarization information by transmitting H and V alternately while receiving H and V from each transmit event. Using an identical scheme, radar pulses are emitted from the forward (F) and aft (A) antennas alternately and received by both. This produces four channels of data, FF, FA, AF and AA, which may be processed to imagery analogous to the polarimetric case. Two unique interferometric baselines may be constructed using these data, one being the separation distance of the antennas and the second being half this distance.

Example data

The AIRSAR instrument imaged the Strait of Messina in the summer of 1991. The mode of operations for one data take was the dual ATI baseline mode for L and C, and standard quad-pol for P band. A phase difference image is obtained (after processing to remove aircraft motion and sensor geometry phase effects) by combining the LAA complex image (A) with (in this case) the LAF (F) complex image according to the following formula:

$$\Delta\phi = \tan^{-1} \left(\frac{\text{imag}(C)}{\text{real}(C)} \right) \quad (1)$$

where:

$$C = F A^* \quad (2)$$

A multi-look phase is determined by coherently summing the interferogram pixels, C , and retaining the resultant phase. This method has been shown by Rodriguez [6] to be the maximum likelihood estimator for determining the interferometric phase. In this case summation over 16 azimuth pixels was used. The phase difference may be converted to interferometric velocities using the following equation:

$$u = \Delta\phi \frac{\lambda v}{4\pi B} \quad (3)$$

where $\Delta\phi$ is the observed phase change, B is the baseline length, v is aircraft speed and λ is the radar wavelength. The ratio of B/v represents the time lag, τ , between forward and aft imaging. The interferometer velocity represents the radial component of the phase change. To project this onto the ground image plane, to extract the surface component, one must divide by $\sin(\theta)$, where θ is the incidence angle. The surface interferometer velocity may be written as:

$$u_s = \frac{\Delta\phi}{k_b \tau} \quad (4)$$

where $k_b = 4\pi/\lambda \sin(\theta)$ and is identified as the Bragg wavenumber.

Measuring coherence time with ATI

In addition to observing the phase difference and producing interferometer velocity maps, correlation maps of the ocean surface may be produced for each baseline. With this dual baseline information, the coherence time of the ocean surface can be measured directly. The coherence time is defined here as the time it takes the autocorrelation function of the backscatter field from the ocean to be reduced to $1/e$. The correlation strength between two images forming a baseline is given by ρ_i where i denotes which of the two baselines the correlation calculation is being carried out on. The correlation image may be calculated as follows:

$$\rho_i = \frac{\left| \frac{\sum f a^*}{\sqrt{\sum |f|^2 \sum |a|^2}} \right|}{\quad} \quad (5)$$

where f and a are the pixels of the forward and aft phase center images for baseline i , and the summations are carried out over an adjacent number of pixels, typically 8 or 16, similar to a multilook filter.

By using the two baselines available with the AIRSAR data, one may measure two values of ρ : ρ_s and ρ_l where s and l indicate "short" and "long" baselines. The nominal time lags associated with the two AIRSAR baselines corresponding to these measurements are 0.05 and 0.10 seconds respectively. Assuming a Gaussian correlation function, the $1/e$ coherence time, τ_c , may be calculated using these two measurements:

$$\tau_c = \sqrt{-\frac{\tau_s^2 + \tau_l^2}{\ln(\rho_s \rho_l)}} \quad (6)$$

High resolution correlation images for the short and long baseline of the Messina data have been formed using (5). From these short and long baseline correlation images, a coherence time image has been formed using (6). The image was quantized to 16 levels going between 0.0 seconds and 0.32 seconds in linear units of 0.02 seconds. The land areas exhibit coherence times greater than the 0.32 maximum. There is quite a bit of structure to this map, both large scale and small scale. There are areas in which the coherence time is noticeable larger than other areas. Ocean coherence times observed in this L-band image vary from about 0.09 seconds to 0.27 seconds.

Acknowledgment

Special thanks goes to S. Madsen for the development and implementation of the SAR processing and motion compensation algorithms used to process the data presented here. The work described in this paper was carried out at the Jet Propulsion Laboratory of the California Institute of Technology, and supported under contracts with National Aeronautics and Space Administration and the Office of Under Secretary of Defense.

¹ Lyzenga, D., "An analytic representation of the synthetic aperture radar image spectrum for ocean waves," *J. Geophys. Res.*, vol 93, no C11, 13,859-13,865, 1988.

² D. Kasilingam and O. Shemdin, "Theory for synthetic aperture radar imaging of the ocean surface: With application to the tower ocean wave and radar dependence experiment of focus, resolution and wave height spectra," *J. Geophys. Res.*, vol 93, no C11, 13,837-13,848, 1988.

³ W. Plant and W Keller, "Evidence of Bragg scattering in microwave Doppler spectra of sea return," *J. Geophys. Res.*, vol 95, no C9, 16,299-16,310, 1990.

⁴ R.M. Goldstein and H.A. Zebker, "Interferometric radar measurements of ocean surface currents," *Nature*, Vol. 328, 20 August 1987.

⁵ R.E. Carande, "Dual baseline and frequency along-track interferometry," *IGARSS '92 Proceedings*, May 1992.

⁶ E. Rodriguez and J. Martin, "Maximum likelihood estimation of the interferometric phase from distributed targets," to be published in *IEEE Trans Geosci Remote Sens*.

A BIBLIOGRAPHY OF GLOBAL CHANGE, AIRBORNE SCIENCE, 1985-1991

Edwin J. Sheffner

TGS Technology, Inc.
MS 239-20, Ames Research Center, Moffett Field, California 94035

James G. Lawless

National Aeronautics and Space Administration
MS 239-20, Ames Research Center, Moffett Field, California 94035

In response to mounting scientific evidence that the biosphere and atmosphere of the earth are undergoing significant anthropogenic changes that appear to be increasing in magnitude and rate, the United States launched the Global Change Research Program (USGCRP) in 1989. The goal of the program is to "...Gain a predictive understanding of the interactive, physical, geological, chemical, biological and social processes that regulate the total earth system." Seven government agencies are involved in the program with the National Aeronautics and Space Administration (NASA) playing a key role by providing space based and earth based data.

The mission elements of NASA's approach to global change research involve the collection and analysis of satellite data from earth probes, geostationary platforms and the primary element of the NASA effort, the Earth Observing System (EOS). EOS consists of a series of polar orbiting platforms that will carry a variety of sensors capable of collecting digital data with spectral and spatial resolution suitable to support multi-disciplinary research in earth system science.

Many of the new remote sensing systems that will begin generating data by the end of this century are based on experiments conducted, and knowledge gained, using airborne platforms, especially within the last 25 years. Although the capability to conduct large scale monitoring of earth processes may be dated from July, 1972 with the launch of Landsat 1, neither the Landsat system nor any of the numerous devices launched since Landsat 1, or now planned for launch, preclude the need to develop and operate remote sensing systems on aircraft. Airborne remote sensing will continue to have scientific merit because 1) new concepts in remote sensing can be developed and proved faster and more cheaply on aircraft than on satellites; 2) the capabilities of aircraft systems are likely to improve, e.g. long duration, pilotless flights, increasing the utility of aircraft for earth observation measurements, especially observations required in response to unusual, rapidly developing events; 3) measurements from aircraft have been shown to be critical in studies of the expression of biophysical processes in the landscape; and 4) evidence indicates that data from airborne sensors increases the value of satellite derived data on global change processes by supplying information that lowers the error associated with satellite-data-driven estimates of the output of those processes.

A bibliography of global change, airborne science from 1985 to 1991 was assembled that may be of utility to the science community. The bibliography was compiled using EndNote® Plus, a software system that operates in Macintosh and PC environments. The intent of the bibliography is to include all articles (primarily in

refereed journals) that address global change issues and that utilize aircraft to acquire data. The bibliography is a tool that has a variety of functions. It can be used by the science community as a reference to search for articles on specific topics, and it is gauge for assessing the impact of airborne sensors on global change science. From the bibliography data base information can be extracted on who is performing global change airborne science, who is sponsoring the research, where the research is being performed and what type of research is being done.

The bibliography includes entries for journal articles, conference proceedings, book and book sections, and reports. For journal articles the data base includes author(s), title, journal name, volume number, year of publication, month of issue, affiliation of author(s), key words, a label field, and abstract (if available). The software allows for inclusive and exclusive searches of the bibliography by character string. Citations can be formatted in numerous ways for entry as in-text citations or bibliographic references. The current version of the bibliography will be updated periodically, and new versions should be available bi-annually.

SOIL CONSERVATION APPLICATIONS WITH C-BAND SAR

Brisco, B.¹, R.J. Brown², J. Naunheimer¹, and D. Bedard¹

¹ Intera Information Technologies	² Canada Centre for Remote
2 Gurdwara Rd., Suite 200	Sensing
Nepean, ON	2464 Sheffield Road
Canada K2E 1A2	Ottawa, ON K1A 0Y7
Tel: (613) 226-5442	Tel: (613) 952-0500
Fax: (613) 226-5529	Fax: (613) 952-7353

Soil conservation programs are becoming more important as the growing human population exerts greater pressure on this non-renewable resource. Indeed, soil degradation affects approximately 10 percent of Canada's agricultural land (Dumanski et al., 1986) with an estimated loss of 6,000 hectares of topsoil annually from Ontario farmland alone (Agricultural Institute of Canada, 1980). Soil loss not only affects agricultural productivity but also decreases water quality and can lead to siltation problems. Thus, there is a growing demand for soil conservation programs and a need to develop an effective monitoring system.

Local topography, soil type, plant residue, vegetative cover, and surface roughness interact to govern soil erosion by wind and water. In general, smooth bare sandy soils are most susceptible to erosion. Contour farming, increasing crop residue and deep tillage to create enough surface roughness to break wind/water flow velocities are management techniques being used to reduce erosion risk. Topography and soil type information can easily be handled within a geographic information system (GIS). Information about vegetative cover type and surface roughness, which both experience considerable temporal change, can be obtained from remote sensing techniques. Thus all the components for a monitoring system are available.

Previous research has shown that useful information for soil conservation applications can be extracted using visible and near infra-red wavelengths (Gausman et al., 1975). Atmospheric effects and winter snow cover over much of the northern United States and

southern Canada limit the data availability in this region of the electromagnetic spectrum. Microwave systems, both active and passive, provide a reliable alternative. Recent research has demonstrated that information about residue/plant cover and surface roughness can be obtained using these types of sensors (Ulaby et al., 1986). For example, Brisco et al. (1991) found that C-Band like polarization was effective for discriminating between different tillage classes on wheat stubble fields as a function of surface roughness.

For further development of the technology to produce an operational soil conservation monitoring system an experiment was conducted in Oxford County, Ontario which investigated the separability of fall surface cover type using C-Band SAR data. This experiment obtained quantitative information on surface roughness and crop residue for about 30 fields in the study site and qualitative information on about another 250 fields.

To date only C-HH narrow swath data (6 meter resolution, 45-76 degrees incidence, 7-look amplitude format) have been analyzed. Transformed divergence separability statistics show that corn stubble can be separated into two classes (high and low stubble) and bare smooth fields can be differentiated from deep tilled fields. Confusion between bare fields and pasture or hay fields, which are also dark on the SAR imagery, could be removed with complementary optical data acquired any time earlier in the growing season. Alternatively, a GIS cover type layer could be generated from historic data as pasture and hay fields are recurring cover types on a yearly basis. This approach is proving useful for other agricultural classification purposes (Bedard et al., 1992). Corn fields that have not been harvested are also highly separable, as previous work has demonstrated (Brisco and Protz, 1980).

Transformed divergence statistics will be calculated for the other polarizations (VV, HV) and evaluated for separability of these conservation classes. Furthermore the analysis will be expanded to include multi-polarization combinations, co-polarization ratios, and cross-polarization ratios to see if improvements in class separability of conservation farming classes can be obtained with multi-polarization C-band SAR data. The results of these analyses will be related to upcoming spaceborne SAR sensors to evaluate the potential for this application using data which should be available in the next couple of years. GIS models incorporating local topography

and soil type to create an erosion potential map are also being developed. Synergism of the SAR data with visible and near-infrared channels from SPOT and TM will also be evaluated. The presentation at the AIRSAR workshop will summarize the results that have been obtained by the time of the workshop.

This research will continue with experiments already planned using ERS-1, SIR-C, and Radarsat data for further development of this application. It is envisioned that operational soil conservation monitoring systems are possible by Radarsat, or at the least by the Earth Observing System (EOS), timeframe.

References

Agricultural Institute of Canada, 1980, "Task Force Report: Soil Erosion on Agricultural Land in Canada", Agrologist, pp. 23-28.

Bedard, D., R. Brown, J. Naunheimer, B. Brisco, and S. Huang, 1992, "Investigating Crop Rotation Knowledge to Improve Agricultural SAR Classifications", Canadian Symposium on Remote Sensing, Toronto, ON, June 1-4, in-press.

Brisco, B. and R. Protz, 1980, "Corn Field Identification Accuracy Using Airborne Radar Imagery", Canadian J. Remote Sensing, V.6(1), pp. 15-24.

Brisco, B., R.J. Brown, B. Snider, G.J. Sofko, J.A. Koehler and A.G. Wacker, 1991, "Tillage Effects on the Radar Backscattering Coefficient of Grain Stubble Fields", Int. J. Remote Sensing, V. 12(11), pp. 2283-2298.

Dumanski, J., D.R. Coote, G. Lucuik, and C. Lok, 1986, "Soil Conservation in Canada", Journal of Soil and Water Conservation, V. 41, pp. 204-210.

Gausman, H.W., A.H. Gerbermann, C.L. Wiegand, R.W. Leamer, R.R. Rodriguez and J.R. Noriega, 1975, "Reflectance Differences Between Crop Residues and Bare Soils", Soil Science Society of America Proceedings, V. 39, pp. 752-755.

Ulaby, F.T., R.K. Moore, and A.K. Fung, 1986, "Microwave Remote Sensing: Active and Passive, V. III: From Theory to Applications", Artech House, Inc., Dedham, MA.

COMPARISON OF EDGES DETECTED AT DIFFERENT POLARISATIONS IN MAESTRO DATA

Ronald G. Caves, Peter J. Harley and Shaun Quegan

Department of Applied and Computational Mathematics, University of Sheffield,
PO Box 597, Sheffield S10 2UN, England.

1. INTRODUCTION

Edge detection would appear to be a crucial tool for analysing multi-polarised, multi-frequency and multi-temporal Synthetic Aperture Radar (SAR) images. Edge structure provides a simple means for comparing different polarisations and frequencies, and for detecting changes over time. Due to the fact that edges and segments (homogeneous regions) are dual concepts, edge detection has an important role to play in identifying segments within which mean backscatter measurements for use in image classification can be made (*White 1991*).

As part of a general investigation into edge detection in SAR imagery, an initial investigation has been carried out into the detectability and nature of edges in multi-polarised and multi-frequency SAR images. The contrast ratio (CR) operator was used to detect edges. This operator has previously been shown to perform well at detecting edges in single-polarised and single-frequency SAR images (*Touzi et al. 1988; Caves et al. 1992*).

2. THE CONTRAST RATIO OPERATOR

At each point in an image the contrast ratio across a $n \times n$ window centred at that point is calculated by splitting the window into two equal sections, estimating the mean value of the pixels in each section and taking the ratio of these two mean values. Ratios are calculated for splits along the horizontal, vertical and two diagonal orientations. The largest ratio gives a measure of the contrast across the window. The larger the ratio, the greater the contrast, and the greater the likelihood that an edge exists at that point.

The contrast ratio image is thresholded to produce an edge map. So long as speckle is a stationary multiplicative noise process the false alarm rate in the edge map will be constant. Additionally, if it is assumed that speckle in an intensity image is uncorrelated and gamma distributed, the distribution of the contrast ratio can be determined and used to set a threshold for a desired probability of false alarm. The effects on the false alarm rate of known system induced correlation can be removed by sub-sampling within the processing window.

3. APPLICATION TO MAESTRO IMAGES

The CR operator was applied to C and P band MAESTRO single-look intensity images of Feltwell, UK. For each band the binary edge maps produced from two different polarisations were compared by overlaying them; the symbol

"o" is used to represent this binary operation (i.e. $\mathbf{HV} \circ \mathbf{VH} = \mathbf{HV} \times 2 + \mathbf{VH}$). This was done for all possible combinations of two different polarisations. Pixel values in the resulting 2-bit images indicated: 0 - no edge at either polarisation, 1 or 2 - an edge at one polarisation but not the other and 3 - an edge at both polarisations. The process was repeated with edge maps produced using different window sizes $n = 3, 5, \dots, 17$ and probabilities of false alarm $p = 10^{-3}, 10^{-4}, \dots, 10^{-6}$ (assuming exponential speckle). The correlation length in both range and azimuth was found to be two pixels; 2×2 sub-sampling was used within processing windows to remove its effect.

4. RESULTS

In each set of edge maps produced from the C band image using a particular window size and probability of false alarm, the greatest degree of similarity occurred between the edge maps of the cross-polarised terms (most values in $\mathbf{HV} \circ \mathbf{VH}$ were 0 or 3). A lesser degree of similarity occurred between the edge maps of the co-polarised terms. The most significant differences occurred between the edge maps of a co and a cross-polarised term. However due to the similarity of the edge maps of the cross-polarised terms, the differences occurring between the edge maps of a co-polarised term and the \mathbf{HV} term were similar to those occurring between the edge maps of the same co-polarised term and the \mathbf{VH} term.

These traits can be observed in figures 1 and 2 which show the results of edge detection using a 9×9 window with a probability of false alarm of $p = 10^{-4}$. Figure 1 shows the edge maps of the \mathbf{HH} , \mathbf{HV} and \mathbf{VV} terms and the result of combining the edge maps of all four polarisations. The edge maps of the single terms are all different from each other. Differences arise not just from edges being better defined in some polarisation than in others but also from features present in some polarisations being completely absent in others. The edge map of the \mathbf{HV} term contains significantly more detail than that of the \mathbf{HH} term which in turn contains slightly more detail more than that of the \mathbf{VV} term. The combined edge map is significantly more detailed than that of any single polarisation; each polarisation contributes something towards it.

Figure 2 shows histograms of combinations of edge maps of the (a) \mathbf{HH} and \mathbf{VV} , (b) \mathbf{HV} and \mathbf{VH} , (c) \mathbf{HH} and \mathbf{HV} , and (d) \mathbf{VV} and \mathbf{HV} terms using the "o" operator described above. The $\mathbf{HH} \circ \mathbf{VV}$ histogram shows that the percentage of edge pixels detected in the \mathbf{HH} term (i.e. those pixels with values 2 and 3) was greater than the percentage detected in the \mathbf{VV} term (pixels with values 1 and 3). The $\mathbf{HV} \circ \mathbf{VH}$ histogram shows that the small proportion of differences between the \mathbf{HV} and \mathbf{VH} terms is equally split between edges detected in the \mathbf{HV} term and not in the \mathbf{VH} term and edges detected in the \mathbf{VH} term and not in the \mathbf{HV} term. The $\mathbf{HH} \circ \mathbf{HV}$ and $\mathbf{VV} \circ \mathbf{HV}$ histograms show that the differences between co and cross-polarised terms is primarily due to a greater percentage of edges being detected in cross-polarised terms than in co-polarised terms. The total percentage of edges pixels in a given combination is indicated by subtracting the percentage of pixels with value 0 from 100. The greatest number of edges is detected by combining a co and a cross-polarised term and the least when the edge maps of the co-polarised terms are combined.

Apart from the \mathbf{HV} term, the P band image was much sharper than the C band image. This resulted in a much larger percentage of edges being detected. Once again the edge maps of cross-polarised terms were similar whilst edge maps of co-polarised terms were significantly different from those of cross-polarised

terms.

5. CONCLUSION

The CR operator has detected edge information useful for comparing differently polarised terms and for use in further processing. Significant differences exist between the edges detected in different polarisations. The most significant differences occurred between co and cross-polarised terms. The differences were small between cross-polarised terms, as reciprocity would predict. The images used were uncalibrated. However, assuming a linear system model, it can be shown that, to a good approximation calibration of this data involves only linear scalings of the intensity images (Quegan 1992). Such scalings would not affect the outcome of applying the CR operator. The fact that the images were not of comparable quality places more serious constraints on interpreting the results in terms of fundamental scattering properties of edges.

REFERENCES

- R. G. Caves, P. J. Harley and S. Quegan "Edge structure in ERS-1 and airborne SAR data," in *Proc. IGARSS'92* (Houston, USA), 1992.
- S. Quegan, "Cross-talk calibration of the MAESTRO data from the Reedham and Feltwell test-sites," in *Proc. MAESTRO Final Workshop*, (Noordwijk, The Netherlands), 1992.
- R. Touzi, A. Lopes and P. Bousquet, "A statistical and geometrical edge detector for SAR images," *IEEE Trans. Geosci. Remote Sens.*, vol. 26, pp. 764-773, 1988.
- R. White, "Change detection in SAR imagery," *Int. J. Remote Sensing*, vol. 12, pp. 339-360, 1991.

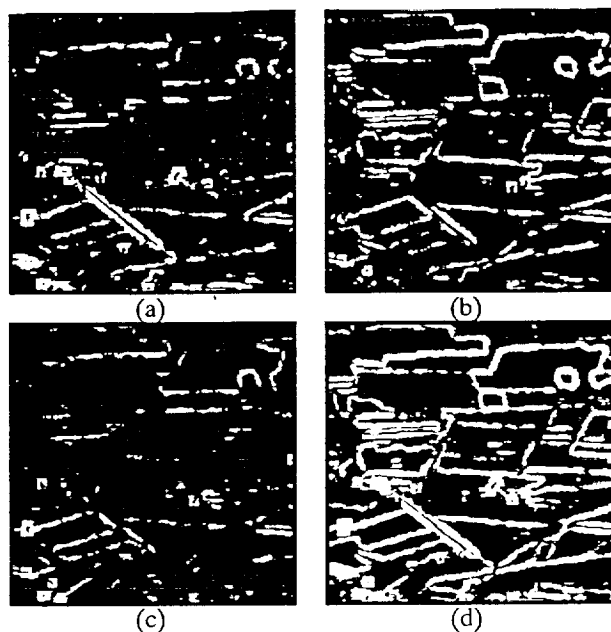


Figure 1. Edge maps of a MAESTRO C band image of an agricultural area produced using the contrast ratio operator with a 9×9 window and a probability of false alarm of 0.0001: (a) HH, (b) HV, (c) VV and (d) HH + HV + VH + HH.

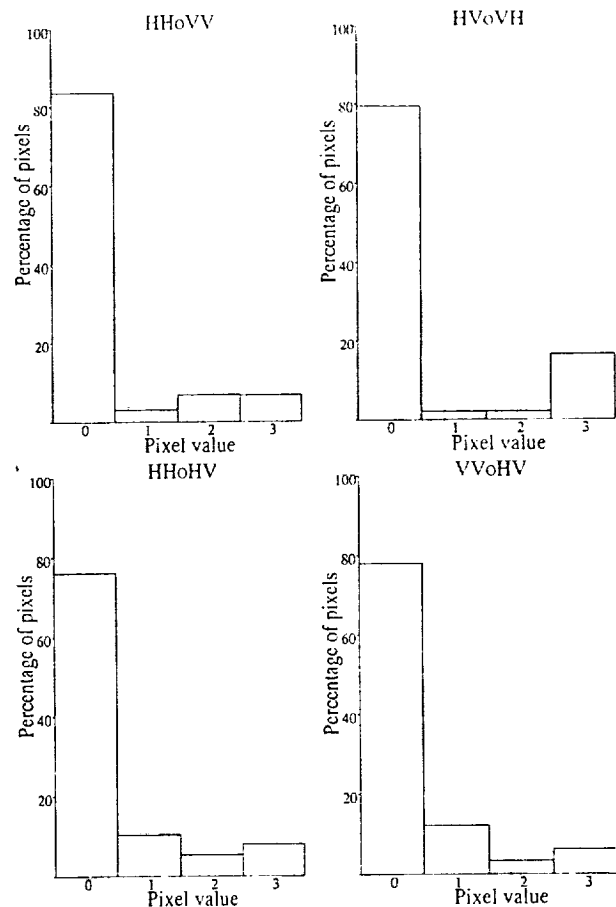


Figure 2. Histograms of combined edge maps.

LITHOLOGICAL AND TEXTURAL CONTROLS ON RADAR AND DIURNAL THERMAL SIGNATURES OF WEATHERED VOLCANIC DEPOSITS, LUNAR CRATER REGION, NEVADA

Jeffrey J. Plaut
Jet Propulsion Laboratory
Mail Stop 230-225, 4800 Oak Grove Drive, Pasadena, CA 91109.

Benoit Rivard
Earth Observation Laboratory,
Institute for Space and Terrestrial Science, York University
4850 Keele Street, North York, Ontario, Canada M3J 3K1.

1. INTRODUCTION

Radar backscatter intensity as measured by calibrated synthetic aperture radar (SAR) systems is primarily controlled by three factors: local incidence angle, wavelength-scale roughness, and dielectric permittivity of surface materials. Radar observations may be of limited use for geological investigations of surface composition, unless the relationships between lithology and the above characteristics can be adequately understood. In arid terrains, such as the Southwest U.S., weathering signatures (e.g. soil development, fracturing, debris grain size and shape, hill slope characteristics) are controlled to some extent by lithologic characteristics of the parent bedrock. These textural features of outcrops and their associated debris will affect radar backscatter to varying degrees, and the multiple-wavelength capability of the JPL AIRSAR system allows sampling of textures at three distinct scales.

Diurnal temperature excursions of geologic surfaces are controlled primarily by the thermal inertia of surface materials, which is a measure of the resistance of a material to a change in temperature (Gillespie and Kahle, 1977). Other influences include albedo, surface slopes affecting insolation, local meteorological conditions and surface emissivity at the relevant thermal wavelengths. To first order, thermal inertia variations on arid terrain surfaces result from grain size distribution and porosity differences, at scales ranging from micrometers to tens of meters. Diurnal thermal emission observations, such as those made by the JPL TMS airborne instrument, are thus influenced by geometric surface characteristics at scales comparable to those controlling radar backscatter.

This paper is a preliminary report on a project involving a combination of field, laboratory and remote sensing observations of weathered felsic-to basaltic volcanic rock units exposed in the southern part of the Lunar Crater Volcanic Field, in the Pancake Range of central Nevada (Snyder et al, 1972). We focus here on the relationship of radar backscatter cross sections at multiple wavelengths, apparent diurnal temperature excursions identified in multi-temporal TMS images, surface geometries related to weathering style, and parent bedrock lithology.

2. GEOLOGIC SETTING

The Lunar Crater portion of the Pancake Range consists of normal-faulted blocks of Tertiary rhyolitic to andesitic volcanic rocks, overlain in places by a Quaternary alkaline basalt field, which includes lava flows, cinder cones and maar craters (Scott and Trask, 1971; Snyder et al, 1972). The area described in this paper includes the southern portion of the basalt field, consisting of two lava flow complexes and two associated cinder cones. The Tertiary volcanic rocks in the area include andesitic and quartz latitic lavas, and a number of distinct welded and bedded tuff units, displaying varying phenocryst and lithic contents and devitrification textures (Snyder et al, 1972).

Basalt outcrops in the area show relatively mature upper weathered surfaces, with well-developed desert pavements consisting of basalt cobbles 1-10 cm in diameter resting on an aeolian-derived sediment of up to several m thickness. Felsic outcrop morphologies

are highly variable, ranging from low rounded hills with relatively thick debris mantles to cap-rocked mesas with fresh bedrock exposures and over-steepened cliff faces as high as 250 m. Alluvial deposits are predominantly sandy gravels, although several washes contain clasts up to large boulder size, reflecting high-energy depositional environments. Relationships at basalt flow margins indicate that these high valleys have been predominantly in a downwasting regime since the basalt eruptions.

3. REMOTE SENSING DATA

AIRSAR data for the southern Lunar Crater area includes three passes along the same azimuth, providing three incidence angles for many of the surfaces of interest. TIMS coverage consists of three sets of overlapping paired passes, acquired at approximately 4 a.m., 8 a.m. and 2 p.m. local time. Figure 1 shows a segment of the afternoon and pre-dawn Band 5 (10.3-11.1 μm) TIMS passes, along with an L-band HH polarization AIRSAR image of approximately the same area.

Changes in contrast relationships among surfaces between the afternoon and pre-dawn TIMS images are almost certainly related to thermal inertia variations. Comparison with the 8 a.m. image taken on the same day (not shown) indicates that differential heating related to slope/insolation effects is minimal by the late afternoon, and is certainly of negligible importance for the pre-dawn data. An interesting reversal in contrast is seen between adjacent outcrop areas of welded tuff (indicated by numbers 1 and 2). The southern outcrop (1) shows relatively little difference in emittance from the surrounding alluvial surfaces in both scenes, while the northern outcrop (2) is much darker in the afternoon scene and much brighter in the pre-dawn scene. Although these data have not yet been calibrated to extract temperature or thermal inertia estimates, qualitative examination indicates that the northern outcrop has a higher thermal inertia than the southern outcrop, expressed as a smaller excursion in temperature relative to the surroundings. AIRSAR data for these two surfaces suggest a relationship between outcrop morphology, surface roughness and thermal inertia. Figure 2 shows the behavior of radar cross section (σ_0) as a function of wave number ($2\pi/\lambda$) for several surfaces. The northern tuff outcrop exhibits high σ_0 values at all three AIRSAR wavelengths, while the southern outcrop has much lower values, and a strong dependence on wavelength. Field observations indicate that the northern outcrop is dominated by fresh exposures and high local relief, while the southern outcrop is pervasively fractured at the cm scale, leading to low relief and a mantle of cm-scale gravel debris. The diurnal temperature contrast is clearly related to the presence of the high thermal inertia rock exposures in the north and the low thermal inertia gravel debris in the south. Similarly, the AIRSAR signatures reflect the steep topography in the north, which leads to high σ_0 values independent of wavelength. On the southern outcrop, the surface appears smooth at P band and relatively rough at C-band, consistent with field observations of the roughness scale of the gravel debris. Although mapped by Snyder et al (1972) as a single unit, the two outcrops display dramatically different radar and thermal signatures related to weathering style. Further sample analysis should illuminate the lithological basis for the contrasting morphology.

At the "boulder field" site (3 in Fig.1), the presence of m-scale and larger boulders is probably responsible for the apparently higher thermal inertia (note bright "warm" signature in pre-dawn scene) of this deposit compared to the surrounding alluvium. This distinct roughness signature is reflected in the SAR data (bright patch in Fig.1), particularly at the longer wavelengths.

The "friable tuff" exposure (4 in Fig.1) consists of rounded "towers" of erodible fine-grained, possibly volcanoclastic tuff. Extensive patches of sandy debris shed from these exposures give the area an overall low thermal inertia, and an extremely smooth signature at C and L AIRSAR wavelengths. The unique radar and thermal signature of this unit is directly related to grain size and cementation, properties related to lithological and (volcanic or sedimentary) depositional parameters.

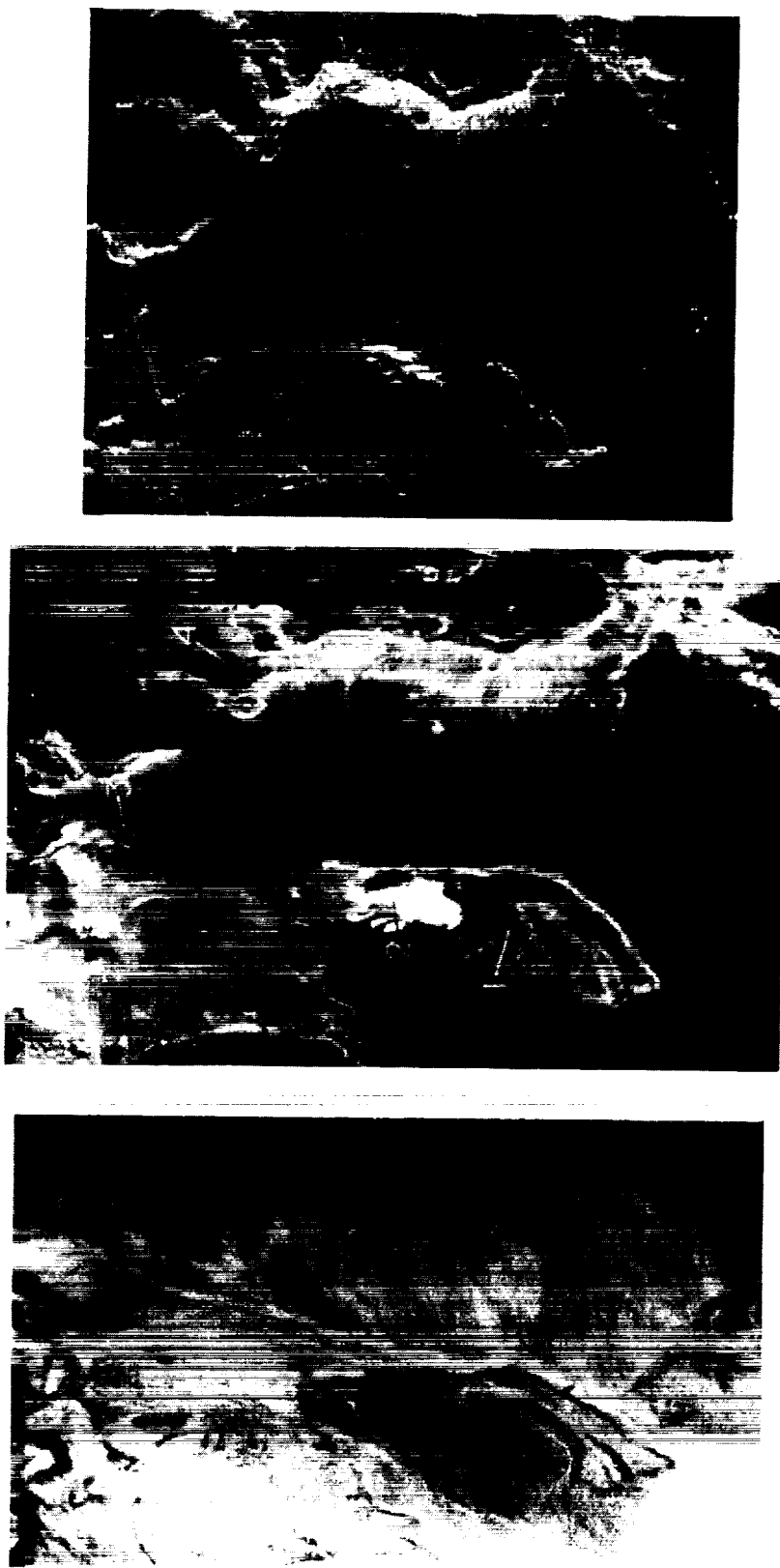


Figure 1. a) TMS band 5 (10.3-11.1 mm) image, afternoon and b) pre-dawn, c) AIRSAR L-band HH, illumination from the left. Scene dimensions are approximately 3 x 5 km. Locations marked in b are 1) south tuff outcrop, 2) north tuff outcrop, 3) boulder field, 4) friable tuff.

4. CONCLUSIONS

Preliminary analysis of radar, thermal and field observations of the southern Lunar Crater region indicates that textural characteristics that dominate radar and diurnal thermal signatures of surfaces are related (though probably not uniquely related) to the primary outcrop lithology. Application of AIRSAR data may be of use in analysis of TIMS data, in which grain size and compositional influences on emittance must be separated. Such combined multi-sensor and field studies also provide valuable experience for analysis of purely "remote" datasets, such as Magellan and Mars Observer.

5. REFERENCES

Gillespie, A.R. and A.B. Kahle, 1977, Construction and interpretation of a digital thermal inertia image, *Photogramm. Eng. and Rem. Sens.* 43, 983-1000.

Scott, D.H. and N.J. Trask, 1971, *Geology of the Lunar Crater Field, Nye County, Nevada*, USGS Prof. paper 599-I.

Snyder, R.P., E.B. Ekren and G.L. Dixon, 1972, *Geologic map of the Lunar Crater quadrangle, Nye County, Nevada*, USGS Misc. Inv. Map I-700.

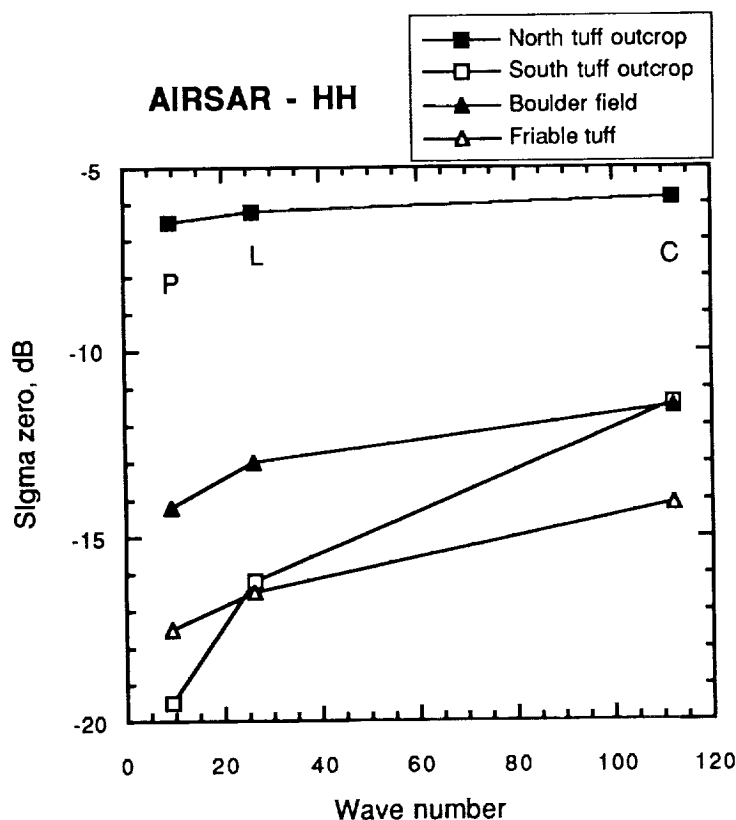


Figure 2. AIRSAR HH polarization backscatter cross section (sigma zero) as a function of wave number ($2\pi/\lambda$). Corresponding wavelengths are: P-band 68 cm, L-band 24 cm, C-band 5.6 cm. Flat spectrum of north tuff indicates topographic control. Steep spectrum of south tuff indicates low "power" at larger scales of surface roughness.

